Forward modelling 3-D geophysical electromagnetic field data with meshfree methods

by

A thesis submitted to the

School of Graduate Studies

in partial fulfillment of the

requirements for the degree of

Doctor of Philosophy (Geophysics)

Department of Earth Sciences

Memorial University of Newfoundland

May, 2020

St. John's Newfoundland and Labrador

Abstract

Simulating geophysical electromagnetic (EM) data over real-life conductivity models requires numerical algorithms that can incorporate realistically complex geometry and topography. The most successful way to incorporate them is to use unstructured meshes in the discretization of an Earth model. Current mesh-based numerical methods that are capable of using such meshes have inherent drawbacks caused by generating 3-D unstructured meshes conforming to irregular geometries. Such a mesh generation process may become computationally expensive and unstable, and particularly so for EM inversion computations in which the forward modelling may be required many times. In this thesis I investigate the feasibility and applicability of radial basis function-based finite difference (RBF-FD), a meshfree method, in forward modelling 3-D EM data. In the meshfree method, the physical model is represented using only a set of unconnected points, effectively overcoming the issues related to the mesh generation. To improve numerical efficiency, unstructured point sets are used in the computation for the first time for EM problems. The computation is further accelerated by introducing a new type of radial basis function in the RBF-FD method. The convergence and accuracy of the proposed RBF-FD method are demonstrated first via forward modelling gravity and gravity gradient data. The computational efficiency of the meshfree method is compared with that of using a more traditional finite element method. The meshfree method is then applied to forward model magnetotelluric data of which the effectiveness is demonstrated using three benchmark conductivity models from the literature. Faithful reproduction of

the physics in the EM fields, e.g. discontinuous electric fields across the conductivity contrasts, is achieved by proposing a hybrid meshfree scheme which is a modification to standard meshfree algorithms. The hybrid method is also applied to simulate controlled-source EM data in the frame of both total-field and primary-secondary field approaches, in which the problems in dealing with singular source functions that cause singularities in the EM fields are addressed. For these two approaches, the accuracies of the proposed hybrid meshfree method in forward modelling the controlled-source EM data are demonstrated by using idealized 1-D layered models and a 3-D marine canonical disk model. The successful applications of the proposed meshfree method in modelling the above EM data suggest that the meshfree technique has the potential of becoming an important numerical method for simulating EM responses over complicated conductivity models.

Acknowledgements

Throughout the years in my PhD study, I have had great helps from many people. First, I would like to give thanks, in a countless form indeed, to my supervisor Colin Farquharson. His spirit of endurance in guiding and supporting me throughout my research adventure is truly remarkable. Aside from generous financial supports, he is always encouraging and trying to provide ideas when I feel the road ahead is full of clouds. Quite honestly, I have never had a mentor before like him, who is doing the geophysical science at the frontiers and yet is always very humble, particularly so when he is trying to tell me something I don't know. I am sure I will forever benefit from what I've learned from his spirit of doing research. Without his support, my PhD research adventure will be much more bumpy.

Specific thanks are given to my supervisory committee, Alison Malcolm and Charles Hurich (Chuck). I am very grateful for their kindness, help and dedicated efforts in co-supervising my study. Whenever I go to them for help, even just for a chat, they are always there and willing to provide support.

I also want to express my gratitude to the following people in Colin's research group, Masoud Ansari, Hormoz Jahandari, Angela Carter-McAuslan, Mehrdad Darijani, Xushan Lu and Peter Lelièvre. I have always enjoyed discussions (not entirely about EM though) with them. Over the course of scientific research, we also have formed an informal tennis team, which is extremely important to help adapt to the not-always-beautiful weather of the lovely St John's.

Special appreciation goes to my family and my fiancée Grace. Without their conditionless love and support, I wouldn't be able to make the first step of my adventure in geophysical science, not to mention to make it this far.

Last but not least, I would like to thank our department as a whole. Their kindness and efforts in supporting graduate students have impressed me so much. I appreciate their tolerance even when I ask for unusual needs during my study program. I feel so lucky to be part of the department.

Contents

List of Figures

List of Tables

Chapter 1

Introduction

1.1 Challenges in constructing realistically complex Earth models

1.1.1 Interpretation for realistic geophysical models

Geophysical electromagnetic (EM) methods are extremely sensitive to electrical conductivity in the subsurface of the Earth. As such, EM survey methods have been the predominant geophysical methods for delineation of conductive or conductor-associated mineral deposits such as volcanic-associated massive sulphides and uranium deposits (Dyck & West, 1984), and for detection of metal objects such as UXO (unexploded ordnance) buried in the shallow subsurface (Pellerin, 2002). Surveys for groundwater, geothermal resources and environmental monitoring also frequently use EM methods (Everett, 2013). In these applications, the conductivity contrast between a target and its country rock units is sufficiently high, allowing the target's

EM signal to be detectable (Spies & Frischknecht, 1991; Zhdanov, 2009).

Both time-domain and frequency-domain EM survey methods are frequently used in practice. In time-domain EM methods, the EM source signal is generated by inducing a transient electric current within a wire or a loop transmitter, for example, which is then abruptly shut off. The induced secondary EM field from the subsurface can then be observed in the absence of the source signal. In frequency-domain EM methods, however, the source field is continuous and oscillates at a particular period. The measured EM field in practice is a mix of both source signal and induced signal from the subsurface. A comprehensive summary and explanation of geophysical EM theory and basic survey methods is given by Nabighian (1988, 1991).

The immediate output from an interpretation of the collected EM data for a particular region is a distribution of conductivity, or a model of the physical property conductivity, rather than the actual lithology and rock units. To delineate the lithological structures of the subsurface, extra information such as geological knowledge and petrophysical links between the conductivity values and rock types needs to be incorporated into the interpretation. The geophysical data interpretation is itself a quantitative analysis that often consists of forward modelling (computer simulation) and inversion of the surveyed data (Nabighian & Asten, 2002; Oldenburg & Pratt, 2007).

An inversion seeks to recover the conductivity model whose predicted EM responses fit adequately well the actual field data. The predicted EM responses of a candidate model are obtained by forward modelling, which is the problem of that, if the EM survey and configuration parameters and the conductivity distribution are known, how to find a mathematical solution, for example electric and magnetic fields

at specific measurement sites, of Maxwell's equations. One fundamental feature of the inversion is non-uniqueness, meaning that there can be an infinite number of potential models whose EM responses fit the observed data (e.g., Parker, 1977). This is precisely the reason why regularized, or constrained, inversions where particular desirable structures or features of the model are forced to appear are necessary (Tarantola & Valette, 1982).

In terms of constraints for inversion, either known *a priori* physical property values or geometries of geological units can be used (McGaughey, 2007). For the former type of information, one example is the air's conductivity value in a conductivity model with an air layer, which is known and can be treated as a strong constraint. For the latter, examples are surface topography and bathymetry that are often measured by other means. While the physical property information is often straightforward to implement in both forward modelling and inversion, incorporation of known geometry information is more challenging. This is because that in the forward modelling, which is the 'engine' of an inversion run, a simple model discretization such as using rectilinear meshes is capable of readily incorporating physical property values, but requires a non-trivial effort to deal with complex geometries. Often, discretizations using unstructured meshes[1] are needed for representing such geometries, which are ubiquitous in realistic Earth models (Fullagar & Pears, 2007). Indeed, with the increasing power of 3-D geological computer modelling, an integrated geophysical interpretation taking the geological observations such as lithological stratigraphic boundaries and contact surfaces into consideration is needed more than ever (Pears

[1]An unstructured mesh is a tessellation of the problem domain with irregular connectivity and local topology in the mesh.

& Chalke, 2016; Lelièvre & Farquharson, 2016).

1.1.2 State-of-the-art numerical modelling methods

In spite of the demand for constructing realistically complex Earth models from geophysical EM data, 3-D forward modelling and thus inversion algorithms that are capable of doing this have not been reported until recently (e.g., Günther et al., 2006; Newman, 2014; Usui et al., 2017; Jahandari & Farquharson, 2017; Wang et al., 2018). The feasibility of 3-D EM imaging for realistic conductivity models is largely attributed to the adoption of unstructured meshes (e.g., tetrahedral meshes), which permits a relatively easy and efficient discretization of topography and bathymetry (Franke et al., 2007; Nam et al., 2007; Schwarzbach et al., 2011; Ren et al., 2013; Ansari & Farquharson, 2014; Jahandari & Farquharson, 2015). While the importance of using unstructured meshes in forward modelling was acknowledged several decades ago in academia (Coggon, 1971), a routine use of them has become possible only in recent years when open-source mesh generating software has become available (Shewchuk, 1996; Fabri et al., 2000; Si, 2015). With unstructured meshes being increasingly used, there have been corresponding changes in the development of 3-D numerical modelling algorithms.

For a general inhomogeneous conductivity model, only a numerical solution to Maxwell's equations can be sought, which is, to date, mostly sought using integral equation (IE) method, finite difference (FD) method, finite volume (FV) method[2] and finite element (FE) method (Börner, 2010). The IE method was intensively studied

[2]FV method is closely related to FD method, and can be shown to be equivalent to some FD schemes over rectilinear meshes. However, there are also important differences between the two. Therefore, they are treated as two different numerical methods here.

from 1970s to 1990s at a time when computer power was very limited (e.g., Jones & Pascoe, 1972; Hohmann, 1975; Newman et al., 1986). In the IE method, a numerical solution consists of two parts: a primary field which is often computed analytically over a homogeneous or layered Earth model (background model), and a secondary field caused merely by inhomogeneities that are embedded in the background model to complete the 3-D inhomogeneous model. The background model is never discretized, and its EM response can be obtained relatively easily. Only the inhomogeneities are discretized by meshes, either structured or unstructured, and the resultant secondary field is numerically computed. For a single and small localized inhomogeneity, the IE method generates a linear system with a small number of degrees of freedom for solving the secondary field, which can be efficiently solved. However, this linear system has a full and dense matrix, making the method inefficient for modelling complex inhomogeneities. Another challenge of the method is that the background model needs to be some simple, ideal model for which analytical solutions are available. This does however make it difficult to account for complex geometries in a realistic model.

The FD method has been applied to simulate EM fields in engineering problems for a long time (Yee, 1966; Taflove & Umashankar, 1990). Nevertheless, the method had not received significant attention in the geophysical EM community until advanced modern computers were developed in 1990s (Wang & Hohmann, 1993; Mackie et al., 1993; Newman & Alumbaugh, 1995; Streich, 2009). By discretizing the entire model domain with meshes (mostly restricted to be rectilinear meshes), FD methods allow for a more straightforward and general treatment of inhomogeneities in 3-D conductivity models than IE methods. Although the resultant linear system is typically large, the system is symmetric and highly sparse, and thus can be solved

with efficiency. One particular aspect of efficiency is its relatively small memory storage requirement when the linear system is solved with iterative solvers (Saad, 2003), which was paramount in early 1990s considering the computer power at that time. Among various FD schemes, the Yee-scheme (Yee, 1966) is particularly favoured since it faithfully reproduces continuous tangential EM fields while at the same time allows for possible jumps in normal EM fields across the elements' interfaces (material's discontinuities) in a mesh. In terms of modelling EM responses over geometrically complex models, common FD techniques have severe limitations in dealing with highly irregular geometries since the FD approximation is essentially one dimensional and is only feasible over tensor-product, or orthogonal, grids for 2-D and 3-D problems. Curvilinear boundaries have to be approximated by staircase-like rectangular cells, or otherwise non-trivial efforts would be needed (Jurgens et al., 1992). Further, a local refinement of the mesh often propagates to the domain's boundaries, resulting in excessive degrees of freedom in other regions that are not of interest. The refinement propagation issue can be mitigated by using quadtree (2-D case) or octree (3-D case) meshes, but by doing so extra complexities in computation such as interpolation of unknowns due to unconformity of these meshes have to be introduced (e.g., Haber & Heldmann, 2007).

For the FE method, the advantages of supporting unstructured meshes and of generating symmetric and sparse linear systems are both present, making the method a powerful solution to modelling EM responses over Earth models with complicated geometries. Like FD methods, the FE method also discretizes the whole problem domain into subdomains, which are called finite elements. Two important types of FE approaches are node-based (or scalar) and edge-based (or vector) FE methods. In

scalar FE methods, unknowns are defined at the nodes in a mesh, whereas in vector FE methods the unknowns are associated with the edges of cells in the mesh. A notable characteristic of the scalar FE method is that the unknown quantity solved for by the numerical method will be forced to be continuous everywhere in the problem domain, in contrast to the vector counterpart where only the tangential component of the unknown quantity is forced to be continuous (Jin, 2014). Consequently, scalar FE techniques are largely restricted to modelling continuous EM field components or EM potentials for inhomogeneous models (Coggon, 1971; Pridmore et al., 1981; Badea et al., 2001; Li & Key, 2007; Puzyrev et al., 2013).

To date, the FE method appears to be the most suitable modelling method for realistic Earth models with irregular surfaces and topography for example. The reason is that a general treatment of FE approximation of functions over various basic types of subdomains (e.g., triangles and parallelograms in 2-D case, and tetrahedra and prisms in 3-D case) can be used (Brenner & Scott, 2007; Jin, 2014). It almost costs the same amount of effort to implement a FE algorithm using rectilinear meshes as that using completely unstructured meshes. This is in contrast to FD and FV methods, for example. While the FV method can support unstructured meshes, it requires much more effort to do so than that of using a direct FD algorithm with a rectilinear mesh, and it also needs a higher degree of regularity of the unstructured meshes compared to a FE algorithm using the same type of mesh (Jahandari & Farquharson, 2014, 2015).

1.1.3 Benefits and challenges in using unstructured meshes

Aside from being more realistic and consistent with geological models, the benefits of using unstructured meshes in understanding the effects of model geometry on simulated EM data have also been consistently demonstrated. For example, Günther et al. (2006) studied artifacts caused by ignoring topography structure in interpreting direct current (DC) resistivity data. Schwarzbach et al. (2011) modelled marine controlled-source EM (CSEM) responses over a bathymetry conductivity model with a seafloor topography constructed from real data, and confirmed the strong influence of topography on the EM fields. The employment of unstructured tetrahedral meshes allowed Jahandari & Farquharson (2015) and Ansari et al. (2017) to synthesize and compare the predicted EM responses of a massive sulphide ore deposit at Voisey's Bay, Canada, with the actual EM data collected in the field. Another modelling example is the study of Um et al. (2015), where the authors used unstructured meshes in their FE algorithm to investigate the effects of very thin steel casing in a well on borehole-surface CSEM data. In the case of magnetotellurics, Usui (2015) and subsequently Usui et al. (2017) included topography explicitly in the 3-D forward modelling and inversion of real data and demonstrated that the undesired effect of galvanic distortion in interpreting magnetotelluric data can be effectively removed.

With an increasing use of unstructured meshes in tackling 3-D problems, some significant challenges related to mesh generation and FE algorithm implementation have emerged. In order to obtain an accurate numerical solution by the FE method, the mesh used for solving Maxwell's equations is required to be of sufficient quality. In the case of FE algorithms, a quality mesh generally means that its cells or ele-

ments are close to regular polygons or polyhedra. It is understood that the accuracy and efficiency of a FE solution have a strong dependence on the mesh quality, which is often characterized by the ratio of the largest to smallest cell sizes, elongation, dihedral angles and radius-edge ratio of cells, etc, for tetrahedral elements for example (Du et al., 2009; Ansari & Farquharson, 2014). The process in obtaining a FE numerical solution when using iterative matrix equation solvers, which are memory efficient, can be slow or even fail to converge if the mesh quality is not good enough (Ansari & Farquharson, 2014). Even using direct equation solvers, if without necessary quality control in the mesh generation, the resulting mesh can have too many low quality cells which cause numerical interpolation errors in the obtained solution (Schwarzbach et al., 2011). For many real-world Earth models that contain rough and highly irregular changes of contact surfaces and topographies, the requirement of quality meshes thus poses a significant challenge in the mesh generation.

Even with the aid of third-party automated mesh generating software, significant difficulties are still faced. If a quality mesh is generated without guidance, often excessive elements are observed as a result of overmeshing, making the FE-based forward modelling intractable (Nalepa et al., 2016; Nalepa, 2016). An example of meshing a thin layer of hydrocarbon reservoir with possible excessive cells is illustrated in Fig 1.1 (Dunham et al., 2018). For an experienced modeller, some rules of thumb can be used. For example, by deploying denser and smaller elements at the EM transmitters and receivers and in other regions where EM fields are expected to change rapidly, and coarser, larger elements elsewhere, the total number of elements can be made to be affordable for given computing resources (Key & Ovall, 2011). However, such experience-guided discretization easily becomes non-trivial for large-

scale models with multiple inhomogeneities where changes of EM fields are harder to predict (Schwarzbach et al., 2011; Nalepa et al., 2016). A practical solution to such manual refinement or coarsening of a mesh is adaptive mesh generation methods (Oden & Prudhomme, 2001). Such adaptive meshing techniques can refine or coarsen some specific parts of an existing mesh based on error estimators constructed from the current numerical solution. As a result, minimum user interference is required in designing a quality mesh without too many excessive cells. One example of adaptive meshing techniques is the goal-oriented adaptive refinement method, which by far has been favoured in 2-D and 3-D EM modelling problems (see, e.g., Franke et al., 2007; Key & Ovall, 2011; Schwarzbach et al., 2011; Ren et al., 2013; Grayver & Burg, 2014).

Nevertheless, adaptive meshing schemes for unstructured elements in 3-D problems are computationally expensive and sometimes even prohibitive. A new mesh resulting from local refinement or coarsening of an existing mesh is obtained either by subdivision or merging of local elements (e.g., Key & Ovall, 2011; Schwarzbach et al., 2011), or by remeshing the whole problem domain (e.g., Ren et al., 2013). The benefit of the former strategy is that it has good stability and only part of the original mesh needs to be updated. The difficulty is that complicated mapping of corresponding elements between the two meshes, and thus updates of degrees of freedom, are required. As the topology of the original mesh is changed, noncomformal elements may also arise, adding additional interpolation computation. In the latter strategy, the aforementioned issues of mapping are avoided, but the remeshing can be time-consuming since the whole domain needs to be remeshed at each iteration of refinements. Furthermore, the remeshing process suffers from possible breakdown of the

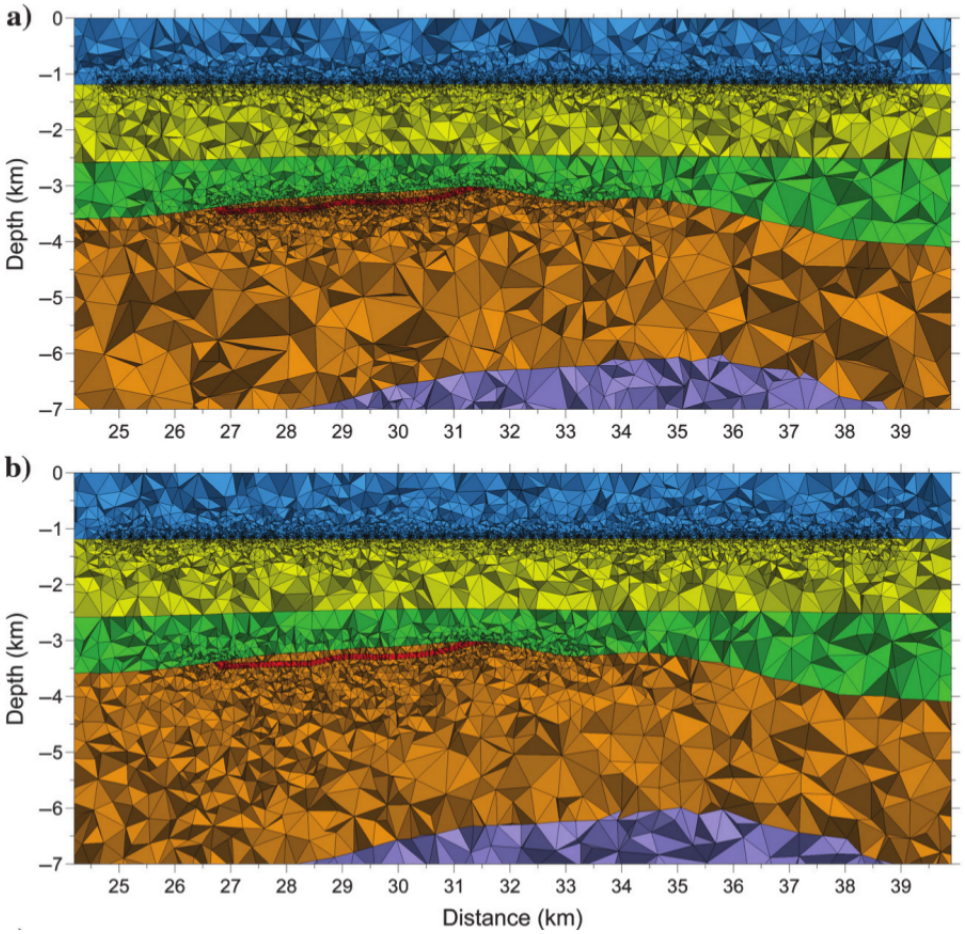

Figure 1.1. Two different tetrahedral meshes for the same multi-layer marine hydrocarbon reservoir model. The thin hydrocarbon layer is shown in red in both meshes. The mesh shown in (a) has about 1 million more cells than the mesh in (b), with the latter mesh being generated with better edge length constraints. From Fig 7 in Dunham et al. (2018).

mesh generator which can be attributed to various factors such as model complexity, software bugs, memory limits, etc.

To summarize, the FE method in conjunction with unstructured meshes appears to be the most suitable solution among mesh-based methods to modelling 3-D EM responses over real-world Earth models with irregular geometries. However, there have been observed difficulties arising mainly from using quality meshes in the FE method, which potentially hampers its application towards dealing with realistic Earth models. This observation motivates the author of this thesis to investigate a fundamentally different numerical method, that is, the meshfree method, which does not require a mesh in obtaining a numerical solution, and its applicability in solving the above 3-D EM modelling problems.

1.2 Meshfree discretization in forward modellings

A key feature of meshfree discretizations is that only a cloud of unconnected points[3] are required in deriving a numerical solution to partial differential equations such as Maxwell's equations. As a consequence, numerical methods that can work with meshfree discretizations in the modelling task have their own distinct features and are termed *meshfree methods*. This is in contrast to traditional numerical methods that rely on a tessellated mesh (hence, mesh-based methods) in order to acquire a numerical solution with a desired accuracy. It is the mesh reliance of mesh-based methods that requires an Earth model be finely meshed with voxel-like cells or elements (Fig 1.2a and Fig 1.2b). However, such fine scale meshes are solely for the

[3]In the literature of meshfree studies, both 'node' and 'point' are interchangeably used to refer to the basic element of a meshfree discretization. In this thesis, the word 'point' is preferred.

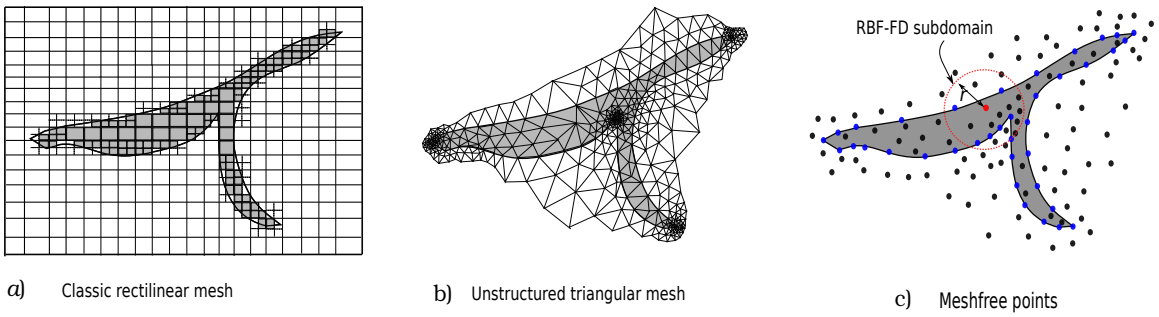

Figure 1.2. Schematic illustration of model discretizations for 2-D irregular geometries using (a) rectilinear mesh with local quadtree refinements, (b) unstructured triangular mesh and (c) meshfree points.

purpose of geophysical data modelling and are not necessary in describing the geometry of geological structures. In describing a geological model, much rougher 3-D meshes, for example a mesh with only outlines of different rock units, are adequate. The interior volumes of rock units even need not be meshed. These rough meshes are precisely the outputs and/or inputs from geological interpretations. In this sense, it can be viewed that there are two meshes involved in the context of forward modelling geophysical data: one is the mesh describing the geometries of different rock units such as those for a conductor embedded in the resistive subsurface in the half space model ('model mesh', Fig 1.3a), and the other one used to carry out forward modelling which is often required to be able to sufficiently sample the function values of the quantity of the forward problem ('numerical mesh', Fig 1.3b). Hereinafter, all discussions about meshes will refer to the latter case.

A meshfree discretization serves the same purpose as that of a tessellated mesh (Fig 1.2c) used for a good numerical solution. For this reason, the discretization is also required to be fine enough in most scenarios (Fig 1.3c). However, in the case of a meshfree discretization, there are now important advantages regarding the

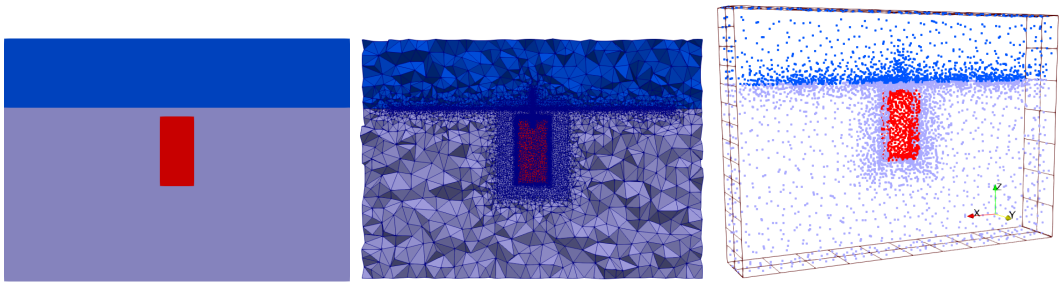

(a) (b) (c)

Figure 1.3. Different spatial discretizations of an Earth model in mesh-based and meshfree numerical methods: (a) a mesh describing the example Earth model which is shown as the cross section of a conductor (in red) embedded in the half space (in grey); (b) an example mesh (unstructured tetrahedra) used for solving the equations if using mesh-based methods; (c) a cloud of points used for solving the equations when using meshfree methods.

mesh generation and mesh refinement issues over traditional mesh-based numerical methods:

- The generation of a set of unconnected points, even with comparable regularity constraints of a fine mesh, is more straightforward and requires less effort.

- The generation of quality points is believed to be more robust than the generation of quality meshes (Du et al., 2002; Fornberg & Flyer, 2015b; Slak & Kosec, 2019), allowing for a more robust adaptive refining ('remeshing') than for mesh-based methods.

- Adaptive refining and/or coarsening of a meshfree discretization is more computationally efficient than the similar process in mesh-based numerical methods, since an addition or deletion of some points will not affect the rest of the points (Duarte & Oden, 1996b; Rabczuk & Belytschko, 2005). This means that there will be no unconformity issues between the old degrees of freedom and the new

ones.

These advantages provide the basis for overcoming the aforementioned challenges in modelling EM data over complex Earth models when using mesh-based methods such as FE. Meshfree numerical methods for data simulation were originally developed in research fields other than geophysical applications. The investigation in this thesis is therefore focused on how, given a meshfree point discretization, can an appropriate formulation of Maxwell's equations be solved using such a discretization.

1.3 Thesis overview

In the following, Chapter 2 firstly presents a review of meshfree numerical methods. Basic meshfree function approximation methods as well as state-of-the-art meshfree numerical methods are introduced. The meshfree method investigated in this thesis is also elaborated with implementation details and justifications for it to be used for geophysical data modelling. In Chapter 3, with the background problem being that of numerically modelling gravity data, a convergence analysis of the meshfree method based on numerical evidence is presented, which is followed by the investigation of how to determine the stencil size (the number of points in a meshfree subdomain) in implementing the meshfree method. A comparison study using the meshfree approach and a more traditional finite element algorithm is also provided. This part of work has been published as a peer-reviewed paper (Long & Farquharson, 2019a). Chapter 4 presents the feasibility and applicability study of the proposed meshfree method in numerically simulating 3-D magnetotelluric data, a commonly used EM survey approach that uses passive EM source signals. The feasibility of using the

meshfree method in the frame of EM potential equations is theoretically analyzed first and then demonstrated with numerical results. The results of this chapter have been published in a separate paper (Long & Farquharson, 2019c). In Chapter 5, the mixed meshfree method proposed in modelling magnetotelluric data is further extended in order to solve the forward modelling of controlled-source EM responses over a general 3-D conductivity model. The incorporation of singular EM source functions in the meshfree method is investigated and numerically tested. Part of the work in this chapter has been summarized in previous SEG Expanded Abstracts (Long & Farquharson, 2017, 2019b). Finally, Chapter 6 and 7 present further discussions and conclusions, respectively, of the above studies.

Chapter 2

A review of meshfree numerical methods

In this chapter, function approximation in a mathematical background is presented first, which is followed by a review of meshfree numerical methods for solving general partial differential equations in the literature. The meshfree method investigated in this thesis is reviewed with more details regarding its development history and algorithm implementation, along with the justifications of employing it in simulating geophysical data.

2.1 Meshfree function approximation

Meshfree function approximation is fundamental to meshfree numerical methods for solving partial differential equations (PDEs). The problem of meshfree function approximation can be stated as: given n discrete data sites with positions $\mathbf{r}_i$ $(i = 1, \ldots, n)$ and their associated function values $\{f_i\}_{i=1}^n$, find an approximant $\hat{f}(\mathbf{r})$

to the unknown function f, which is assumed to be sufficiently smooth, such that

$$||\hat{f}(\mathbf{r}) - f(\mathbf{r})||_p, \quad \mathbf{r} \in \Omega \subset \mathbb{R}^3, \quad \hat{f}, f \in \mathbb{R}, \tag{2.1}$$

is minimized over the problem domain Ω. $||\cdot||_p$ is a chosen norm, and $\mathbb{R}^3$ is the 3-D space of real values. Ω is the support of f and is also called a meshfree subdomain when only a set of local points are employed to construct function approximation (see Fig 2.1). Eq (2.1) states a general measure of the quality of the approximation. To obtain a good approximation, the approximate $\hat{f}(\mathbf{r})$ is often expanded using known and simple functions.

The assumption of a sufficient smoothness of the unknown function allows a general treatment of the approximation problem and systematic developments of mathematical theories (e.g., error analysis, see Buhmann, 2003; Fasshauer, 2007). With this assumption, the approximant, $\hat{f}(\mathbf{r})$, can be expanded as a linear combination of some basis functions ϕ

$$\hat{f}(\mathbf{r}) = \sum_{i=1}^{M} \phi_i(\mathbf{r}) \cdot c_i, \tag{2.2}$$

where c_i are coefficients to be determined, and M is the number of terms of basis functions. Depending on the choice of types of basis functions, M may or may not be equal to n which is the number of data sites.

In the context of meshfree approximation where the data sites are discrete points in 3-D space, two types of basis functions are commonly used: monomial functions and radial functions. Other rational functions are possible in principle, but they are not as widely used as these two types (Fasshauer, 2007). The approximation

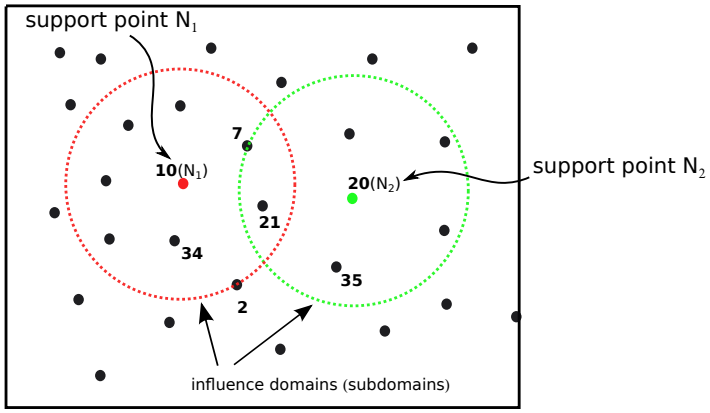

Figure 2.1. Schematic illustration of meshfree subdomains consisting of scattered points. A set of local points within a neighbourhood (outlined by dotted circles) of a point (denoted as support point) comprises the subdomain for that point.

based on monomial functions is termed moving least squares (MLS) method, and the counterpart based on radial basis functions is termed radial basis function-based method (Fasshauer, 2007). Note the use of monomial functions in approximation over meshed subdomains is the foundation of the mesh-based numerical methods such as finite element and classical grid-based finite difference methods (Fig 2.2 (a) and (b)).

In the method of MLS, a complete set of monomial functions is typically used for accuracy. For example, a complete set of linear monomials in 3-D space is $[1, x, y, z]$ with $M = 4$, and a complete set of quadratic monomials is $[1, x, y, z, xy, yz, xz, x^2, y^2, z^2]$ with $M = 10$. The approximant $\hat{f}$ constructed using MLS is determined by minimizing the functional

$$J = \sum_{k=1}^{n} w(\mathbf{r}, \mathbf{r}_k) \left(\sum_{i=1}^{M} \phi_i(\mathbf{r}) \cdot c_i - f_k \right)^2 , \tag{2.3}$$

where c_i are the coefficients to be determined, $\mathbf{r}_k$ is the position of kth point in a subdomain, and $w(\mathbf{r}, \mathbf{r}_k)$ is a weight function which is predetermined and is chosen such that $w > 0$. In order to obtain a unique solution to eq (2.3), $n \geqslant M$ is required

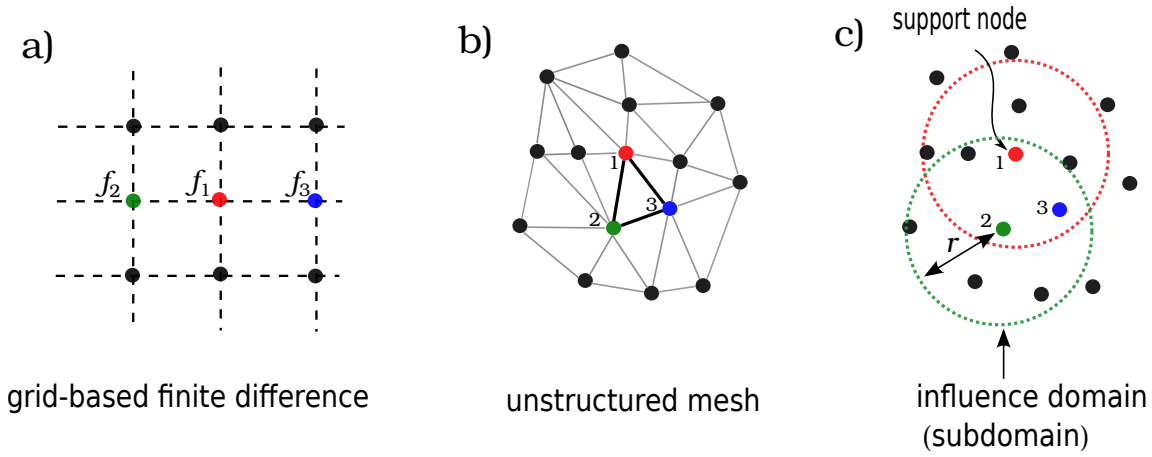

Figure 2.2. Schematic illustration of different discretizations in mesh-based and meshfree approximation methods. Shown above are **(a)** a grid-based finite difference stencil, **(b)** an unstructured mesh and **(c)** two meshfree subdomains.

to hold. In practice, $n > M$ is often the case and c_i are solved in a least squares manner (see Nguyen et al., 2008, and references therein). The weight function is required here so that the linear system of equations from least squares averaging has a nonsingular matrix for high dimensional (2-D and 3-D) data sites, which makes MLS feasible for multivariate function approximation, or equivalently, for high dimensional meshfree function approximation. However, in 2-D and 3-D situations, the data sites, or meshfree points in a subdomain are still required to possess a certain degree of regularity such as not being collinear points (Fig 2.3), regardless of the choice of w.

In the method of approximation by radial basis functions (RBFs), which are explained with more details in Sections 2.4 and 2.4.1, $\phi_i(\mathbf{r})$ are translations of a chosen RBF at the n points. Since many RBFs that are used in practical meshfree function approximation are positive definite functions, standard Lagrange-type interpolation conditions $(\hat{f}(\mathbf{r}_i) = f_i = f(\mathbf{r}_i), i = 1, \cdots, n)$ can be employed to determine c_i in eq (2.2). In this case, $n = M$ in each subdomain.

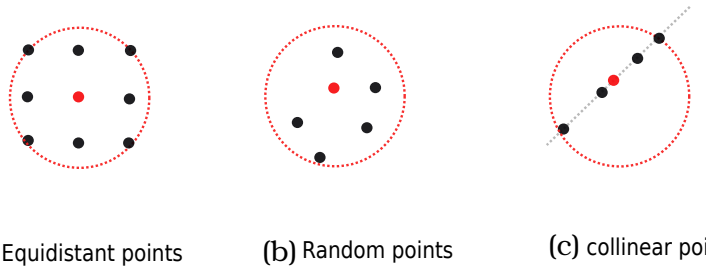

Figure 2.3. Some point arrangements in a 2-D meshfree subdomain: **(a)** regular, equidistant points; **(b)** randomly distributed points and **(c)** collinear points. The red point is the support point.

2.2 Meshfree methods for solving PDEs

Different meshfree numerical methods have been developed to solve PDEs arising from various applications. Although early applications of meshfree methods were primarily focused on fluid and solid mechanics and astrophysics, applications in many other fields have been reported (see the reviews by Belytschko et al., 1996; Li & Liu, 2002; Nguyen et al., 2008; Chen et al., 2017). Over the years, there have been numerous meshfree PDE-solving approaches proposed which are often named by the proposers' practical applications, causing a remarkable inconsistency in the nomenclature of meshfree numerical methods (see, e.g., the various names listed in Chen et al., 2017). This is sometimes inconvenient and even misleading for researchers and practitioners to understand the techniques in those approaches. To alleviate this issue, an explanation of the essence of those meshfree methods is presented here.

Similar to mesh-based numerical methods, meshfree methods are generally categorized as two groups from the point of view of deriving a numerical solution: strong form-based methods (SFMs) and weak form-based methods (WFMs). In the process of seeking a numerical solution to PDEs (e.g., $Df = g$, g is a known function) over a bounded domain, the action of a differential operator D on the unknown function f,

Df, will be approximated as the result of a linear combination of a certain number (e.g., k) of local function values

$$Df \approx \sum_{j=1}^{k} c_j f_j. \tag{2.4}$$

In SFMs, the coefficients c_j in eq (2.4) are obtained by satisfying the above approximation at discrete data sites (meshfree points here). In WFMs, however, the PDE under consideration is satisfied in an averaged sense (thus, the 'weak' form)

$$\int_{\Omega'} v \cdot (Df - g)\, dV = 0, \quad \Omega' \subset \mathbb{R}^3, \tag{2.5}$$

where v is often referred to as test function or weight function, and Ω' is the problem domain.

It can be observed from eqs (2.4) and (2.5) that in either type of the numerical methods, approximation of the unknown function f needs to be carried out before a numerical solution can be found, and there are a number of meshfree function approximation approaches available in addition to the two widely used ones mentioned in the previous section. In the case of WFMs, aside from different ways of approximating f, there are different methods to partition the problem domain into subdomains (subdomains for function approximation and for weak form integration may be different). There are also different ways to choose the test function, for which two commonly used approaches are Galerkin (also known as Bubnov-Galerkin or standard Galerkin) method and Petrov-Galerkin method (Atluri & Zhu, 1998; Gockenbach, 2006).

Differing in these aspects in finding a numerical solution, some notable strong

form-based meshfree methods include smoothed particle hydrodynamics (Gingold & Monaghan, 1977), generalized finite differences (Liszka & Orkisz, 1980), the vortex method (Leonard, 1985), finite-volume particle-in-cell method (Munz et al., 1999), meshless collocation method (Kansa, 1990a) and RBF-based finite difference (RBF-FD, Tolstykh & Shirobokov, 2003). Similarly, some notable weak form-based meshfree methods are diffuse element method (Nayroles et al., 1992), element free Galerkin method (EFG, Belytschko et al., 1994), reproducing kernel particle method (Liu et al., 1995), h-p cloud method (Duarte & Oden, 1996a), partition of unity method (Melenk & Babuška, 1996), free mesh method (Yagawa & Yamada, 1996), meshless local Petrov-Galerkin method (MLPG, Atluri & Zhu, 1998), and radial point interpolation method (RPIM, Wang & Liu, 2002a). In the past two decades, improvements to the aforementioned methods have been developed that are devoted to enhancing particular aspects in computer implementations such as efficiency and convergence rate (Chen et al., 2017). One important example of these improvements is how to accurately and efficiently carry out volume or surface integration over meshfree subdomains in WFMs. This is because when using meshfree function approximation techniques, the resultant shape functions are often high-order rational functions, as opposed to low-order polynomials that typically appear in mesh-based methods (e.g., finite element and integral equation methods), and as such the integrals in eq (2.5) have to be carried out numerically instead of analytically.

2.3 Applications in geophysics

Applications of meshfree methods in geophysics were reported as early as the 1970s (Hardy, 1971). However, meshfree methods are still not widely known to the geophysical community. As mentioned in the Introduction of the thesis, a major benefit of using meshfree numerical methods is that irregular geometries can be relatively easily represented. Another advantage using meshfree methods is that high order accuracy and/or convergence rate can be achieved by a discretization with fewer degrees of freedom than that using traditional mesh-based methods. The latter is due to the high order smoothness of the meshfree approximant or interpolant. To date, there have been increasing applications of meshfree methods in forward modelling geophysical data. For example, Jia & Hu (2006) investigated the numerical accuracy of applying EFG to simulate 2-D time-domain seismic wave fields. Martin et al. (2015) demonstrated that using RBF-FD with multiquadric RBFs can lead to a high-order h convergence in modelling 2-D seismic wave propagation. Similarly, Takekawa et al. (2015) proposed to use a polynomial-based meshfree FD approach to solve the problem of frequency-domain elastic wave modelling, which is further studied by Takekawa & Mikada (2016, 2018). Li et al. (2017) studied time-space-domain elastic wave modelling using RBF-FD for greater temporal accuracy, which uses the same RBFs as in Martin et al. (2015). For the modelling of EM data, Wittke & Tezkan (2014) presented an application of MLPG for simulating 2-D magnetotelluric (MT) responses of inhomogeneous conductivity models. The same MT numerical problem was also studied by Li et al. (2015) using an implementation of EFG and by Ji et al. (2018) using a realization of RPIM.

The above geophysical studies using meshfree techniques involve, however, only 2-D problems and only employ uniform or quasi-uniform (unstructured but uniform density of points) meshfree point discretizations. In this thesis, 3-D geophysical data modelling problems are addressed and the use of unstructured meshfree discretizations is investigated. I have adopted the strong form-based variant of RBF-FD for such purpose. This choice is based on the facts that: first, RBF-FD allows for arbitrarily distributed meshfree points to be used in discretizing Earth models, and therefore is capable of dealing with complex and realistic geometries of models; second, RBF-FD is free from integrations when transforming continuous PDEs into discrete algebraic equations, effectively circumventing difficulties arising from numerical integrations (quadrature and/or cubature) using WFMs (e.g., EFG and MLPG).

2.4 RBF-based meshfree methods

A radial basis function (RBF) is defined as a radially symmetric (with respect to its centre) rational function. An RBF is mathematically denoted in general as $R(r) = R(||\mathbf{r} - \mathbf{r}_i||_{l_2})$ throughout this thesis, where $\mathbf{r} = (x, y, z)$ in 3D is the argument (variable) and $\mathbf{r}_i$ is its centre[1]. The radial symmetry means that the value of the function only depends on the Euclidean distance (r) between the argument and its centre. Therefore, any rotations of an RBF does not change the function value. RBFs are particularly suitable for multivariate function approximation based on scattered data (Buhmann, 2003). The importance of these properties of RBFs in the context of meshfree function approximation and PDE-solving problems is two-fold. First, RBFs

[1]The centre variable of an RBF always appears at the second place within $||\cdot||$ throughout the thesis.

can be directly used in the function approximation with standard Lagrange interpolation conditions, that is, the approximant $\hat{f}$ of an unknown function f constructed in this way passes through all discrete function values $\hat{f}(\mathbf{r}_i) = f_i = f(\mathbf{r}_i)$. This enables a straightforward and simple implementation of Dirichlet-type boundary conditions in solving PDEs, for which extra boundary treatments would otherwise be needed if using polynomial-based meshfree approximation (Atluri & Shen, 2002). Second, possible matrix singularity issues of the resultant linear system in multidimensional meshfree approximation are readily avoided, even for extreme point arrangements (e.g., collinear points in Fig 2.3, Section 2.1). Extreme point arrangements will cause singularity issues in the polynomial-based meshfree approximation such as MLS (Wang & Liu, 2002a).

Although RBFs were used for solving problems of scattered data interpolation as early as the 1970s (e.g., Hardy, 1971, for geological mapping), applications of using RBF-based approximation in solving PDEs had not been reported until 1990s (Kansa, 1990a,b). The method used by Kansa (1990a) is essentially a global approximation of differential operators, or derivatives, in a PDE by using the RBF-based meshfree approximation, leading to a full, dense and unsymmetrical matrix in the resultant linear system of equations. Since his pioneering works, many researchers have been seeking more efficient RBF-based numerical methods that for example are able to generate a sparse and/or symmetric global matrix equation such that larger modelling problems could be tackled. One noticeable development as a result of these effort is the proposal of using compactly supported[2] RBFs in Kansa's method, which originally used global RBFs (see, e.g., Schaback & Wendland, 1999). The use of compactly

[2]A compactly supported function is a function whose non-zero domain is compact.

supported RBFs greatly improves the sparsity of the matrix of the linear system of equations.

A more revolutionary idea is, however, using the RBF-based approximation for differential operators in a finite difference way, which was to the best of my knowledge independently proposed by Tolstykh & Shirobokov (2003), Shu et al. (2003), and Larsson & Fornberg (2003). The most significant difference between this new idea and previous methods is that the approximation of derivatives only occurs within local subdomains, rather than happening globally (using all points). The nature of local approximation ensures that the final linear system always has a sparse matrix, and at the same time allows for possibilities of constructing symmetric coefficient matrices. In spite of different terms in nomenclature employed in the literature, the numerical method based on this idea is mostly called RBF-based finite difference method (RBF-FD) (Fornberg & Flyer, 2015a). Throughout this thesis, 'RBF-FD' is used to refer to such a numerical method for which the implementation is further described in detail in Section 2.4.1.

Compared to mesh-based numerical methods such as finite element and grid-based finite difference, one aspect to note is that theoretical developments of RBF-FD techniques in terms of error analysis (e.g., convergence) in the context of solving various PDEs are less mature and still being studied. However, significant advances have been reported in the past two decades. For example, Wright (2003) pointed out that although RBF-FD is conceptually similar to classical grid-based FD, the differentiation weights (i.e., RBF-FD weights) in the RBF-FD frame enforce the resultant difference formula to be exact for a given RBF, whereas the differentiation weights in the grid-based FD scheme enforce the resultant difference formula to be exact for

polynomials up to some degree. Performance evaluations and convergence analyses (under refinements of discretization) of RBF-FD demonstrated via numerical results are provided by, for example, Ding et al. (2005), Wright & Fornberg (2006), Bayona et al. (2010) and Davydov & Oanh (2011a). Studies focusing on the numerical analysis of RBF-FD involving two major groups of RBFs (see Table 2.1) have revealed new insights regarding adding polynomials in RBF-based approximation (Flyer et al., 2016a,b; Bayona et al., 2017). General mathematical analyses, albeit more theoretical, regarding convergence and error bounds in solving PDEs have also been reported steadily (e.g., Fasshauer, 1996; Franke & Schaback, 1998; Schaback, 2007; Davydov & Schaback, 2016; Schaback, 2017).

2.4.1 RBF-FD

RBF-FD uses the strong form of differential equations and generalizes classical grid-based FD methods from lattice-based grids to arbitrarily scattered points. In RBF-FD, a differential operator acting on a function (e.g., $\nabla^2\phi$ with ϕ as gravitational potential) is directly approximated as a linear combination of local function values, which can be written as

$$D\ f|_{\mathbf{r}=\mathbf{r}_i} \approx \sum_{j=1}^{n} c_j f_j, \tag{2.6}$$

where D is the operator, $f = f(\mathbf{r})$ is the function, f_j are discrete function values, and c_j are approximation coefficients or weights. The subscript $\mathbf{r} = \mathbf{r}_i$ indicates that the approximation takes place at a specific position. The mathematical form in eq (2.6) can be equally used for an approximation of operators when using a classical grid-based FD approach. However, a classical grid-based FD approach approximating Df

is essentially one dimensional, and finding c_j in eq (2.6) is equivalent to enforcing that the corresponding FD formula (e.g., 3-point central FD formula) is exact for monomial functions 1, x, x^2,..., up to a desired degree. In the RBF-FD case, the approximation in eq (2.6) is possible for higher dimensional (e.g., 2-D and 3-D) spaces, and finding the weights is equivalent to enforcing that the RBF-FD formula is exact for translations of a given RBF (Fornberg & Flyer, 2015a). In practice, when determining the RBF-FD weights c_j in the meshfree case, the (possibly unknown) function, f, is itself approximated using a Lagrange-type interpolant[3] first. The RBF-based interpolant $s(\mathbf{r})$ is written as

$$s(\mathbf{r}) = \sum_{k=1}^{n} R(||\mathbf{r} - \mathbf{r}_k||) \cdot b_k, \quad \mathbf{r} \in \mathbb{R}^3, \tag{2.7}$$

where $||\cdot||$ is the l_2 norm, $R(||\mathbf{r} - \mathbf{r}_k||)$ is an RBF, $\mathbb{R}$ is the space of real values, and n is the number of local points (also the number of local function values) within a meshfree subdomain (see Fig 2.1). The interpolation coefficients, b_k, are obtained by enforcing the standard Lagrange interpolation condition

$$s(\mathbf{r}_k) = f_k = f(\mathbf{r}_k), \qquad k = 1, 2, \cdots, n \tag{2.8}$$

which is equivalent to solving the local linear system

$$\begin{pmatrix} R(||\mathbf{r}_1 - \mathbf{r}_1||) & R(||\mathbf{r}_1 - \mathbf{r}_2||) & \cdots & R(||\mathbf{r}_1 - \mathbf{r}_n||) \\ R(||\mathbf{r}_2 - \mathbf{r}_1||) & R(||\mathbf{r}_2 - \mathbf{r}_2||) & \cdots & R(||\mathbf{r}_2 - \mathbf{r}_n||) \\ \vdots & \vdots & \ddots & \vdots \\ R(||\mathbf{r}_n - \mathbf{r}_1||) & R(||\mathbf{r}_n - \mathbf{r}_2||) & \cdots & R(||\mathbf{r}_n - \mathbf{r}_n||) \end{pmatrix} \begin{pmatrix} b_1 \\ b_2 \\ \vdots \\ b_n \end{pmatrix} = \begin{pmatrix} f_1 \\ f_2 \\ \vdots \\ f_n \end{pmatrix}. \tag{2.9}$$

[3]The interpolant, rather than approximant, is used here to indicate that the approximation here is derived using interpolation conditions, as described in the following.

Eq (2.9) can be written as a compact matrix form:

$$\mathbf{R}\mathbf{b} = \mathbf{F}, \tag{2.10}$$

where $\mathbf{R}$ is the symmetric matrix at the left-hand side of eq (2.9), $\mathbf{b} = (b_1\ b_2\ \cdots\ b_n)^T$ is the vector of the interpolation coefficients and $\mathbf{F} = (f_1\ f_2\ \cdots\ f_n)^T$ the function value vector. The superscript T indicates the transpose of a vector or matrix unless otherwise indicated.

It is seen here that $\mathbf{R}$ is only determined by the predefined point distribution once a type of RBF is chosen. To ensure a unique solution to eq (2.10), the matrix $\mathbf{R}$ needs to be nonsingular. This is proven to be true for many positive definite RBFs, which include the examples listed in Table 2.1 (Buhmann, 2003; Fasshauer, 2007). If the inverse of $\mathbf{R}$ exists, the unique solution to eq (2.10) is $\mathbf{b} = \mathbf{R}^{-1}\mathbf{F}$. Substituting this relation back into eq (2.7) leads to the form of interpolant in terms of *meshfree shape functions*:

$$s(\mathbf{r}) = \sum_{k=1}^{n} N_k(\mathbf{r}) f_k, \tag{2.11}$$

where the shape functions $N_k(\mathbf{r}) = N_k(x, y, z)$ are non-polynomial rational functions and satisfy $N_k(\mathbf{r}_k) = 1$ and $N_k(\mathbf{r}_l) = 0$ $(l = 1, \ldots, k-1, k+1, \ldots, n)$.

If the vector of local function values $\mathbf{F}$ is known as well, which is common in function approximation, a unique interpolant can then be obtained. However, in approximating differential operators in the context of solving PDEs, as in the case of finding RBF-FD weights, the function f, therefore $\mathbf{F}$, is typically unknown. This means that eq (2.10) is not the right one to solve in order to obtain RBF-FD weights;

instead, a different local linear system of equations should be solved.

To demonstrate, the action of a differential operator on f is now expanded using the interpolant in eq (2.7) as

$$\begin{aligned} Df|_{\mathbf{r}=\mathbf{r}_i} &\approx \sum_{k=1}^{n} DR(||\mathbf{r}-\mathbf{r}_k||)|_{\mathbf{r}=\mathbf{r}_i} \cdot b_k \\ &= \begin{pmatrix} b_1 & \cdots & b_n \end{pmatrix} \begin{pmatrix} DR(||\mathbf{r}-\mathbf{r}_1||)|_{\mathbf{r}=\mathbf{r}_i} \\ \vdots \\ DR(||\mathbf{r}-\mathbf{r}_n||)|_{\mathbf{r}=\mathbf{r}_i} \end{pmatrix} \\ &= \mathbf{b}^T \cdot \mathbf{P}_{Radial}, \end{aligned} \tag{2.12}$$

where $\mathbf{P}_{Radial}^T = (DR(||\mathbf{r}-\mathbf{r}_1||), \cdots, DR(||\mathbf{r}-\mathbf{r}_n||))|_{\mathbf{r}=\mathbf{r}_i}$, and $\mathbf{b}$ is the same vector as in eq (2.10). Next, replacing $\mathbf{b}$ in eq (2.12) with $\mathbf{R}^{-1}\mathbf{F}$ results in

$$Df|_{\mathbf{r}=\mathbf{r}_i} \approx \mathbf{F}^T\mathbf{R}^{-1}\mathbf{P}_{Radial}. \tag{2.13}$$

Denoting the product of $\mathbf{R}^{-1}$ and $\mathbf{P}_{Radial}$ in eq (2.13) as a vector (e.g., $\mathbf{c}$), it is clear that

$$Df|_{\mathbf{r}=\mathbf{r}_i} \approx \mathbf{F}^T\mathbf{c} = \sum_{j=1}^{n} c_j f_j, \tag{2.14}$$

and

$$\mathbf{R}\mathbf{c} = \mathbf{P}_{Radial}. \tag{2.15}$$

As a result, solving eq (2.15) for each meshfree subdomain gives rise to its RBF-FD weights c_j. Note that eq (2.15) only differs from eq (2.9) in the right-hand side vector.

The interpolant in eq (2.7) can be enriched with low-order monomial basis func-

Table 2.1. Common types of RBFs. The infinitely smooth RBFs include a shape parameter $c > 0$. r is the Euclidean distance between two points $\mathbf{r}_1$ and $\mathbf{r}_2$: $r = ||\mathbf{r}_1 - \mathbf{r}_2||_{l_2}$. N^+ is the space of positive integers.

Type of basis function	**Radial function** $R(r)$
Finite-smoothness RBFs	
Generalized Duchon spline	$r^{2k}\log r, \quad k \in N^+$
Polyharmonic spline (PHS)	$r^{2k-1}, \quad k \in N^+$
Infinitely smooth RBFs	
Gaussian (GA)	$e^{-(cr)^2}$
Multiquadric (MQ)	$(c^2 + r^2)^{\frac{1}{2}}$
Inverse-multiquadric (IMQ)	$(c^2 + r^2)^{-\frac{1}{2}}$

tions. In general, the enrichment of monomials improves stability and convergence under h refinement (i.e., under different cell sizes in the mesh, here under different inter-nodal distances). In the 3-D case, a complete monomial basis of linear order is $[1, x, y, z]$, and $[1, x, y, z, xy, yz, xz, x^2, y^2, z^2]$ for quadratic order. Hereinafter, these monomial basis functions are generally called polynomials based on the facts that any polynomial function can be constructed from monomial basis functions and polynomials are more commonly used. In this section, only the demonstration using the RBF-based approximation enriched with 3-D linear polynomials is given. However, the procedure can be equally and straightforwardly applied to higher-order polynomial enrichment situations. The enriched interpolant thus becomes

$$s(\mathbf{r}) = \sum_{k=1}^{n} R(||\mathbf{r} - \mathbf{r}_k||) \cdot b_k + d_0 + d_1 x + d_2 y + d_3 z, \tag{2.16}$$

with d_i $(i = 0, 1, 2, 3)$ as additional degrees of freedom. The determination of the additional coefficients requires extra equations, which are provided by applying the

unisolvency conditions (Buhmann, 2003)

$$\sum_{k=1}^{n} b_k = \sum_{k=1}^{n} b_k x_k = \sum_{k=1}^{n} b_k y_k = \sum_{k=1}^{n} b_k z_k = 0 \tag{2.17}$$

at the n local points. Here, x_k, y_k and z_k are the Cartesian coordinates of the kth point. Now a unique solution to the approximation problem in eq (2.16) is guaranteed. The updated local linear system of equations then becomes

$$\begin{pmatrix} & & & 1 & x_1 & y_1 & z_1 \\ & \mathbf{R} & & \vdots & \vdots & \vdots & \vdots \\ & & & 1 & x_n & y_n & z_n \\ 1 & \cdots & 1 & & & & \\ x_1 & \cdots & x_n & & \mathbf{0} & & \\ y_1 & \cdots & y_n & & & & \\ z_1 & \cdots & z_n & & & & \end{pmatrix} \begin{pmatrix} b_1 \\ \vdots \\ b_n \\ d_0 \\ d_1 \\ d_2 \\ d_3 \end{pmatrix} = \begin{pmatrix} f_1 \\ \vdots \\ f_n \\ 0 \\ 0 \\ 0 \\ 0 \end{pmatrix}, \tag{2.18}$$

and can be expressed in a compact matrix form as

$$\begin{pmatrix} \mathbf{R} & \mathbf{P} \\ \mathbf{P}^T & \mathbf{0} \end{pmatrix} \begin{pmatrix} \mathbf{b} \\ \mathbf{d} \end{pmatrix} = \begin{pmatrix} \mathbf{F} \\ \mathbf{0} \end{pmatrix}, \tag{2.19}$$

where $\mathbf{P}$ denotes the upper right blocky submatrix

$$\mathbf{P} = \begin{pmatrix} 1 & x_1 & y_1 & z_1 \\ \vdots & \vdots & \vdots & \vdots \\ 1 & x_n & y_n & z_n \end{pmatrix}, \tag{2.20}$$

and $\mathbf{d}$ denotes the vector $(d_0\ d_1\ d_2\ d_3)^T$.

Similar to the situation without polynomial enrichment, eq (2.19) is not solvable for seeking RBF-FD weights. Instead, a different linear system of equations needs to be solved. Using the same demonstration process presented before, it is proven that the new local linear system has the same left-hand matrix as in eq (2.19), but a different right-hand side (RHS) vector:

$$\begin{pmatrix} & & & 1 & x_1 & y_1 & z_1 \\ & \mathbf{R} & & \vdots & \vdots & \vdots & \vdots \\ & & & 1 & x_n & y_n & z_n \\ 1 & \cdots & 1 & & & & \\ x_1 & \cdots & x_n & & \mathbf{0} & & \\ y_1 & \cdots & y_n & & & & \\ z_1 & \cdots & z_n & & & & \end{pmatrix} \begin{pmatrix} w_1 \\ \vdots \\ w_n \\ w_{n+1} \\ w_{n+2} \\ w_{n+3} \\ w_{n+4} \end{pmatrix} = \begin{pmatrix} DR(||\mathbf{r}-\mathbf{r}_1||)|_{\mathbf{r}=\mathbf{r}_i} \\ \vdots \\ DR(||\mathbf{r}-\mathbf{r}_n||)|_{\mathbf{r}=\mathbf{r}_i} \\ D\ 1|_{\mathbf{r}=\mathbf{r}_i} \\ D\ x|_{\mathbf{r}=\mathbf{r}_i} \\ D\ y|_{\mathbf{r}=\mathbf{r}_i} \\ D\ z|_{\mathbf{r}=\mathbf{r}_i} \end{pmatrix}, \tag{2.21}$$

where D is the same operator as in eq (2.6), and w_i $(i = 1, \ldots, n, n+4)$ are the solution. Note that only w_i $(i = 1, \ldots, n)$ are used as the RBF-FD weights.

In general, the dimension of the linear system in eq (2.21) will be $n + m$, with n as the number of meshfree points in a subdomain (i.e., number of RBF interpolation basis functions) and m as the number of terms of enriched polynomials. In this thesis, the local linear system of equations in eq (2.21) is by default solved by the LU decomposition algorithm implemented in open source package LAPACK (version 3.8.0) (Anderson et al., 1999), unless otherwise stated.

2.4.2 Infinitely smooth and finite-smoothness RBFs

In the scheme of RBF-based meshfree numerical methods (including RBF-FD), many different RBFs can be chosen to form the meshfree interpolation in eq (2.18) with a nonsingular coefficient matrix. These RBFs are often grouped as two categories in terms of smoothness (Fasshauer, 2007): infinitely smooth and finite-smoothness RBFs (the finite-smoothness RBFs are sometimes called piecewise smooth RBFs, see Fornberg et al., 2002). As the group names indicate, infinitely smooth RBFs are differentiable for any order of derivatives, whereas finite-smoothness RBFs are C^k functions with $0 \leqslant k \neq \infty$ as an integer. Some typical RBFs from these two groups are listed in Table 2.1. Since Kansa's pioneering work (see Section 2.4), RBF-based PDE-solving methods using infinitely smooth RBFs have been frequently studied and applied for meshfree PDE-solving problems in areas that include computational fluid dynamics and solid mechanics (e.g., Wang & Liu, 2002a; Shu et al., 2003; Chandhini & Sanyasiraju, 2007), mantle convection modelling of the Earth (e.g., Wright et al., 2010), and seismic wavefield simulation (e.g., Takekawa et al., 2015; Li et al., 2017).

The success and popularity of using infinitely smooth RBFs in PDE-solving methods is largely because of their high-order convergence rate under refinement. However, infinitely smooth RBFs often contain a shape parameter (see Table 2.1) that controls the flatness of the RBF. The shape parameter has a significant effect on the numerical accuracy of RBF-based interpolation and therefore that of PDE-solving algorithms, and needs to be chosen with care. In fact, in the case of infinitely smooth RBFs, it is now understood that flatter RBFs (e.g., smaller c in Gaussian RBFs $e^{-(cr)^2}$) result in a better interpolation accuracy in theory but at the same time a more ill-

conditioned local linear system of equations in the function approximation, although the approximation itself is well-posed (Schaback, 1995; Fasshauer & Zhang, 2007; Fornberg & Piret, 2007). If the ill-conditioned linear system is solved directly using algorithms with finite precision arithmetic, a numerical solution with low accuracy will be obtained. This is due to numerical evaluation errors. On the other hand, using sharper RBFs leads to a better conditioned linear system which can be solved with less numerical errors, but the approximation accuracy is predicted theoretically to be lower. This phenomenon is sometimes referred to as 'uncertainty principle' in the literature (Schaback, 1995). It is this dilemma that causes a trade-off in selecting a good enough shape parameter of infinitely smooth RBFs for solving a general PDE, as explained in the following.

To use infinitely smooth RBFs in deriving approximation weights of differential equations (e.g., RBF-FD weights), two categories of methods can be used to ensure the interpolation accuracy, or equivalently, the quality of approximation weights of PDEs. The first type of methods aims to find an 'optimal' or trade-off shape parameter that limits the deterioration of the numerical solution of local linear system of interpolation to an acceptable level (Rippa, 1999; Wang & Liu, 2002b; Fasshauer & Zhang, 2007; Davydov & Oanh, 2011b; Uddin, 2014). Once such a value of shape parameter is determined, the local linear systems can then be solved directly (e.g., by LU decomposition) without any modification or preconditioning (methods of this group are thus abbreviated as RBF-direct methods in the following). The second type of method focuses on finding a new and more stable basis of vectors[4] that spans the same solution space as the original RBF-based basis does for the coefficient matrix

[4]Here, the basis of vectors of a matrix is referred to as the column basis vectors of a matrix.

of interpolation, such that the resultant new linear system can be stably solved with accuracy for the whole range of shape parameter values (Fornberg & Wright, 2004; Fornberg & Piret, 2007; Fornberg et al., 2011; Fasshauer & McCourt, 2012; Larsson et al., 2013; Fornberg et al., 2013). The change of basis vectors of a coefficient matrix can be considered as a preconditioning technique (e.g., Larsson et al., 2013; similarly, methods of this group are abbreviated as basis-changing methods in the following).

Infinitely smooth RBFs have the advantage of higher order of convergence than the finite-smoothness RBFs in meshfree function approximation. However, in the context of solving PDEs such as forward modelling of geophysical data, the use of infinitely smooth RBFs is considered to be disadvantageous in this thesis study. This can be justified from two aspects. First, when using localized meshfree PDE-solving methods, for example RBF-FD in this thesis, the convergence advantage of infinitely smooth RBFs is somewhat diminished. Convergence rate of solution when solving PDEs is no longer predominantly affected by the RBFs; it will be equally or even overwhelmingly affected by the subdomain size (i.e., number of points in a meshfree subdomain, Bayona et al., 2010) and possibly enriched polynomials (Flyer et al., 2016a). Second, significant computational cost is necessary to determine a sufficiently good shape parameter, particularly for large-scale Earth models with a considerable amount of degrees of freedom as in the case of geophysical data modelling. This can be explained with both RBF-direct and basis-changing methods mentioned above in determining the shape parameter of RBFs. In the former methods (i.e., RBF-direct methods), since an optimal shape parameter is typically affected by many factors including spatial arrangement of local points, type of RBFs, size of subdomain and the unknown function itself (Rippa, 1999), search algorithms for determining an optimal

parameter become potentially problem-specific. Also, an intelligent search algorithm considering these factors is needed to find the optimal parameter, requiring solving the local interpolation linear system many times for each point. In the latter methods, the basis-changing process provides stable numerical solutions even for those shape parameters of flat RBFs, however, the developed algorithms so far entail complicated decomposition and orthogonalization of the original interpolation matrix, and typically require 10 to 20 times more computational time than a standard evaluation time using direct LU decomposition (Larsson et al., 2013).

Finite-smoothness RBFs (e.g., polyharmonic splines, or PHSs, in Table 2.1), on the other hand, are free of such a shape parameter and thus completely avoid the necessity of selecting a good shape parameter for solving PDEs. Another benefit of using PHS RBFs is that although the local linear system of equations arising from RBF-based interpolation can still become very ill-conditioned when the number of points in subdomains is not small (e.g., $n > 50$ in 3-D), accurate solution of the linear system can be readily obtained by a direct LU decomposition if scaling the subdomain by a distance h_s first, which is essentially a preconditioning technique, for very large condition number situations (Iske, 2003). This is different from the ill-conditioning issue of using flat infinitely smooth RBFs as just described, which may require the computation of LU decomposition many times in deriving differential weights in a subdomain. This simple scaling preconditioning, made possible due to the invariant property under scaling of PHS RBFs (Iske, 2003), is however not applicable to infinitely smooth RBFs. As such, PHS RBFs are preferred in the applications of RBF-FD in this thesis study. Recent studies (Flyer et al., 2016a,b; Bayona et al., 2017) show that the meshfree interpolation using PHS RBFs, if augmented

with proper polynomials, can overcome saturation errors under local refinements of points, a difficulty frequently encountered when using infinitely smooth RBFs alone (e.g., Gaussian RBFs, Fornberg et al., 2013). Another finding in these studies is that when using PHS RBFs in the RBF-FD scheme, the rate of h convergence (i.e., convergence under refinement) is essentially dependent on the degree of enriched polynomials, rather on the degree of PHS RBFs. This finding, although being a numerical observation, provides a new insight in applying RBF-FD for solving PDEs with good accuracy.

2.5 Application of meshfree methods in problems with discontinuity

Regardless of the type of basis functions (RBF or non-RBF), a standard meshfree function approximation results in a highly smooth interpolant within each meshfree subdomain. Since meshfree subdomains typically overlap, this gives rise to a globally smooth solution when solving PDEs (Nguyen et al., 2008). The global smoothness of a numerical solution is traditionally an advantage of meshfree PDE-solving methods when considering their early applications as mentioned before (e.g., computational fluid dynamics and astrophysics). For the same reason, the smoothness nature of standard meshfree techniques becomes a drawback when solving problems involving discontinuities in the function of interest or in its first derivatives (Krongauz & Belytschko, 1998). The application of meshfree methods in synthesizing geophysical EM data for a geometrically arbitrary 3-D conductivity model falls within the case that

involves possible discontinuities.

Being a potential difficulty, the reproduction of possible discontinuities in a meshfree solution has been addressed since as early as 1990s (Belytschko et al., 1996) and is still an active research topic (e.g., Jalušić et al., 2017). Over the years, two major ideas for overcoming this difficulty have been developed. The first is to modify to some extent the standard meshfree function approximation in order to reproduce desirable discontinuities within meshfree subdomains. The second is to take advantage of the geometric information of the discontinuities and then construct a normal meshfree approximation that satisfies specific conditions. Since the discontinuity behaviour of the normal electric field in geophysical EM data over conductivity jumps is well understood, this discontinuity issue needs to be addressed in order to apply any meshfree technique to synthesize EM responses. The proposed meshfree method in this thesis originates from the second idea, but differs from existing techniques. The details of available techniques along with the newly proposed techniques in this thesis are presented in Chapters 4 and 5.

Chapter 3

Simulation of geophysical gravity data using RBF-FD

3.1 Introduction

Geophysical gravity data interpretations resolve density information in the subsurface. The interpretations are routinely carried out by means of 3-D inversion nowadays, in which 3-D forward modellings are necessary (Li & Oldenburg, 1998; Moorkamp et al., 2011). In the forward problem, the task is to calculate gravity fields (mostly vertical gravity) and gravity gradients at specific measurement locations due to a density distribution of the subsurface. Two categories of methods are capable of modelling the gravity responses of a general inhomogeneous density model: summation-based and PDE-solving techniques. In the summation-based approaches, gravity responses are obtained by taking volume integrals based on Newton's law of universal gravitation. In the PDE-solving category, a boundary value problem using Poisson's equation of

gravitational potential is solved.

Summation-based approaches are often called analytical methods since the evaluation of integrals can be carried out rather accurately, sometimes even without using numerical quadrature. Early studies in terms of 3-D gravity data modelling mostly focused on this type of technique, with a number of developed mathematical formulae for evaluating integrals. A particular interest in the early time was to use rectilinear meshes, which are the simplest 3-D meshes, for discretizations (Nagy, 1966; Banerjee & Das Gupta, 1977; Last & Kubik, 1983; Guillen & Menichetti, 1984; Bear et al., 1995; Li & Oldenburg, 1998). In order to account for complex density models, analytical formulae of computing gravity or gravitational potential have also been developed, mainly based on the gravity responses due to a particular type of polyhedral element other than prisms with homogeneous densities (Paul, 1974; Barnett, 1976; Okabe, 1979; Waldvogel, 1979; Pohánka, 1988; Petrović, 1996; Holstein, 2002; Tsoulis, 2012; D'Urso, 2014a). More recently, there have been attempts in developing such analytical formulae for polyhedral elements within which the density is not constant, but changes continuously following the pattern of some polynomial functions (Pohánka, 1998; Hansen, 1999; Holstein, 2003; Zhou, 2009; D'Urso, 2014b; Ren et al., 2017a).

One obvious reason to use summation-based approaches in the context of forward modelling and inversion of gravity data is that their algorithm implementations are relatively easy and straightforward. Also, very accurate numerical results are often offered if the above-mentioned analytical formulae are available for a given model discretization. In terms of efficiency, the computation complexity for N measurements with a discretization of M degrees of freedom (the number of cells) is $O(N \times M)$. It is known that the efficiency achieved using summation-based approaches deteriorates

as either N or M increases, which is a major drawback when dealing with large-scale models with possible hundreds of thousands of measurements (e.g., airborne gravity surveys). Another disadvantage is that, when adopting such approaches as the forward modelling engine in an inversion using gradient-based optimization, for example, the popular minimum-structure inversion using a Gaussian-Newton method, the resultant sensitivity matrix is full and dense and has the dimension of N by M. This full and dense sensitivity matrix would require a large amount of memory storage for inversions for large-scale models, or for moderate-scale models but with high resolution. Aside from the memory storage issue, the computational complexity also increases due to a large full and dense sensitivity matrix, for which the detailed arguments are presented by, for example, Farquharson & Mosher (2009) and May & Knepley (2011). For practical 3-D forward modelling and inversion of gravity data, additional remedies that alleviate the storage of and/or the computational complexity related to the sensitivity matrix are often required (e.g., Li & Oldenburg, 1998, 2003; Chasseriau & Chouteau, 2003; Pilkington, 2009; Davis & Li, 2011; May & Knepley, 2011; Ren et al., 2017b).

In contrast to summation-based approaches, PDE-solving techniques can synthesize all N data measurements at once, including gravity fields and gravity gradients, with a trivial cost once a solution to the PDE is obtained. In other words, the computational complexity is $O(M)$. This is because gravity signals at the desired measurement locations can be simultaneously obtained by solving once a linear system of equations in PDE-solving approaches. The linear system arising from traditional PDE-solving techniques (e.g., grid-based FD, FE and FV methods) has a highly sparse coefficient matrix. When this coefficient matrix is implicitly formed

and stored in memory in a matrix-free way, the aforementioned sensitivity matrix even needs not be explicitly stored. As a result, the computation involving the sensitivity matrix, which is still full and dense, can be very efficiently carried out in the case of gradient-based iterative inversions (Farquharson & Mosher, 2009). Although the solution accuracy of a PDE-solving approach is affected by model discretization, the above-mentioned advantages of PDE-solving approaches make them an attractive option for practical gravity data inversions, particularly for those involving large-scale complex models.

Forward modellings and inversions of 3-D gravity data using grid-based FD, FE and FV methods have all been reported in the literature. Farquharson & Mosher (2009) and Farquharson (2008) used a FD method together with rectilinear meshes to forward model and invert, respectively, gravity data, and demonstrated the above computational efficiency of PDE-solving approaches with numerical examples. Zhang et al. (2004) used an FE implementation for the forward calculation of gravity fields in their genetic search-based inversion algorithm. Cai & Wang (2005) also used a FE method for 3-D gravity data modelling and compared its computational efficiency with that of summation-based techniques. They concluded that using the FE techniques can be significantly more efficient than using summation-based counterparts in modelling over 3-D complex geological regions if the data amount N is much greater than a few hundreds. May & Knepley (2011) reported similar efficiency results by using an FE implementation and summation-based techniques. Their comparison study suggests that the FE approach in conjunction with an approximated boundary condition for solving Poisson's equation (Cai & Wang, 2005) can be more useful in practice than an accelerated version of summation-based techniques, namely, their

fast multipole method. More recently, PDE-solving techniques have been used for dealing with complicated geometries of density models (Jahandari & Farquharson, 2013) and for modelling efficiency in working with large-scale density models (Haber et al., 2014; Gross et al., 2015).

In this chapter, the chosen meshfree method, RBF-FD, is proposed as an alternative PDE-solving approach to forward model 3-D gravity signals. Implementation details of the meshfree methods, for example how to determine RBF-FD stencil sizes, are presented here. Despite being a simpler problem compared to EM field simulations, the gravity data modelling is a good example of investigating the fundamentals of the meshfree method, which will be the basis for the later applications in modelling MT and CSEM data.

3.2 Poisson's equation for gravitational potential

In this thesis, Poisson's equation for the gravitational potential due to a density distribution is numerically solved. A general expression for the equation is (Kellogg, 1967; Blakely, 1996)

$$\nabla^2\phi(\mathbf{r}) = -4\pi\gamma\rho(\mathbf{r}); \quad \text{for} \quad \mathbf{r} \in \Omega \subset \mathbb{R}^3, \tag{3.1}$$

where $\phi(\mathbf{r})$ is the potential function, γ is the gravitational constant, $\rho(\mathbf{r})$ denotes the density function or distribution, Ω represents the problem domain, and ∇^2 is the Laplacian operator. Eq (3.1) holds both in and outside the density source region Ω_s ($\Omega_s \subset \Omega$, $\rho \neq 0$ only in Ω_s). In practical geophysical applications, gravity fields

and gravity gradients are collected as the measurements. The gravity field vector, or acceleration vector, $\mathbf{g}$ is obtained by taking the gradient of ϕ

$$\mathbf{g} = -\nabla\phi. \tag{3.2}$$

The gravity gradients, which are the 9 components of the 3 by 3 gradient tensor, $\mathbf{U}$, are numerically obtained by taking the gradient of $\mathbf{g}$

$$\mathbf{U} = \nabla\mathbf{g} = -\nabla\nabla\phi = \begin{pmatrix} U_{xx} & U_{xy} & U_{xz} \\ U_{yx} & U_{yy} & U_{yz} \\ U_{zx} & U_{zy} & U_{zz} \end{pmatrix}. \tag{3.3}$$

For the gravity problem, $\mathbf{U}$ has symmetric components; that is, $U_{xy} = U_{yx}$, $U_{zy} = U_{yz}$ and $U_{zx} = U_{xz}$ always hold. Also, according to eq (3.1), the three diagonal components of $\mathbf{U}$ satisfy $U_{xx} + U_{yy} + U_{zz} = 0$ outside of the source regions. As a result, only 5 of the components of the gradient tensor are independent.

In order to devise a numerical solution to eq (3.1), the problem domain Ω is truncated to be a rectangular box for all numerical examples here. On its boundaries, the Dirichlet boundary condition

$$\phi(\mathbf{r}) = 0, \quad \mathbf{r} \in \partial\Omega, \tag{3.4}$$

is used to ensure a unique solution. One can use far-field approximated potential values to replace the boundary condition in eq (3.4) so that the problem domain, which is also the computational domain, is further reduced in size (Cai & Wang,

2005). However, the homogeneous Dirichlet boundary condition in eq (3.4) is simple to implement and more general for density models with arbitrary geometries. Further, it can be shown that a local refinement with unstructured meshfree points allows for an efficient discretization without a significant increase in the number of degrees of freedom.

Eq (3.1) is discretized over the meshfree points per subdomain using the approximation discussed in Section 2.4.1. For the source term, the point-based density value of $\rho(r)$ is used for homogeneous regions, and an arithmetic average of the density is used for any meshfree points residing on the interfaces in the density model. The gravitational potential is smooth even across the boundaries of the density source so that there is no discontinuity issues here.

3.3 Convergence analysis of RBF-FD

3.3.1 The case of global refinement

A synthetic density model with a single prismatic density anomaly was designed in order to understand the convergence behaviour of RBF-FD under a global refinement of discretization. The prism, with the density $\rho = 2000$ kg m^{-3}, is embedded at the centre of the computational domain and is surrounded by a void region with density $\rho = 0$ kg m^{-3}. The model set-up is the same as that in Farquharson & Mosher (2009) and May & Knepley (2011). The rectangular computational domain size is truncated to be $\Omega = \{(x, y, z) | -500 \text{ m} \leqslant x, y, z \leqslant 500 \text{ m}\}$. The prism source has the dimension of $100 \times 100 \times 100$ m. The meshfree points are distributed in a way

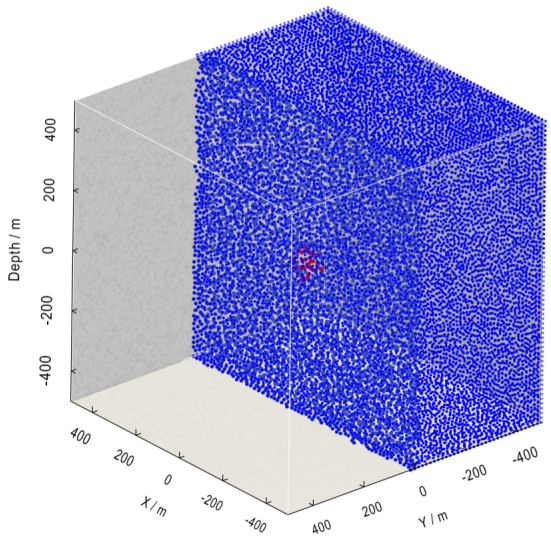

Figure 3.1. Quasi-uniform points shown on the surface and at the cross-section $y = 0$ of the prismatic density model for convergence analysis. The red points in the middle of the cross section are inside the cubic density source.

such that they are quasi-uniform and unstructured (Fig 3.1), that is, an unstructured set of points with uniform averaged internodal distances[1]. Unstructured meshfree point discretizations are favoured for meshfree methods in this thesis study because they have the most powerful capability of representing irregular geometries which are common in realistic Earth models. In the case of quasi-uniform discretizations, the number of points grows as the order of N_h^3 with N_h the estimated number of points in each Cartesian direction.

The truncated domain is not sufficiently large to use the boundary condition in eq (3.4) without significant numerical errors. Therefore, an analytical solution of potentials on the boundaries based on a summation-based integral technique (Waldvogel, 1976) was used as the boundary values. The small truncated domain is not

[1]Such a quasi-uniform point discretization normally has almost the same amount of degrees of freedom as that of a uniform rectilinear mesh.

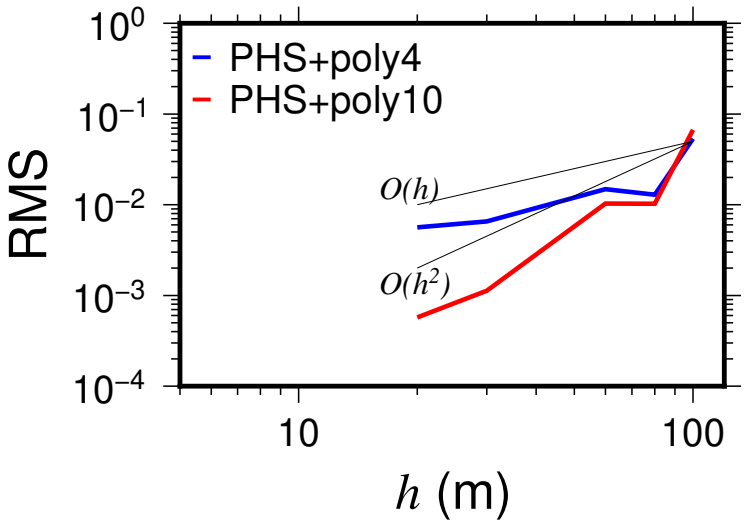

Figure 3.2. RMS errors of computed gravity potentials versus the averaged internodal distance h. Results were calculated by PHS RBF-FD with enriched linear polynomials (labelled as 'PHS+poly4') and quadratic polynomials (labelled as 'PHS+poly10'). The two black solid lines indicate theoretical linear $O(h)$ and quadratic $O(h^2)$ convergence rates in the log-log plot.

suitable for practical applications, but was chosen in the test such that the number of degrees of freedom will not become too large under global refinements. In order to assess the convergence rate of different RBF-FD schemes, the root-mean-square (RMS) error in the following is computed

$$RMS = \sqrt{\frac{1}{N}\sum_{i=1}^{N}\left(\frac{\phi_i^{numer} - \phi_i^{exact}}{\phi_i^{exact}}\right)^2}, \tag{3.5}$$

where N is the total number of points but excluding those on the boundaries of the computational domain, ϕ_i^{numer} are the potentials computed by RBF-FD and ϕ_i^{exact} are the analytical solutions.

The PHS RBF used is r^5 in this chapter as it is twice differentiable and thus is able to approximate the Laplacian operator (see Appendix A). The stencil size was

fixed as $n = 30$. The h convergence results are shown in Fig 3.2. It is evident that for both situations of polynomial enrichment (linear and quadratic), the numerical solution using the PHS RBF-FD scheme converges to the true solution. In addition, it is observed that the PHS RBF-FD enriched with linear polynomials in meshfree interpolation has the convergence rate approximately as $O(h)$, and the counterpart with quadratic polynomials has the convergence rate approximately as $O(h^2)$ when reducing the internodal distance. These observations are consistent with those of Bayona et al. (2017) which shows that it is numerically observed that the h convergence order is dependent on the highest order of the enriched polynomials, rather than the order of PHS RBFs. It is worth noting that in both situations of enrichment, the number of RBF-FD weights for each subdomain is the same; therefore, the additional computational costs as a result of using higher order polynomials occur in the process of finding RBF-FD weights, instead of in solving the global linear system of equations which is often the most computationally expensive part for a numerical solution.

3.3.2 The case of local refinement

Although uniform (i.e., equidistant points) or quasi-uniform 3-D point discretizations are relatively easy to generate, non-uniform and unstructured meshfree point discretizations are more practical. The non-uniform feature of a discretization is fulfilled by using local refinements. Several studies using meshfree methods have been reported for solving geophysical modelling for EM data (Wittke & Tezkan, 2014) and for seismic wave field (Jia & Hu, 2006; Martin et al., 2015; Takekawa & Mikada, 2016; Li et al., 2017). However, they all use uniform, or quasi-uniform, or the combination

of these two types of point discretizations and are focused on 2-D problems. A major drawback of using these discretizations is that the number of degrees of freedom grows as N_h^3 when solving 3-D problems. In this case, unstructured discretizations with local refinements will be more efficient.

To demonstrate the convergence of RBF-FD under local point refinements, the same single-block density model was discretized with non-uniform points. Typically, local refinements are deployed in regions where numerical accuracy is desired or the function involved changes very rapidly. For the density model here, a line with 200 points was designed for the synthetic measurement sites. The line is located at $-200\text{m} \leqslant x \leqslant 200$ m, $y = 0$ m, $z = 100$ m, which is 100 m above the centre of the rectangular block anomaly. The local refinements are focused on the measurement sites and inside the density block. The computational domain was extended to be $\Omega = \{(x, y, z)| - 500 \text{ km} \leqslant x, y, z \leqslant 500 \text{ km}\}$. This is made possible because of the limited degrees of freedom (up to 90,000 for discretization examples here). As a result, the homogeneous Dirichlet boundary condition in eq (3.4) was used for all discretizations with local refinements here. A graphical example of the local refinements is shown in Fig 3.3.

Both gravity potentials and the vertical gravity component ($\mathbf{g}_z$) at the measurement sites were computed under different local refining scales for two cases. In the first case, local refinements were carried out inside the density source. In the second case, the points around the 200 measurement sites were refined with different scales. The refining scales were manually controlled by setting different internodal distances in the discretizations. To examine the local convergence performance, relative errors of the numerically computed potentials and gravity are considered. For the numerical

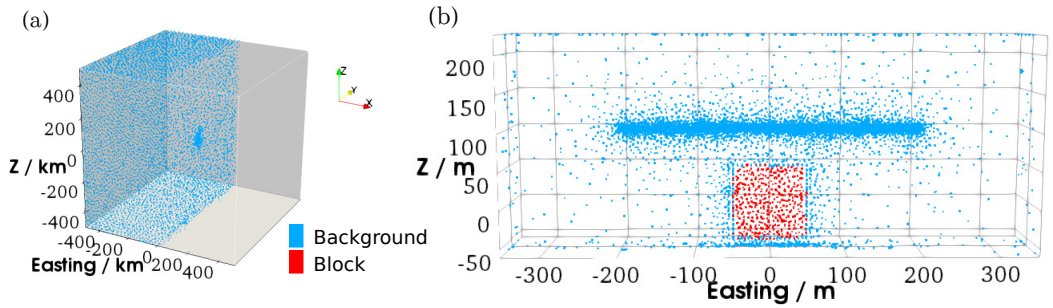

Figure 3.3. Unstructured, non-uniform point discretization displayed in: (a) a perspective view of the points within the easting $-500 \leqslant x \leqslant 0$ km, and (b) an enlarged view of the local point refinements within the blocky density source (red points, internodal distance $h = 10$ m) and at the observation sites at the cross section northing $y = 0$ m (internodal distance $h = 1$ m).

solutions, the PHS RBF-FD with enriched quadratic polynomials was used. In both cases, the RBF-FD stencil size was fixed as $n = 37$ to avoid possible adverse effects on numerical accuracy that result from using an insufficient number of points in RBF-FD subdomains (influence of the stencil size is discussed in the next section). In order to obtain the exact potentials and gravity values, the summation-based methods of Waldvogel (1976) and Li & Chouteau (1998; by the method of eq. 4) were used for calculating the analytical potential and gravity values, respectively.

The relative errors are shown in Fig 3.4. In the first case (panels a and b), the density source was refined with different averaged internodal distances, and the measurement sites were refined with the internodal distance $h = 1$ m. In the second case (panels c and d), the measurement sites were refined with different scales, as indicated in Fig 3.4, and the density source was refined with the internodal distance $h = 10$ m. It is observed that in both cases, the numerical solutions converge to the exact ones under local refinements. Note that the error spikes in the case of measurement refinement when $h = 20$ m (blue dots) shown in panels c and d are due to the lower

point regularity caused by the meshing tool (Si, 2015). The results show that for accurate modelling, the density source, or the physical property distribution, should be appropriately discretized. It is also seen that the smoothness of the numerical solution can be improved by the local refinements. These observations are similar to those of numerical solutions obtained by mesh-based methods such as FE and FV.

A comparison of the computed gravitational potentials and vertical gravities along the designed measurement line using a quasi-uniform discretization and an unstructured point discretization is shown in Fig 3.5. For both discretizations, the PHS RBF-FD was enriched with quadratic polynomials. In the former case, RBF-FD stencil size was $n = 30$ and the average internodal distance $h = 20$ m. The computational domain was $\Omega = \{(x, y, z)| - 500 \text{ m} \leqslant x, y, z \leqslant 500 \text{ m}\}$. While in the latter case, i.e., the non-uniform discretization, $n = 37$ and $\Omega = \{(x, y, z)| - 500 \text{ km} \leqslant x, y, z \leqslant 500 \text{ km}\}$. A local refinement with $h = 9.5$ for the density source and $h = 1$ m at the measurement sites was used. For both types of discretizations, the numerical solutions of ϕ and g_z agree well with corresponding analytical solutions, with the maximum relative errors being less than 2 %. While the quasi-uniform discretization has $367,605$ points in total, the unstructured discretization has only $72,082$ points, which is approximately one fifth of the former. It is noted that in the latter case, a much larger computational domain with practical boundary conditions ($\phi = 0$ at the boundaries) can be used, which has little assumptions on the density source distribution.

The gravity gradient tensor components (U_{xx}, U_{xy}, U_{xz}, U_{yy}, U_{yz}, and U_{zz}) can also be directly computed using the meshfree method. Fig 3.6 shows the computed tensor components using the above non-uniform unstructured point discretization in the meshfree method. For comparison, an analytical solution (Okabe, 1979) is also given.

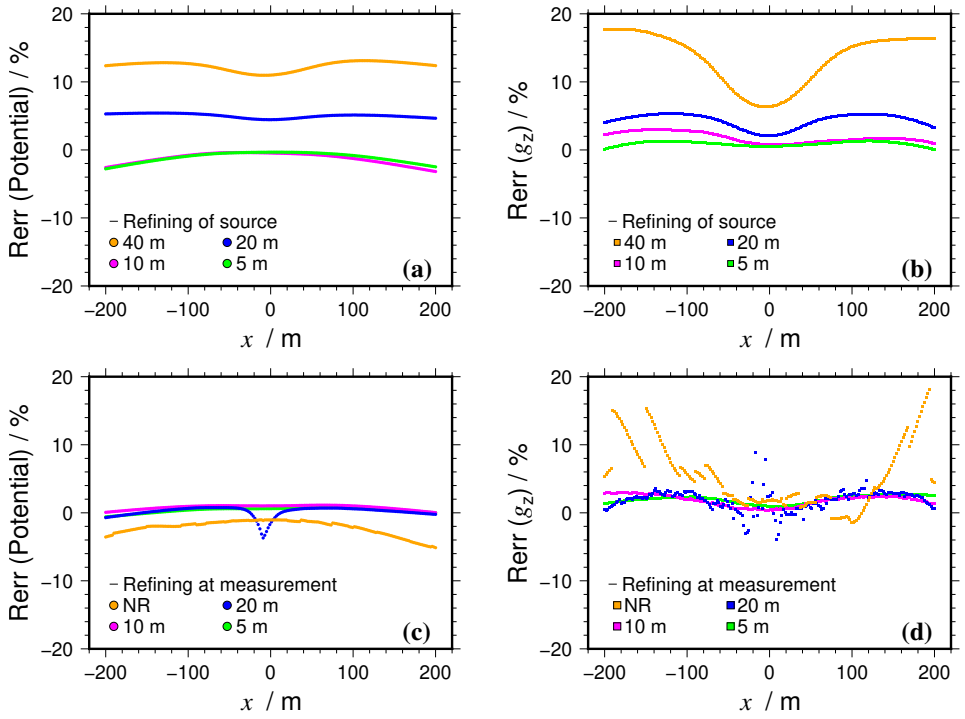

Figure 3.4. Relative errors for the numerical potential and gravity by RBF-FD along the test line in the blocky density model (Fig 3.3). Panels a and b show the errors under different refining scales inside the density source (indicated by the internodal distance $h = 40$, 20, 10 and 5 m) for potentials and gravities (g_z), respectively. In the case of source refinements, a refinement of $h = 1$ m was applied at the measurements. Panels c and d show the corresponding errors under different local refining scales at the measurement sites (indicated by the internodal distance $h = 20$, 10, and 5 m). The situation without local refinement at the measurements is denoted as NR. In the case of measurement refinements, a refinement of $h = 10$ m was applied for the density source block.

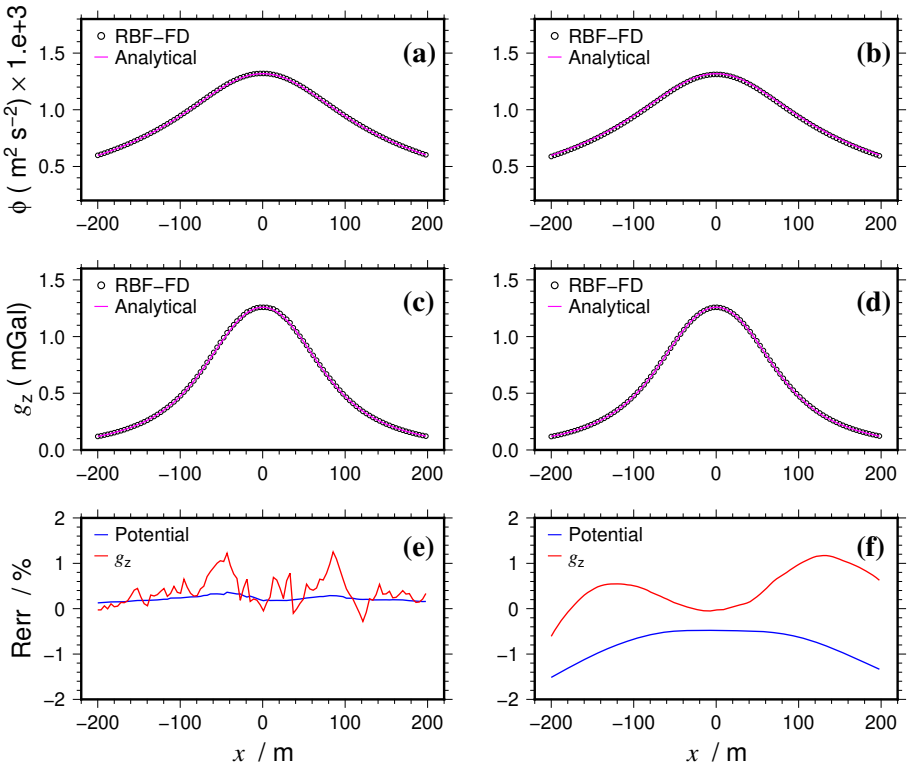

Figure 3.5. Computed potential (ϕ), vertical gravity (g_z), and their relative errors (Rerr) by the PHS RBF-FD using a quasi-uniform point discretization with the averaged inter-nodal distance $h = 20$ m (panels **a**, **c** and **e**), and using a non-uniform, unstructured point discretization (panels **b**, **d** and **f**), which is discussed in the text, for the blocky density model.

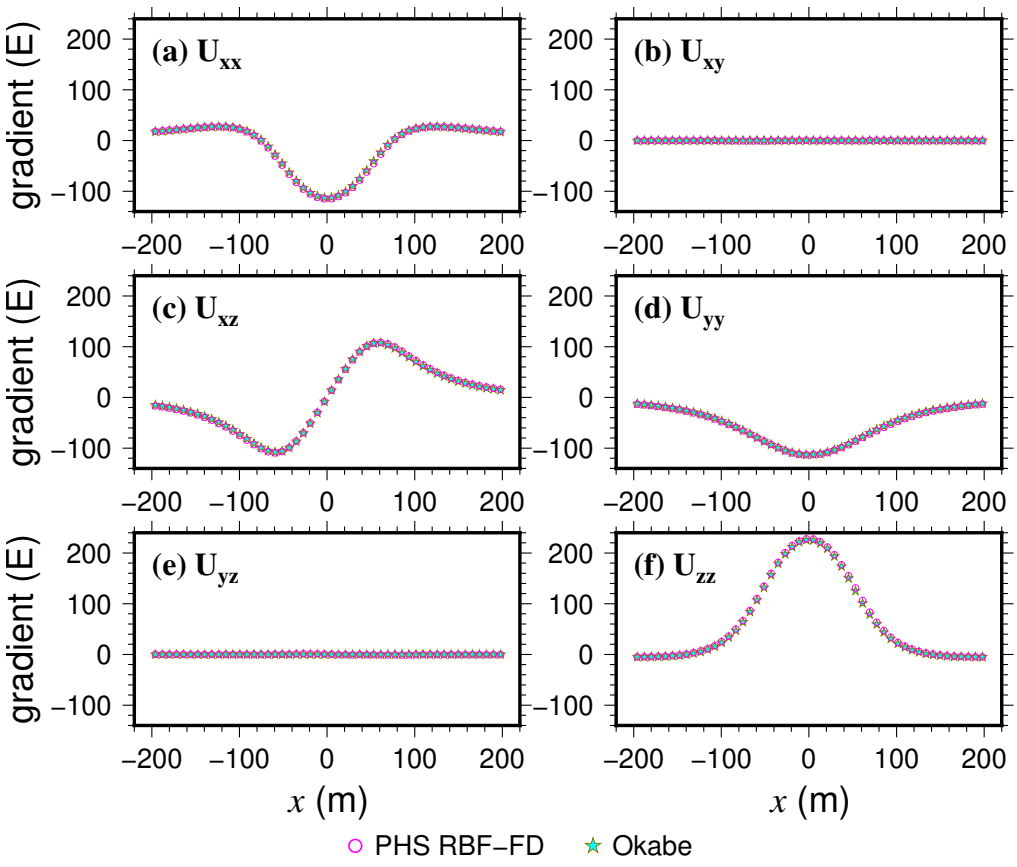

Figure 3.6. Comparison of six components of gravity gradient tensor (U_{xx}, U_{xy}, U_{xz}, U_{yy}, U_{yz}, and U_{zz}) calculated using the PHS RBF-FD method with a non-uniform, unstructured point discretization, and using a summation method (Okabe, 1979) for the blocky density model. The gradient values are shown in Eötvös (E).

The measurement sites are the same as those for Fig 3.4 and Fig 3.5. It is observed that the calculated gradient tensor components also have an excellent agreement with analytical results. Although U_{zz} is often not considered as an independent component, it was numerically computed here (i.e., not using the relation $U_{zz} = -U_{xx} - U_{yy}$).

3.4 Influence of stencil size

In RBF-FD, stencil size refers to the number of points in a subdomain. Although varying stencil sizes for different subdomains can be used, how best to choose the meshfree points in a subdomain remains unclear. There have been attempts in automatically determining an optimal RBF-FD stencil for each subdomain when solving PDEs (e.g., Wright & Fornberg, 2006). However, such selection processes inevitably introduce extra computational costs by solving an optimization problem. In the PHS RBF-FD investigated here, the stencil size is fixed for all meshfree subdomains.

The RBF-FD stencil size affects the matrix dimension of local interpolation linear systems and the sparsity of the formed coefficient matrix of the global linear system of equations, therefore the solving efficiency. It also affects the interpolation accuracy which determines the quality of RBF-FD weights within each subdomain and eventually the accuracy of the numerical solution when solving PDEs. To show the influence of using different stencil sizes on the final numerical solution, the quasi-uniform point discretization with the computational domain size $\Omega = \{(x, y, z) | -500 \text{ m} \leqslant x, y, z \leqslant 500 \text{ m}\}$ was used for demonstration. Again, exact potential values were used as the boundary values. The average internodal distance was $h_s = 45$ m. The total number of points was 37,227. RMS errors of potentials using PHS RBF-FD were calculated

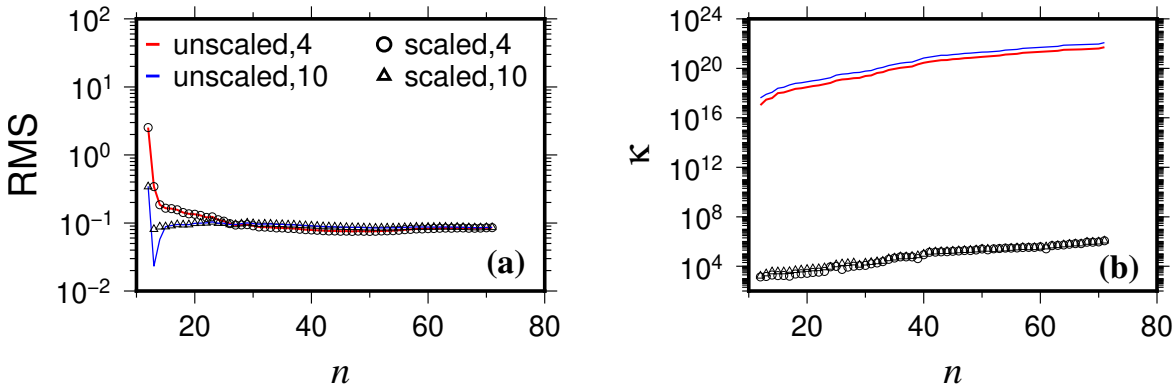

Figure 3.7. Plots of RMS errors (panel **a**) of potentials of PHS RBF-FD, and the condition numbers (κ, panel **b**) of the local interpolation linear system for the point at $(x, y, z) = (50.0, 50.0, 50.0)$ versus various stencil sizes, n. In the labels, '4' indicates that the PHS RBF-FD was enriched with linear polynomials, and '10' indicates that quadratic polynomials were instead used. 'scaled' indicates that the PHS RBF-based interpolation was scaled by the distance h_{sp}, which is the radius of the smallest sphere enclosing all n points in a subdomain. 'unscaled' indicates that the interpolation was not scaled.

for different stencil sizes ranging from $n = 12$ to $n = 70$, as shown in Fig 3.7. In this example, both linear and quadratic polynomial enrichment were tested in the frame of PHS RBF-FD. The PHS RBFs can be scaled simply by the maximum Euclidean distance between the support point and the rest of the points in a subdomain, or the radius of the smallest sphere enclosing all n points in a subdomain, to improve the conditioning of the local interpolation system. Both scaled and unscaled PHS RBF-based meshfree interpolations were tested.

As observed from Fig 3.7(**a**), the solution accuracy of the PHS RBF-FD is affected by the stencil size n. For an accurate numerical solution for 3-D problems, the stencil size should not be too small. It is seen that in this example, the RMS errors for all 4 implementations of the PHS RBF-FD become saturated after increasing n to be about 30. When n is less than 20, the RMS errors are large and the numerical solution

becomes inaccurate. By testing various other examples using both quasi-uniform and non-uniform discretizations, it is found that using $n \geqslant 30$ is mostly sufficient to obtain an accurate numerical solution. It is also observed that when n becomes sufficiently large, increasing n further does not improve the accuracy, but however significantly increases the computational cost by reducing the sparsity of the matrix of the global linear system of equations. This suggests that in the PHS RBF-FD, the benefit of using many more points in subdomains is very limited.

The changes of conditioning of the local interpolation linear system for an example subdomain with its support point as $(x, y, z) = (50.0, 50.0, 50.0)$ are also plotted in Fig 3.7(**b**). It shows that the conditioning can be improved significantly by scaling the interpolation problem. Although the RMS errors in this example for the unscaled and scaled situations are almost indistinguishable, the use of scaled PHS RBF-based interpolation can prevent possible inaccurate evaluations of the PHS RBF-FD weights.

3.5 A comparison between RBF-FD and scalar FE methods

In this section, a comparison of performances between the PHS RBF-FD and scalar FE methods for modelling gravity data over an irregular density model is presented. The density model was built up from part of the model of the Bay du Nord reservoir which is located at the Flemish Pass Basin offshore eastern Canada (Dunham et al., 2018). In the density model, two non-zero density blocks are embedded in a background region that has $\rho = 0$ kg m^{-3}. The density value of the background medium

here is not realistic. It is used merely to generate a sharp change in the simulated gravities at locations of interest. The first block is a Cretaceous sedimentary layer with an average thickness of 300 m and density value $\rho = 2200$ kg m^{-3}. The second block is a reservoir unit that is approximately 100 m thick and is overlain by the sedimentary layer. The reservoir block is assigned the density value $\rho = 2600$ kg m^{-3}. The gap distance between the two blocks is about 100 m for the northern parts. At the southern end, the two blocks gradually attach and join together, and the attachment forms a wedge-like sharp angle, as shown in Fig 3.8 and Fig 3.9. To evaluate the numerical solutions of the vertical gravity field, g_z, using PHS RBF-FD and scalar FE methods, two vertical lines representing measurement sites were designed. The two lines are within the cross section in the y-z plane of the coordinate system with $x = 0$ m (easting). The y (northing) coordinates of the two lines are $y = -3.5$ km (line-1, or L1) and $y = -1.0$ km (line-2, or L2), respectively. The range of the vertical coordinates of the two lines is from $z = -2.5$ km to $z = -4.0$ km.

For both RBF-FD and FE methods, unstructured model discretizations were employed here to represent the irregular geometries, especially those near the attachment of the two density blocks. For the FE method, an unstructured tetrahedral mesh is used. For the PHS RBF-FD, the points generated as the vertices of the tetrahedral elements in the FE mesh are used as the meshfree discretization. The same set of points is used for both methods in this example so that the numerical performances from using the two methods can be compared with minimum discrepancies resulted from model discretizations. In this case, the linear systems from the PHS RBF-FD and scalar FE methods have exactly the same dimension and number of degrees of freedom. The computational domain was set to be $\Omega = \{(x, y, z)| - 50 \text{ km} \leqslant x, y, z \leqslant 50 \text{ km}\}$. The

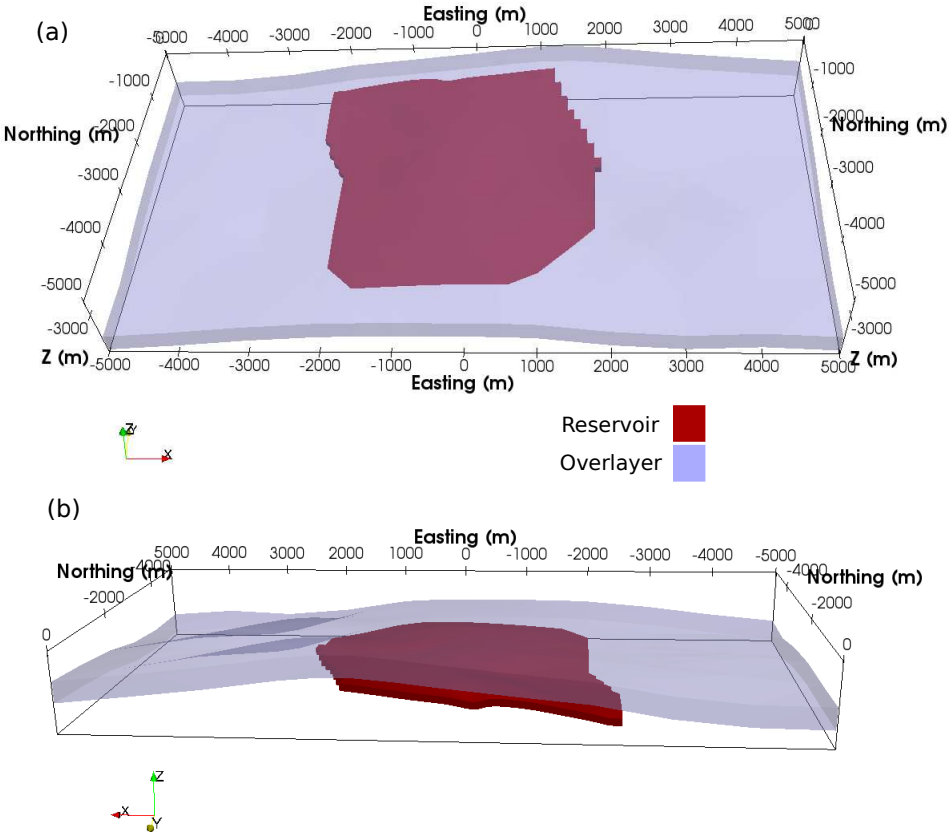

Figure 3.8. Perspective 3-D views of the Bay du Nord density model. The easting is along the x direction, and the northing is along the y direction. The top panel (a) shows the reservoir unit overlain by the sedimentary unit. The view is looking from south to north. The bottom panel (b) is a side view from north to south. A 2-D cross section at $x = 0$ (easting) that cuts through the two blocks is given in Fig 3.9.

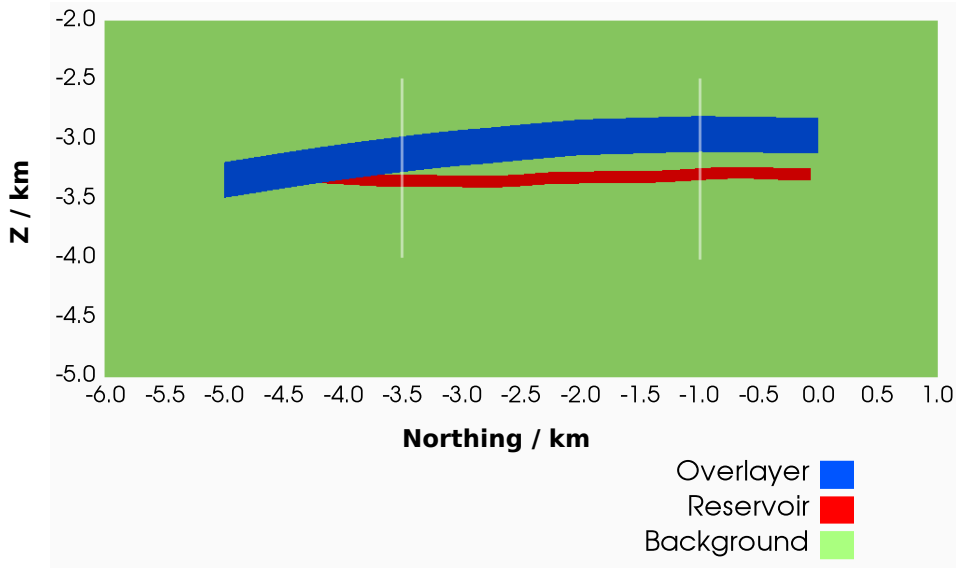

Figure 3.9. Vertical cross section of the Bay du Nord model at $x = 0$ (easting, looking from the positive x direction). The northing direction is along the y axis. Two vertical white lines mark the positions of two measurement lines at $y = -3.5$ km (L1) and $y = -1.0$ km (L2), respectively.

Dirichlet boundary condition for Poisson's equation in eq (3.4) was used. To ensure the accuracy of numerical solutions, local refinements at the measurement sites (200 sites for each line) and within the density blocks were carried out unless otherwise indicated. A comparison of the meshed and meshfree point discretizations is given in Fig 3.10.

The FE results for g_z at the measurement sites were computed by using linear basis functions in the FE elemental analysis. Implementation of the linear FE is the same as that described in Jahandari & Farquharson (2013) for example. For the PHS RBF-FD results, the stencil size was fixed as $n = 30$ and quadratic polynomials were used in meshfree interpolations. To show the accuracies of both FE and RBF-FD methods, an analytical solution was also obtained using the summation-based method in Okabe (1979). The analytical solution for g_z was obtained by summing up the calculations

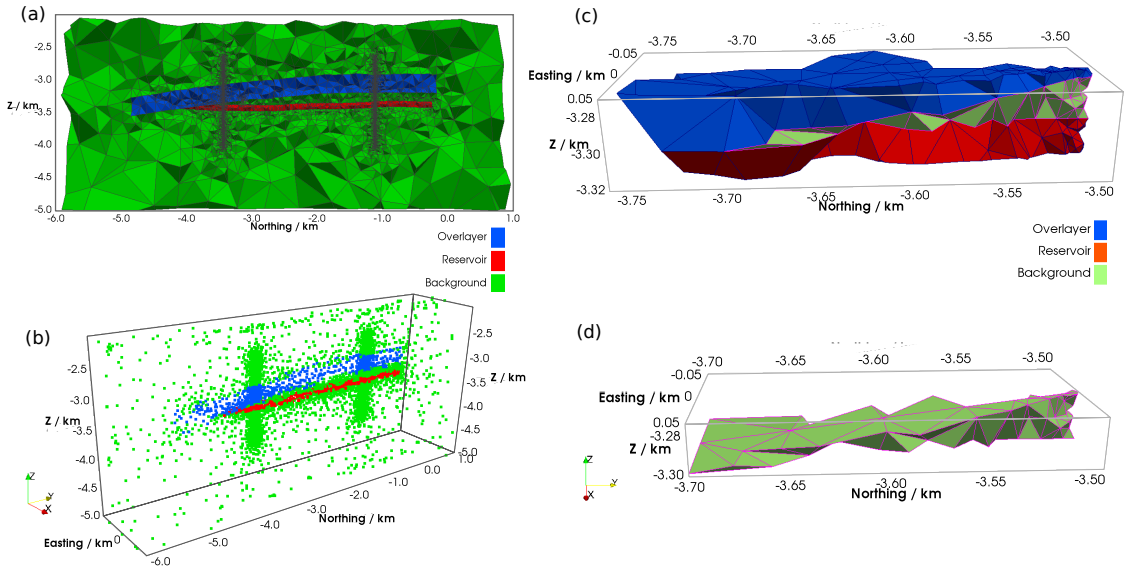

Figure 3.10. Unstructured mesh (panel a) and meshfree points (panel b) for the section shown in Fig 3.9. Note that the mesh is located on the 3-D crinkled surface made at easting $x = 0$ m, and the points in the panel (b) are the 3-D points within the rectangular domain: $\Omega_p = \{(x, y, z) | -0.75 < x < 0.75 \text{ km}, -6.0 < y < 1.0 \text{ km}, -5.0 < z < -2.0 \text{ km}\}$. Panel (c) shows an enlarged 3-D view of the mesh around the wedge-like attachment that is shown in the panel (a). Panel (d) shows the same enlarged view as in panel (c) but only with the tetrahedral elements in the background region. In the panel (d), the tetrahedra shown at the southern end become increasingly thin wedge- or sliver-like elements.

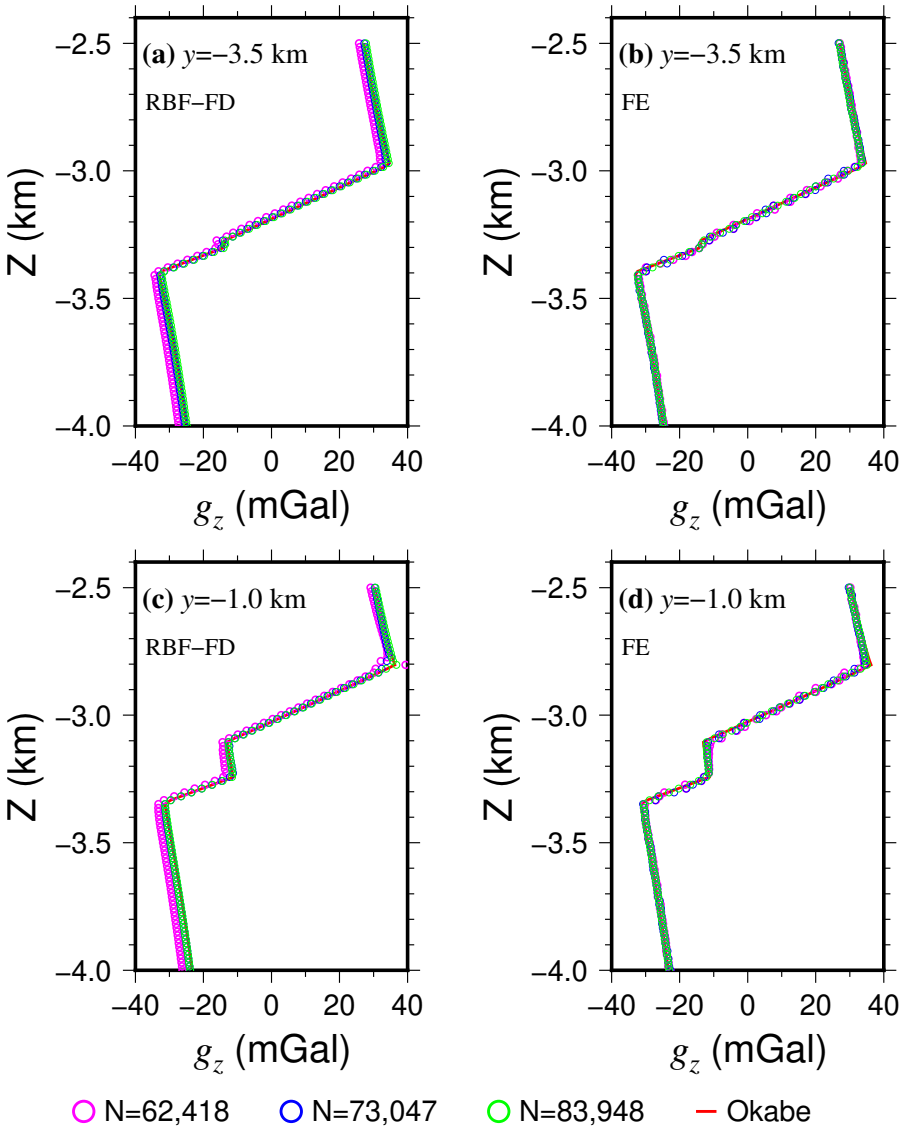

Figure 3.11. Plots of computed g_z along the two vertical lines of the Bay du Nord model, L1 ($y = -3.5$ km) and L2 ($y = -1.0$ km), for three different model discretizations using PHS RBF-FD (panels **a** and **c**) and scalar FE (panels **b** and **d**) methods. Analytical solutions are denoted by 'Okabe'. The three model discretizations are distinguished by the total number of points, N.

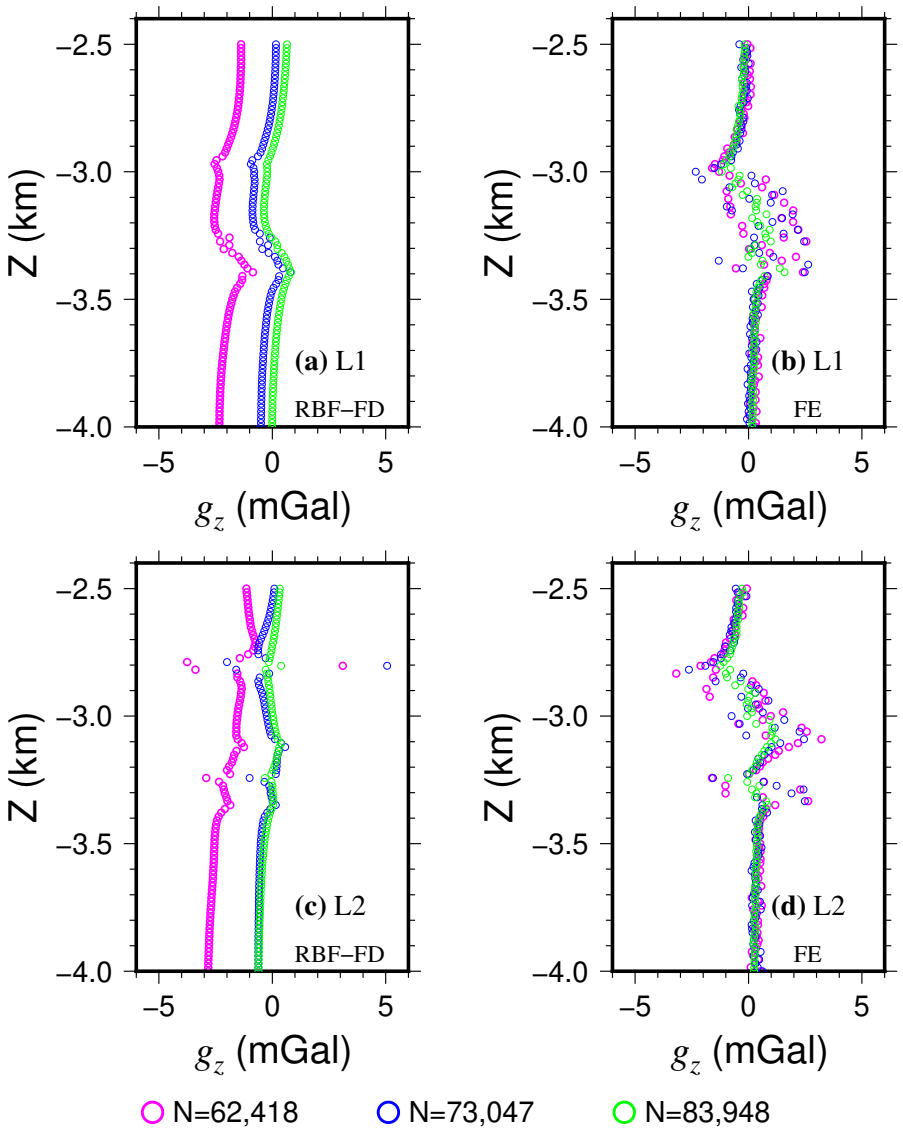

Figure 3.12. Plots of the differences between various numerical solutions and analytical solution of g_z for the Bay du Nord model. The numerical solutions, as shown in Fig 3.11, were computed along the two vertical lines, L1 ($y = -3.5$ km) and L2 ($y = -1.0$ km), for three different model discretizations using PHS RBF-FD (panels **a** and **c**) and scalar FE (panels **b** and **d**) methods. The three model discretizations are distinguished by the total number of points, N.

of g_z over each tetrahedral element. Although the two linear systems of equations resulting from the FE and RBF-FD schemes have the same dimension, the coefficient matrices of the two systems have different sparsities, or different numbers of non-zero entries. The coefficient matrix of the PHS RBF-FD with $n = 30$ is generally denser than that of the linear FE.

In this example, three different model discretizations were generated with the total number of points as N = 62,418, 73,047, and 83,948, respectively. The three discretizations are obtained by using increasingly higher quality controls in generating the mesh without changing the local refinement constraints. Therefore, a discretization with more points can be considered as a global refinement of the previous one with fewer points. The corresponding total numbers of tetrahedral elements are N_{ele} = 392,363, 459,129 and 526,796, respectively. The computed g_z for these discretizations are plotted in Fig 3.11, and the differences (i.e., absolute errors) between the numerical solutions and the analytical solution are plotted in Fig 3.12. The results show that both RBF-FD and linear FE solutions converge to the true solution as N increases. Although the RBF-FD solution has larger deviations from the analytical solution than the FE solution when $N = 62,418$, the RBF-FD solution is more accurate than the FE counterpart when $N = 83,948$, as shown in Fig 3.12. This is because the PHS RBF-FD enriched with quadratic polynomials has a nonlinear convergence rate, whereas the linear FE has only a linear convergence rate. Also, the linear FE solution is less smooth than that of PHS RBF-FD.

In terms of computational efficiency, the RBF-FD method implemented here is generally slower than the linear FE method in assembling and solving the system of algebraic equations. The assembling process refers to deriving RBF-FD or FE weights

and forming the coefficient matrix of the linear system. The solving phase refers to solving the linear system after assembling. The main reasons for more computational cost from the RBF-FD are that firstly, the local interpolation linear system described in eq (2.21) needs to be numerically evaluated, as opposed to analytical evaluation in the case of linear FE with tetrahedral elements (the FE interpolation linear system has the dimension 4×4). Secondly, the RBF-FD implemented with the fixed stencil size $n = 30$ is likely to generate more non-zero entries than the linear FE method, resulting in more factorization time during the solving phase. For example, when $N = 73,047$, in which case the RBF-FD and linear FE gave comparable accuracies of g_z, the number of non-zero entries in the RBF-FD linear system was $nz = 2,187,814$, while in the linear FE the number was $nz = 1,137,641$. The computational time in seconds for the meshfree solution was $t = 33.410$ s (28.407 s for matrix assembling, and 5.003 s for solving phase), while the same computational time for the FE solution was $t = 18.624$ s (14.427 s for matrix assembling, and 4.197 s for solving phase).

In practice, post-processing time for numerical solutions can also be non-negligible, despite the fact that it is mostly a fraction of the entire running time. The post-processing time for numerical methods such as FE and RBF-FD is referred to as the amount of time needed to obtain derivatives (e.g., vertical gravities or gravity gradients here) from the solutions (e.g., gravity potentials here) to the linear system. For this example with $N_{site} = 200$ measurement sites, the RBF-FD required 0.1 s to obtain the vertical gravities from potentials, whereas the linear FE needed 3.172 s. The substantially less processing time for the former is due to the use of k-dimensional tree[2] structures in searching meshfree subdomains, which is a common

[2]Here, k represents the spatial dimension. k-dimensional tree structures are a type of method to

method to group unconnected points. The longer FE processing time is due to necessary geometry searching calculations (N_{site} times) in a standard FE implementation, for example finding which elements a specific vertex or measurement site belongs to in the unstructured mesh. Such geometry searching calculations, for which the efficiency is dependent on the implementation algorithm and available outputs from mesh generation software, are also needed N times (for N degrees of freedom) prior to the assembling of the global linear system.

3.6 Chapter summary

Convergence analysis and performance of PHS RBF-FD are presented in the example of modelling gravity data. It is numerically demonstrated that the PHS RBF-FD (with PHS as r^5) converges to the exact solution under global and local point refinements. A nonlinear h convergence rate can be obtained by enriching the PHS RBF-FD with nonlinear polynomials when constructing meshfree interpolation in subdomains. The PHS RBF-FD stencil size determines the number of points in each meshfree subdomain. For the case of using a constant stencil size (n) for all subdomains, the numerical solution using the PHS RBF-FD is shown to be not improved by using very large n. On the other hand, using very small stencil sizes ($n \leqslant 20$) in the 3-D case results in inaccurate solutions. The numerical tests suggest that using $n = 30$ is mostly adequate for accuracy of RBF-FD approximations of derivatives up to second order (e.g., Laplacian operator). A comparison of performance between using the PHS RBF-FD and using a linear scalar FE method shows that the RBF-FD

organize data.

computation is generally more expensive than that of linear FE for a discretization with the same number of degrees of freedom. The main reason is because of the numerical evaluation of interpolation linear systems of equations with the dimension as $n + m$ in the RBF-FD case, with n as the number of points in a subdomain and m as the number of the enriched polynomials.

Chapter 4

Simulation of magnetotelluric data using PHS RBF-FD

4.1 Introduction

The magnetotelluric (MT) method is a natural source EM survey method that assumes a plane wave incident EM field at the surface of the Earth as the signal. Although the true sources, such as lightning and solar radiation, produce non-plane wave EM fields, they are far away from the Earth's surface and therefore the plane wave approximation is valid for EM frequencies of MT surveys (Evans, 2012). The frequencies used in the MT method are typically very low (between 0.0001 Hz and 10 Hz) and the penetration depth of MT signals can reach dozens or hundreds of kilometres. In terms of the numerical modelling of MT data, the mathematical equations (Maxwell's equations) describing the propagation of the EM fields are the same as those for the controlled-source EM method. However, as there is no source term in

Maxwell's equations for the MT method, numerical issues related to singularity near sources can be avoided in the MT case.

Over the years, the MT method has seen intensive developments and applications of 3-D EM forward modelling and inversion algorithms. The development history of 3-D algorithms for the method follows the description given in Chapter 1. Two particular example studies, for instance, that reflect the pattern of MT algorithm development are Zhdanov et al. (1997) and Miensopust et al. (2013). In Zhdanov et al., the authors summarized major modelling algorithms for MT data at that time, which were mostly based on the IE method, and proposed a number of benchmark 2-D and 3-D conductivity models for which solutions using different algorithms can be compared against. Miensopust et al., in an uncommon instance, compared modelling and inversion results of 3-D synthetic MT data using various 3-D codes that had been developed by different researchers over the previous two decades. In this comparison study, it was found that most of the available codes were based on algorithms of FD method. In the recent ten years, a new trend is that FE method-based modelling and inversion algorithm developments have been increasingly popular and routine, if not dominant, in 3-D MT studies (e.g., Liu et al., 2008; Farquharson & Miensopust, 2011; Grayver & Burg, 2014; Usui, 2015; Kordy et al., 2016; Jahandari & Farquharson, 2017), which is likely because of the acknowledgement of the advantages of FE modelling methods in dealing with complex Earth models.

In this chapter, the meshfree PHS RBF-FD is extended and applied to modelling 3-D MT data. While the gravity potential function is high order smooth in nature, the EM field due to a general 3-D inhomogeneous conductivity model can be discontinuous. The feasibility and applicability of using RBF-FD in dealing with 3-D

conductivity models are presented here.

4.2 A-ψ potential scheme with Coulomb gauge condition

EM fields propagating within a general Earth model are described by Maxwell's equations and constitutive relations between physical properties (i.e., electrical conductivity σ, electrical permittivity ϵ and magnetic permeability μ) and the EM fields. In the frequency domain, the EM fields change harmonically in time and Maxwell's equations can be written as

$$\nabla \times \mathbf{E} = -i\omega\mathbf{B}, \tag{4.1}$$

$$\nabla \times \mathbf{H} = \mathbf{J}_c + i\omega\mathbf{D} + \mathbf{J}_{exter}, \tag{4.2}$$

$$\nabla \cdot \mathbf{B} = 0, \tag{4.3}$$

$$\nabla \cdot \mathbf{D} = \rho. \tag{4.4}$$

In eqs (4.1)-(4.4), i is the imaginary unit, $\omega = 2\pi f$ is angular frequency (the time dependence $e^{i\omega t}$ is implied here), $\mathbf{E}$ is the electric field, $\mathbf{H}$ is the magnetic field, $\mathbf{D}$ is displacement electric current density vector, and $\mathbf{B}$ is magnetic induction vector. $\mathbf{J}_c$ is conductive current density that only exists in a conductive medium, and $\mathbf{J}_{exter}$ is the EM source term expressed in the form of an electric current density ($\mathbf{J}_{exter}$ is zero for the MT case). Finally, ρ is the volume density of electric charges which in the case of MT method is only nonzero at the conductivity jumps of an Earth model.

The interactions between the EM fields and the medium through which the fields propagate are described by the constitutive relations. In this thesis, the physical properties (σ, ϵ, μ) of the medium are assumed to be only dependent on the spatial position ($\mathbf{r}$) and thus the medium is isotropic, nondispersive (i.e, frequency independent) and linear (the physical properties are not affected by the applied EM fields), etc. In this case, the constitutive relations are expressed in the simple form as

$$\mathbf{J}_c = \sigma \mathbf{E}, \tag{4.5}$$

$$\mathbf{D} = \epsilon \mathbf{E}, \tag{4.6}$$

$$\mathbf{B} = \mu \mathbf{H}. \tag{4.7}$$

For numerical modellings of EM data for a general conductivity model, there are many different derived forms of Maxwell's equations that can be used (Hohmann, 1983). A commonly used form is the Helmholtz equation for the $\mathbf{E}$ field, which is derived by substituting eq (4.1) into eq (4.2) and taking advantage of the relations in eqs (4.5)-(4.7). The $\mathbf{E}$ field Helmholtz equation is thus given as

$$\nabla \times \mu^{-1} \nabla \times \mathbf{E} + i\omega\sigma\mathbf{E} - \omega^2 \epsilon \mathbf{E} = \mathbf{0}. \tag{4.8}$$

For the MT method here, the frequency is very low such that the high order term $\omega^2\epsilon\mathbf{E}$ can be neglected, which is the case of the quasi-static approximation (Ward & Hohmann, 1988). Further, the magnetic permeability can be assumed to be the constant value of free air if only the conductivity structure of an Earth model is involved. As a result, the modified Helmholtz equation for the $\mathbf{E}$ field that is used

for a numerical solution is given as

$$\nabla \times \nabla \times \mathbf{E} + i\omega\mu\sigma\mathbf{E} = \mathbf{0}. \tag{4.9}$$

The **E**-field Helmholtz equation has the vector **E** field as the unknown function. The total **E** field can be discontinuous in the computational domain for a given modelling problem, posing a difficulty in discretizing the equation. In mesh-based methods such as staggered-grid based FD, FV and vector FE, this difficulty is avoided by taking the degrees of freedom as the tangential **E** fields along the edges of the mesh, which are always continuous throughout the domain. In the scalar FE method, for example, the degrees of freedom would be all three scalar components of the **E** field associated with the vertices in the mesh if eq (4.9) is used to derive a numerical solution. However, the scalar FE method forces all three components to be continuous even at the conductivity jumps, and thus violates the physical behaviours of a possibly discontinuous **E** field function. Similarly, if using meshfree approaches together with the **E**-field Helmholtz equation, the same violation of the physical nature of the **E** field would occur, since the degrees of freedom are all defined at the points in the meshfree discretization.

To avoid the discretization difficulty in the case of meshfree numerical methods, equations of continuous functions need to be used. When considering only the conductivity as the changing physical property, there are at least two options available. One is to use EM potential functions as the unknowns. It is well known that EM potential functions are smoother than the **E** and **H** fields (Biro & Preis, 1989, 1990; Badea et al., 2001). The other is to use the **H** field-based Helmholtz equation where

the magnetic field is the unknown function (Mackie et al., 1994; Siripunvaraporn et al., 2002). The **H** field-based equation systems would involve the same solution discontinuities in **H** if an Earth model has abrupt magnetic material jumps, that is jumps of the physical property μ. In this chapter, the **A**-ψ EM potential system of equations (e.g., Biro & Preis, 1989), with **A** the magnetic vector potential and ψ the electric scalar potential, is used in the frame of PHS RBF-FD meshfree method.

4.2.1 A-ψ potential equations

In the **A**-ψ scheme, the **E** and **H** fields are represented by **A** and ψ. According to eq (4.3), the vector field **B** is solenoidal and can be represented by the curl of a vector potential function **A**:

$$\mathbf{B} = \nabla \times \mathbf{A}. \tag{4.10}$$

Substituting eq (4.10) into eq (4.1) and using the Helmholtz decomposition theorem for the vector field **E** (Harrington, 2001), one obtains

$$\mathbf{E} = -i\omega\mathbf{A} - \nabla\psi, \tag{4.11}$$

where ψ here is an arbitrary and sufficiently differentiable scalar function (thus called electric scalar potential). $\nabla\psi$ is needed here to uniquely decompose **E**. Subsequently, the Helmholtz equation for **A** can be obtained by substituting eq (4.11) into the **E**-field Helmholtz equation of eq (4.9):

$$\nabla \times \nabla \times \mathbf{A} + i\omega\mu\sigma\mathbf{A} + \sigma\mu\nabla\psi = \mathbf{0}. \tag{4.12}$$

In order to determine a solution to eq (4.12), an additional equation is required. Here, the equation of conservation of charge for $\mathbf{A}$ and ψ is used (Biro & Preis, 1989; Badea et al., 2001). It is obtained by taking the divergence of eq (4.12):

$$\nabla \cdot (i\omega\mu\sigma\mathbf{A} + \sigma\mu\nabla\psi) = 0. \tag{4.13}$$

In deriving eq (4.12) and eq (4.13), the vector identities $\nabla\times\nabla f = \mathbf{0}$ and $\nabla\cdot\nabla\times\mathbf{F} = 0$ for any arbitrary and sufficiently differentiable functions f and $\mathbf{F}$ have been used.

The $\mathbf{A}$-ψ scheme solves eqs (4.12) and (4.13) first, then computes the $\mathbf{E}$ and $\mathbf{H}$ ($\mathbf{H} = \frac{1}{\mu}\mathbf{B}$) fields by the relations in eq (4.10) and eq (4.11). The numerical solution to eqs (4.12) and (4.13) is however not unique. The non-uniqueness is caused by only specifying the curl part of the vector potential $\mathbf{A}$, which is eq (4.10), and leaving the divergence part of $\mathbf{A}$ undetermined (Stratton, 2007). A common way to obtain a unique numerical solution for the $\mathbf{A}$-ψ scheme is to use gauge conditions (Biro & Preis, 1989; Harrington, 2001). In this thesis study, the Coulomb gauge condition $\nabla \cdot \mathbf{A} = 0$ is explicitly introduced in the form of $\nabla(\nabla \cdot \mathbf{A})$ to eq (4.12) (e.g., Badea et al., 2001). The gauged Helmholtz equation for $\mathbf{A}$ then becomes

$$\nabla \times \nabla \times \mathbf{A} - \nabla(\nabla \cdot \mathbf{A}) + i\omega\mu\sigma\mathbf{A} + \sigma\mu\nabla\psi = \mathbf{0}, \tag{4.14}$$

which can be further recast as

$$-\nabla^2\mathbf{A} + i\omega\mu\sigma\mathbf{A} + \sigma\mu\nabla\psi = \mathbf{0}, \tag{4.15}$$

according to the vector identity $\nabla \times \nabla \times \mathbf{A} = \nabla(\nabla \cdot \mathbf{A}) - \nabla^2\mathbf{A}$. The Coulomb

gauged $\mathbf{A}$-ψ scheme solves the pair of eqs (4.15) and (4.13). It can be shown that (Appendix B), by solving these two equations, eqs (4.15) and (4.13), with appropriate boundary conditions for the potentials, the divergence condition $\nabla \cdot \mathbf{A} = 0$ will be forced to hold everywhere in the computational domain.

In implementing the PHS RBF-FD for solving eqs (4.15) and (4.13), the component-wise form is used:

$$-\nabla^2 A_x + i\omega\mu\sigma A_x + \sigma\mu\frac{\partial\psi}{\partial x} = 0, \tag{4.16}$$

$$-\nabla^2 A_y + i\omega\mu\sigma A_y + \sigma\mu\frac{\partial\psi}{\partial y} = 0, \tag{4.17}$$

$$-\nabla^2 A_z + i\omega\mu\sigma A_z + \sigma\mu\frac{\partial\psi}{\partial z} = 0, \tag{4.18}$$

$$i\omega\mu\sigma(\frac{\partial A_x}{\partial x} + \frac{\partial A_y}{\partial y} + \frac{\partial A_z}{\partial z}) + \sigma\mu\nabla^2\psi = 0. \tag{4.19}$$

In eq (4.19), the condition $\nabla\sigma = 0$ has been implied, indicating dealing with regular regions of constant conductivity distribution. For possible non-constant conductivity regions, the term $\nabla\sigma$ needs to be incorporated into the implementation. The three scalar components of $\mathbf{A}$ (A_x, A_y, A_z) and ψ are the degrees of freedom that are associated with each point in a meshfree point discretization. The RBF-FD approximations of the differential operators in eqs (4.16)-(4.19) ($\frac{\partial}{\partial x}$, $\frac{\partial}{\partial y}$, $\frac{\partial}{\partial z}$ and ∇^2) are described in Section 2.4.1.

The matrix form of eqs (4.16)-(4.19) is given as

$$\begin{pmatrix} D_1 & 0 & 0 & D_2 \\ 0 & D_1 & 0 & D_3 \\ 0 & 0 & D_1 & D_4 \\ i\omega D_2 & i\omega D_3 & i\omega D_4 & D_5 \end{pmatrix} \begin{pmatrix} A_x \\ A_y \\ A_z \\ \psi \end{pmatrix} = \begin{pmatrix} 0 \\ 0 \\ 0 \\ 0 \end{pmatrix}, \tag{4.20}$$

where the expressions for differential operators $D_j, (j = 1, \cdots, 5)$ are detailed in Table 4.1. Once D_j are approximated as RBF-FD weights, a compact matrix form of the resulting linear system of equations can be obtained as the following

$$\begin{pmatrix} \mathbf{D}_1 & \mathbf{0} & \mathbf{0} & \mathbf{D}_2 \\ \mathbf{0} & \mathbf{D}_1 & \mathbf{0} & \mathbf{D}_3 \\ \mathbf{0} & \mathbf{0} & \mathbf{D}_1 & \mathbf{D}_4 \\ i\omega\mathbf{D}_2 & i\omega\mathbf{D}_3 & i\omega\mathbf{D}_4 & \mathbf{D}_5 \end{pmatrix} \begin{pmatrix} A_x \\ A_y \\ A_z \\ \psi \end{pmatrix} = \begin{pmatrix} \mathbf{R}_1 \\ \mathbf{R}_2 \\ \mathbf{R}_3 \\ \mathbf{R}_4 \end{pmatrix}, \tag{4.21}$$

where the block matrices $\mathbf{D}_j, (j = 1, \cdots, 5)$ contain the assembled RBF-FD weights for approximating D_j. The right-hand side block matrices $\mathbf{R}_j, (j = 1, \cdots, 4)$ are the results of incorporating boundary values of $\mathbf{A}$ and ψ into the linear system. The coefficient matrix in eq (4.21) is a complex-valued, asymmetric sparse matrix.

4.2.2 MT impedance response

The MT impedance tensor, or electric transfer function, $\mathbf{Z}$, is considered here as the modelling data. The impedance tensor is dependent on the conductivity distribution in the subsurface and the EM source frequency. It can be numerically computed from

Table 4.1. Differential operators used in eq (4.20).

Term	**expression**
D_1	$-\nabla^2 + i\omega\mu\sigma$
D_2	$\mu\sigma\frac{\partial}{\partial x}$
D_3	$\mu\sigma\frac{\partial}{\partial y}$
D_4	$\mu\sigma\frac{\partial}{\partial z}$
D_5	$\mu\sigma\nabla^2$

the ratio information of **E** and **H** fields. In the case of 3-D MT problems, **Z** can be obtained by solving twice the forward modelling under two different and orthogonal plane-wave source polarization modes. Since in the MT method the source fields, $\mathbf{E}_s$ and $\mathbf{H}_s$, are also orthogonal for each mode, the polarization mode with $\mathbf{E}_s$ aligned with x direction (thus, the source magnetic field, $\mathbf{H}_s$, is aligned with y direction) in a Cartesian coordinate system is denoted as E-x mode. Similarly, the polarization mode with $\mathbf{E}_s$ aligned with y direction (thus, the source magnetic field, $\mathbf{H}_s$, is aligned with x direction) is denoted as E-y mode. In each mode, there are corresponding induced **E** and **H** field measurements at the surface as a result of the source field.

The components of the 2×2 impedance tensor are then given by solving the following matrix equation

$$\begin{pmatrix} E_{x1} & E_{x2} \\ E_{y1} & E_{y2} \end{pmatrix} = \begin{pmatrix} Z_{xx} & Z_{xy} \\ Z_{yx} & Z_{yy} \end{pmatrix} \begin{pmatrix} H_{x1} & H_{x2} \\ H_{y1} & H_{y2} \end{pmatrix}, \tag{4.22}$$

where the indices 1 and 2 denote the numerical solutions of **E** and **H** from the forward modelling under the E-x and E-y modes, respectively. The subscripts x and y indicate

the two perpendicular horizontal components of each field. The computed tensor components (Z_{xx}, Z_{xy}, Z_{yx}, and Z_{yy}), which are complex-valued, are often plotted as the apparent resistivity (ρ) and phase curves which are obtained by

$$\rho_{kj} = \frac{1}{\omega\mu}|Z_{kj}|^2, \tag{4.23}$$

$$\phi_{kj} = \tan^{-1}\left(\frac{ImZ_{kj}}{ReZ_{kj}}\right), \quad k = x, y;\ j = x, y. \tag{4.24}$$

4.2.3 Boundary condition

The computational domain in the following examples of MT modelling is set to be a rectangular box. Each plane side of the boundary of the domain needs to be assigned with proper boundary values of $\mathbf{A}$ and ψ. In the PHS RBF-FD method, there is always some amount of points distributed on the boundary. Here, Dirichlet-type boundary values of the potentials are prescribed at the points for obtaining a unique numerical solution. The 1-D method described in Weaver (1994) is used for 3-D conductivity models with a 1-D background model such as a half-space (including an air layer) or a layered model. The formulation for computing the boundary values of the electric field using the 1-D method is discussed in Appendix C.

Once the boundary $\mathbf{E}$ field is obtained, the boundary values for the potentials can be determined according to eq (4.11). Since in most situations the 3-D inhomogeneities are far away from the boundary sides, there is no electric charge built up at the boundaries. Thus, $\nabla\psi = 0$ holds at the boundaries, making ψ a constant function

(set to be $\psi = 0$ here[1]). The boundary values for $\mathbf{A}$ are then given as

$$(A_x, A_y, A_z, \psi) = (-\frac{1}{i\omega}E_x, 0, 0, 0), \tag{4.25}$$

for the E-x mode. Similarly, the boundary values for the E-y mode are given as

$$(A_x, A_y, A_z, \psi) = (0, -\frac{1}{i\omega}E_y, 0, 0). \tag{4.26}$$

The Dirichlet boundary conditions in eqs (4.25) and (4.26) fulfill the divergence condition $\nabla \cdot \mathbf{A} = 0$ at the boundaries.

4.3 Challenge of discontinuities

The PHS RBF-FD meshfree method presented in Chapter 3 is applicable to solve any differential equations that have sufficiently smooth functions (e.g., C^1 continuous functions) as the unknown quantities. Such situations include for example Poisson's equations for gravity (as demonstrated in the previous chapter), Navier-Stokes equations for fluid flows and dynamics (Wu & Liu, 2003; Wright et al., 2010), geophysical seismic wave field modelling (Takekawa et al., 2015; Martin et al., 2015), and 2-D MT modelling (Wittke & Tezkan, 2014). However, a standard meshfree method such as RBF-FD faces a major difficulty in faithfully reproducing possible discontinuous functions when applied to modelling 3-D EM fields in general. In geophysical diffusive EM data simulation, discontinuities of the electric field arise when the conductivity dis-

[1]Unlike the unique determination of the vector potential $\mathbf{A}$, the Coulomb gauged $\mathbf{A}$-ψ scheme determines a unique ψ up to a constant C since $\nabla(\psi + C) = \nabla\psi$, i.e., the scheme uniquely determines a pair of $(\mathbf{A}, \nabla\psi)$.

tribution has sudden changes or jumps, which are common for a geological model featuring different rock units with sharp contrasts in their homogeneous conductivities. The difficulty is caused by the nature of constructing a standard meshfree function approximation, in which the approximant is guaranteed to be high order smooth (at least C^1 continuous) everywhere in a meshfree subdomain (Belytschko et al., 1996). As a result, spurious solutions will occur if applying such standard meshfree methods in solving the 3-D EM field simulation problems (Herault & Marechal, 1999).

In the mesh-based methods, the function discontinuities in EM data simulation are dealt with by aligning the material discontinuities (i.e., conductivity jumps) with elemental interfaces in the mesh. In the meshfree case, there is however no explicit geometry of the meshfree subdomains, which are mostly overlapping (Fig 4.1). To remove the spurious meshfree solutions related to the function discontinuities, two groups of approaches are typically used. In the first group, the idea is to firstly construct meshfree subdomains by ignoring the material jumps (conductivity interfaces), which may or may not intersect the subdomains, and then modify the standard meshfree function approximation over any subdomain that is indeed cut by the interfaces. The purpose of the modification of function approximation is to reproduce the desired discontinuities in the approximated function or its derivatives. Among these modification methods, the most popular method is to enrich the standard meshfree approximant with additional C^0 basis functions having the discontinuities in derivatives at the interfaces (Cordes & Moran, 1996; Krongauz & Belytschko, 1998; Batra et al., 2004; Xu & Belytschko, 2005; Joyot et al., 2005). This is suitable for EM potential functions since $\mathbf{A}$ and ψ are continuous themselves but their first-order derivatives may not be so. Another option is, instead of a partial enrichment, to construct the

meshfree approximant entirely using C^0 basis functions (Yu & Chen, 2011). The main drawback in the modification approaches is that such modification is highly dependent on the geometry of the physical property interfaces. For example, if the normal discontinuity in function derivatives is desired, the normal directions at all the interfacial points are then required. The determination of these normal directional vectors can be computationally expensive for a set of scattered points located on complex 3-D surfaces, and can be even impossible if the 3-D surface is not smooth (e.g., the tips of the surface of a rectangular prism). Another issue of these approaches, albeit less severe, is that extra degrees of freedom are introduced in the meshfree function approximation (Xu & Belytschko, 2005). Due to the (derivative) discontinuities in the constructed approximant, the algebraic equations for the interfacial points must be obtained by using weak form integrals, which are evaluated numerically and are typically carried out using high-order Gauss quadrature methods after partitioning the integration domain into multiple regular regions (the partition often means a local or global mesh needs to be constructed, although solely for quadrature, see Krongauz & Belytschko, 1998).

In the second group, the idea is to never form any meshfree subdomain that intersects the physical property interfaces. This can be done by, for example, truncating any subdomain that is cut by an interface into two new subdomains along the interface, each of which thus has a homogeneous physical property. Over these two new subdomains, standard meshfree approximations can then be used (Li et al., 2003; Nicomedes et al., 2011; Lima et al., 2012; Jalušić et al., 2017). One prominent advantage of this idea is that it is capable of dealing with arbitrarily shaped interfaces in a model. As there is no link of the continuity requirements between the

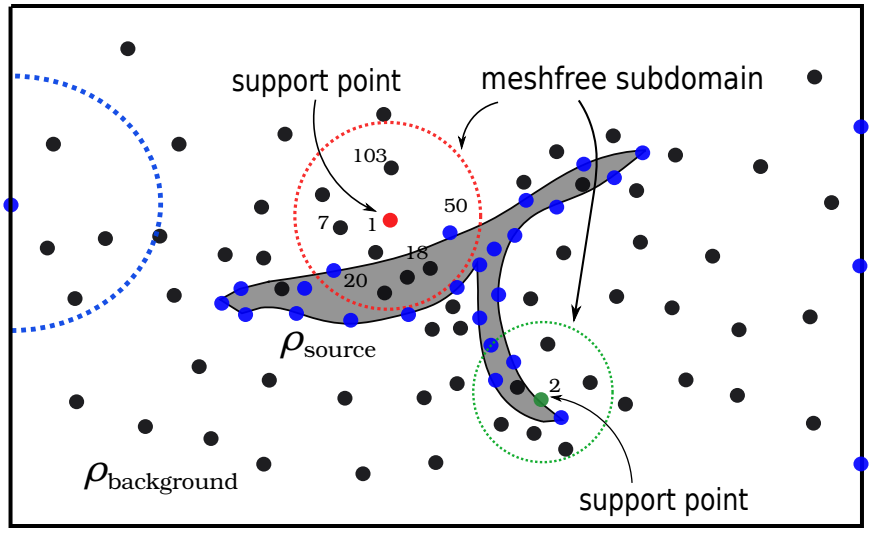

Figure 4.1. Schematic illustration of different meshfree subdomains for different points. Points on the boundaries of the problem domain and on the interfaces are coloured blue, and interior points are coloured black.

two subdomains, the approximated function may have both normally and tangentially discontinuous derivatives, which is undesirable in the EM problem (Herault & Marechal, 1999). To enforce the physical continuities, the continuity or discontinuity equations (such as $E_{\parallel,1} = E_{\parallel,2}$ for the tangential component and $\sigma_1 E_{\perp,1} = \sigma_2 E_{\perp,2}$ for the normal component of the electric field) at the interface need to be explicitly incorporated into the linear system resulting from discretizing PDEs.

A common method of such incorporation is to use a Lagrange multiplier in the form of a weak-form integral for each continuity equation (Herault & Marechal, 1999; Li et al., 2003; Lima et al., 2012). The Lagrange multipliers inevitably introduce extra degrees of freedom. Also, the integrals need to be numerically evaluated, as in the first group of approaches. Another method of incorporation is to directly enforce the continuity equations at the interface points in a strong form. In the case of $\mathbf{A}$-ψ

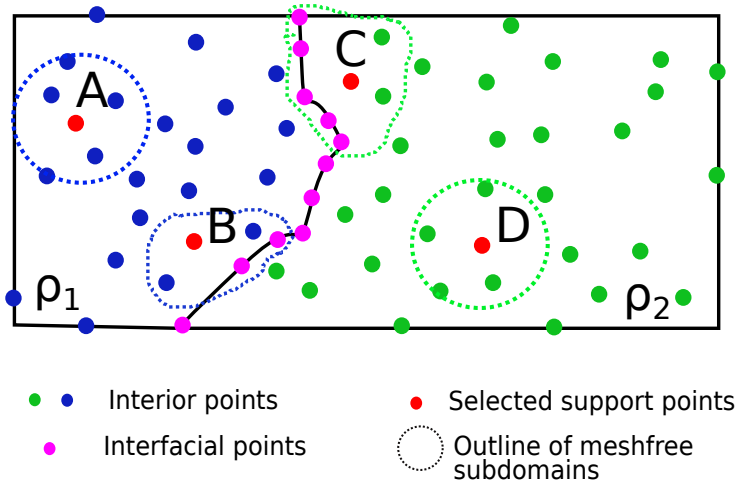

Figure 4.2. Different meshfree subdomains in the partitioned regions. Shown above are two different physical regions with the resistivities ρ_1 and ρ_2. Meshfree points are distributed in both regions and at their interface. Subdomains for those support points far away from the interface (e.g., A and D) include only the points belonging to the same region as the support points. Subdomains for those support points close to the interface (e.g., B and C) include some interfacial points as well as interior points, but not any points on the other side of the interface.

potential schemes, this can be done by applying the following equations

$$-i\omega A_{\parallel,1} - (\nabla\psi)_{\parallel,1} = -i\omega A_{\parallel,2} - (\nabla\psi)_{\parallel,2}, \tag{4.27}$$

$$-i\omega\sigma_1 A_{\perp,1} - \sigma_1(\nabla\psi)_{\perp,1} = -i\omega\sigma_2 A_{\perp,2} - \sigma_2(\nabla\psi)_{\perp,2}, \tag{4.28}$$

for each point at the interface. The $\mathbf{A}$-ψ equations above are based on the continuity equations of the electric field ($\mathbf{E} = -i\omega\mathbf{A} - \nabla\psi$). The subscript 1 (or 2) denotes that the potential functions are approximated using the meshfree points located in the subdomain in region 1 (or 2, see Fig 4.2). σ_1 and σ_2 are the homogeneous conductivities from regions 1 and 2, respectively. As there are often more than one continuity equation for each interfacial point, the same degrees of freedom (unknowns) associ-

ated with a point are repeated in the linear system of equations when incorporating the continuity equations into the linear system, as if they were additional unknowns. Because of this, the layer of interfacial points is said to be 'doubled' or 'tripled', depending on the number of continuity equations for each point. This incorporation method is sometimes called the double-layer method (Nicomedes et al., 2011). An obvious advantage of this method is that integrals, and thus numerical quadrature, are completely avoided in enforcing the continuity conditions. However, there are at least two important issues left to be addressed: (1) the physical interactions between the **E** and **H** fields (e.g., Faraday's law) at the interface are not numerically translated into the linear system of equations, and (2) the linear independence among the added continuity equations is not guaranteed.

To address the discontinuity issue in the PHS RBF-FD method, a hybrid RBF-FD meshfree method that incorporates a weak-form treatment for the interfacial points is proposed in this study. The key idea of the hybrid RBF-FD method is to use a local mesh to construct the integrals that can be carried out analytically. To do this, the computational domain is partitioned firstly into different sub-regions with homogeneous or continuously varying conductivity values. This partition is typically done in the process of building up an Earth model in the first place and before a forward modelling is considered. Then, a desired number of meshfree points are generated with some of them located at the material interfaces. The meshfree subdomains are formed in the same way as those in the second group of approaches mentioned above, namely, the RBF-FD subdomains for non-interfacial points are never cut through by the interfaces (Fig 4.2). To facilitate the formations of the subdomains in different sub-regions, a separate k-dimensional tree of 3-D points for

each sub-region is created. As a result, the RBF-FD approximation using the standard RBF-based interpolations can be used without issues.

For the interfacial points, their meshfree subdomains are firstly formed in a standard way as if there were no interface, as in the aforementioned modification approaches. Then, a local mesh containing the meshfree points in the subdomain is formed. This is a novel part compared to previous studies that employ weak form integrals to handle discontinuities, which use either modifications of meshfree approximant or Lagrange multipliers. In those methods, the integrals based on the meshfree function approximation are formed firstly, which does not need any local mesh. However, the resultant integrands are often high-order rational functions and thus the volume integrations of them cannot be carried out analytically. A sophisticated domain partitioning (i.e., local mesh construction) and/or mappings are then required to numerically carry out the evaluation of integrals with accuracy (Belytschko et al., 1994; Krongauz & Belytschko, 1998; Atluri et al., 1999; Dolbow & Belytschko, 1999; Jia & Hu, 2006; Wittke & Tezkan, 2014; Hillman & Chen, 2016). The numerical quadrature process becomes more complicated and expensive in dealing with 3-D problems (Li et al., 2003). In the hybrid method proposed here, the weak form integrals are formed in an opposite way: a local 3-D mesh within the formed subdomain overlapping with the interfaces (Fig 4.3) is constructed first. Then, a mesh-based function approximation is carried out. For the unstructured points, a local tetrahedral mesh can be used. Over the tetrahedral elements, the standard linear finite element (FE) Galerkin method is chosen in this study to form the integrals. Here, the purpose of the local meshes for interfacial points is to allow for a weak form discretization of the PDEs (e.g., $\mathbf{A}$-ψ equations), whereas the purpose of them in the

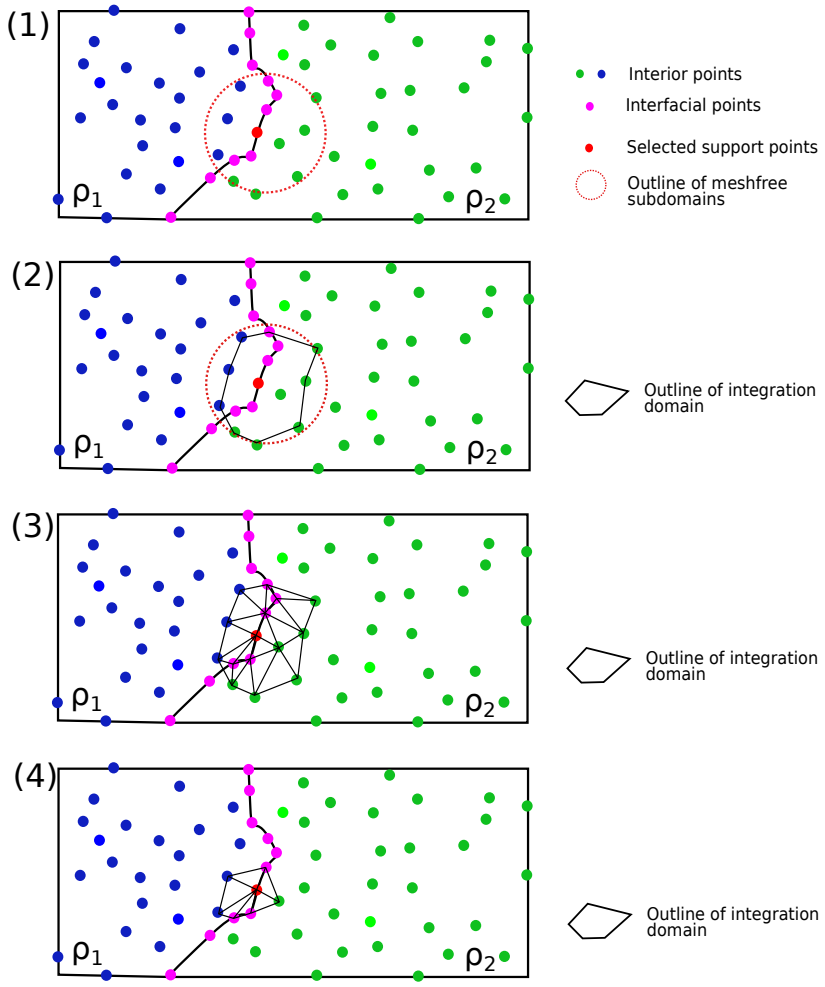

Figure 4.3. Demonstration of the incorporation of the weak-form integration in the hybrid RBF-FD method. There are three steps in forming the local subdomain for an interfacial support point: (i) construct a normal meshfree subdomain as if there is no interface (panel 1); (ii) construct a local mesh among the points within the subdomain (panels 2 and 3); and (iii) select the required sub-mesh from the mesh formed in Step 2 by excluding unnecessary points, depending on the weak form method (panel 4).

aforementioned previous approaches is to facilitate numerical integrations.

The rationales behind this hybrid method for dealing with discontinuities of function derivatives are threefold. First, it is well known that the integration from FE methods using common types of element (e.g., prisms and tetrahedra) can be analytically carried out, effectively circumventing computationally expensive quadrature. Second, since the local meshfree points for a subdomain are already available, the construction of the small, local mesh within that subdomain is significantly easier than the counterpart when numerically carrying out a meshfree volume integration for that subdomain's support point. In the latter, the region to be meshed, or the integration domain, may be much larger than the subdomain's occupying volume (i.e., the smallest sphere containing all the points) since the meshfree shape functions may not be compactly supported (Dolbow & Belytschko, 1999). Third, the RBF-FD meshfree discretization can be easily coupled with that of grid-based FD and scalar FE/FV methods when the unknowns are defined at the points. It is worth noting that in the second rationale, the local mesh only serves as providing a bounded and compact integration region and is constructed based on the existing points in a meshfree subdomain (30 to 50 points in solving 3-D EM modellings here). As such, the local mesh generation does not face the difficulty of conforming to irregular geometries of the interface while still ensuring quality cells in a traditional mesh-based method.

The procedure of deriving algebraic equations using the local meshes for interfacial points, for which a graphical demonstration is shown in Fig 4.3, is the same as that described in Badea et al. (2001), for example. For each interfacial point that has $n_l - 1$ ($n_l > 2$) neighbouring points used in the weak form integration, the derived FE weights, c_j, in discretizing any of the differential operators in Table 4.1 are obtained

by the approximation

$$< u, D_k f >= \sum_{j=1}^{n_l} c_j f_j, \quad 1 \leqslant k \leqslant 5, \quad k \in \mathbb{N}, \tag{4.29}$$

where $<,>$ denotes a bilinear form of the inner product with u as the test function in the Galerkin FE method, and f_j denotes the function values of one of the potential function components (A_x, A_y, A_z and ψ) at the n_l points. In the linear FE method, f is approximated as a linear function within each tetrahedral cell before the inner product in eq (4.29) is evaluated:

$$f \approx a + bx + cy + dz = \sum_{j=1}^{4} N_j(x, y, z) f_j, \tag{4.30}$$

where N_j are the FE shape functions and the coefficients (a, b, c, d) are obtained by a Lagrange interpolation (Badea et al., 2001; Jin, 2014).

4.4 Numerical examples

4.4.1 COMMEMI model 3D-1A

The conductivity model for this first example is the benchmark model COMMEMI[2] 3D-1A (Zhdanov et al., 1997). The model has a single rectangular conductor ($\sigma = 2.0$ S/m) embedded in the more resistive background subsurface ($\sigma = 0.01$ S/m). The conductor has the dimensions as $-0.5 \leqslant x \leqslant 0.5$ km, $-1.0 \leqslant y \leqslant 1.0$ km, and $-2.25 \leqslant z \leqslant -0.25$ km. Perspective views of the model are shown in Fig 4.4.

[2]COMMEMI stands for Comparison Of Modelling Methods for ElectroMagnetic Induction.

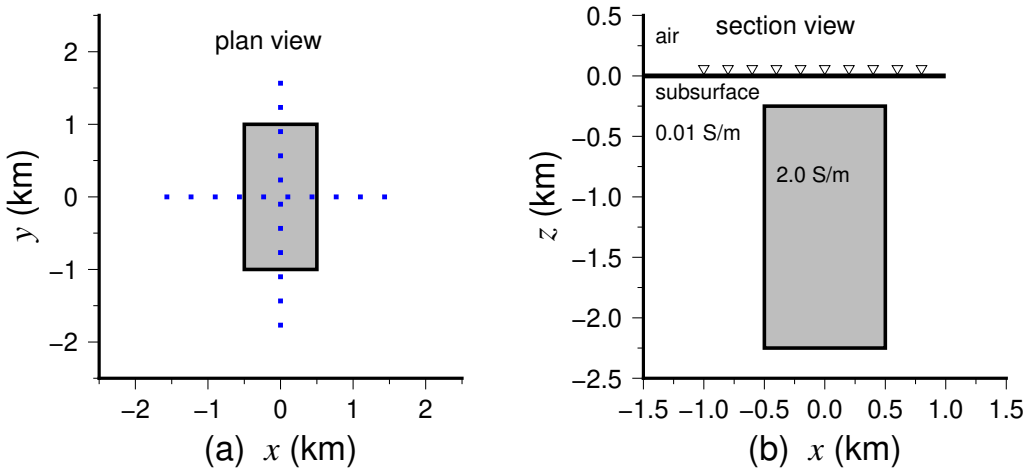

Figure 4.4. Plan (a) and section (b) views of the COMMEMI 3D-1A conductivity model. The conductor is indicated by the shaded block. Two perpendicular measurement lines are located at the air-Earth surface ($z = 0$ km) and are denoted as dotted lines in the plan view. The x-directed measurement sites are indicated by triangles in the section view.

The air-Earth surface is set to be flat in this example and is at $z = 0$ m. The air layer was assigned the small conductivity value $\sigma = 10^{-8}$ to stabilize the numerical solution. Two perpendicular and horizontal measurement lines that are located at the air-Earth surface are used to examine the numerical solution of MT impedance components, as indicated in Fig 4.4(a). One line is along the x direction and has the coordinates $-4 \leqslant x \leqslant 4$ km and $y = 0$ (line1). The other line is along the y direction and has the coordinates $-4 \leqslant y \leqslant 4$ km and $x = 0$ (line2). To ensure a sufficient approximation of the 1-D boundary condition, the computational domain was set to be $\Omega = \{(x, y, z)| -5 \leqslant x \leqslant 5 \text{ km}, -5 \leqslant y \leqslant 5 \text{ km}, -5 \leqslant z \leqslant 2 \text{ km}\}$.

An unstructured meshfree discretization consisting of $N = 73,630$ points was used to obtain an accurate numerical solution. In this discretization, the points were locally refined both within the conductor (with the average internodal distance $h_s \approx 35$ m) and at the measurement lines ($h_s \geqslant 30$ m) and becomes gradually sparser towards the

computational boundaries. For the PHS RBF-FD method, the stencil size for non-interfacial points is $n = 30$ and quadratic polynomials are enriched for the numerical examples hereinafter, unless otherwise stated. For this discretization, the resulting sparse matrix in the linear system of equations has the dimension of $294,520$ and has $N_{non} = 18,441,072$ non-zero entries. The impedance tensor, $\mathbf{Z}$, was calculated for the two frequencies: 0.1 Hz and 10 Hz, for which the off-diagonal components (Z_{xy} and Z_{yx}) are plotted as apparent resistivity and phase curves in Fig 4.5 and Fig 4.6, respectively (the diagonal components, Z_{xx} and Z_{yy}, have the apparent resistivities of the order of 10^{-5} to 10^{-3} and are not shown here).

It is observed that the meshfree solution agrees well with other mesh-based numerical solutions that include FV, grid-based FD and IE solutions (see Jahandari, 2015; Zhdanov et al., 1997) for each frequency. In order to examine the details of reproducing possible discontinuous EM fields in this example, a horizontal test line within the cross section at $y = 0$ that is perpendicular to the facets of the conductor was used to compute the normal components of the electric field. The test line is shown in Fig 4.7. The electric field is expected to be discontinuous along this line at the intersections with the conductor, since the normal electric field, E_x, with respect to the facets of the conductor in the x-y plane is not continuous. Fig 4.8 shows the semi-log plots of A_x, ψ, $(\nabla\psi)_x$, and E_x $(= -i\omega A_x - (\nabla\psi)_x)$ along the test line. It is observed here that the potentials (A_x and ψ) are indeed continuous across the conductivity jumps, whereas the normal component of the scalar potential, $(\nabla\psi)_x$, and E_x are discontinuous, both of which are physically anticipated. Note that in the plots of ψ, the discontinuities appearing in the curves at $x = 0$ indicate the cut-off positions of positive and negative ψ values, rather than the function's discontinuities.

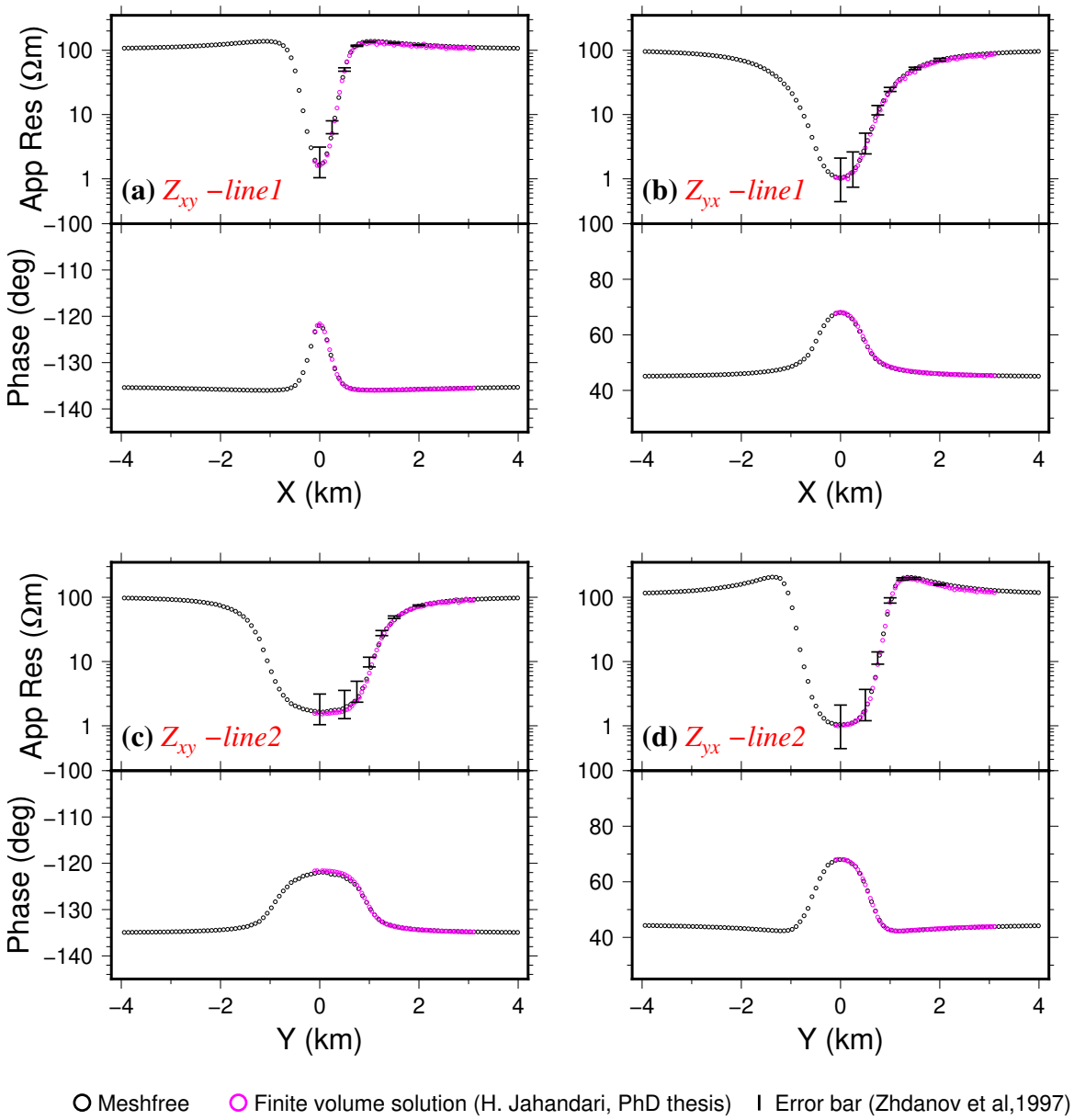

Figure 4.5. Computed impedance components Z_{xy} and Z_{yx} at the frequency of 0.1 Hz for line 1 (panel **a**, **b**) and line 2 (panel **c**, **d**) using the meshfree method, compared with a finite volume solution (Jahandari, 2015) and other mesh-based solutions (error bars, Zhdanov et al., 1997). For each panel, the top shows the apparent resistivity, and the bottom shows the phase curves. The error bars represent the standard deviations and mean values of the numerical results reported in Zhdanov et al. (1997). Only the error bars for apparent resistivity are available.

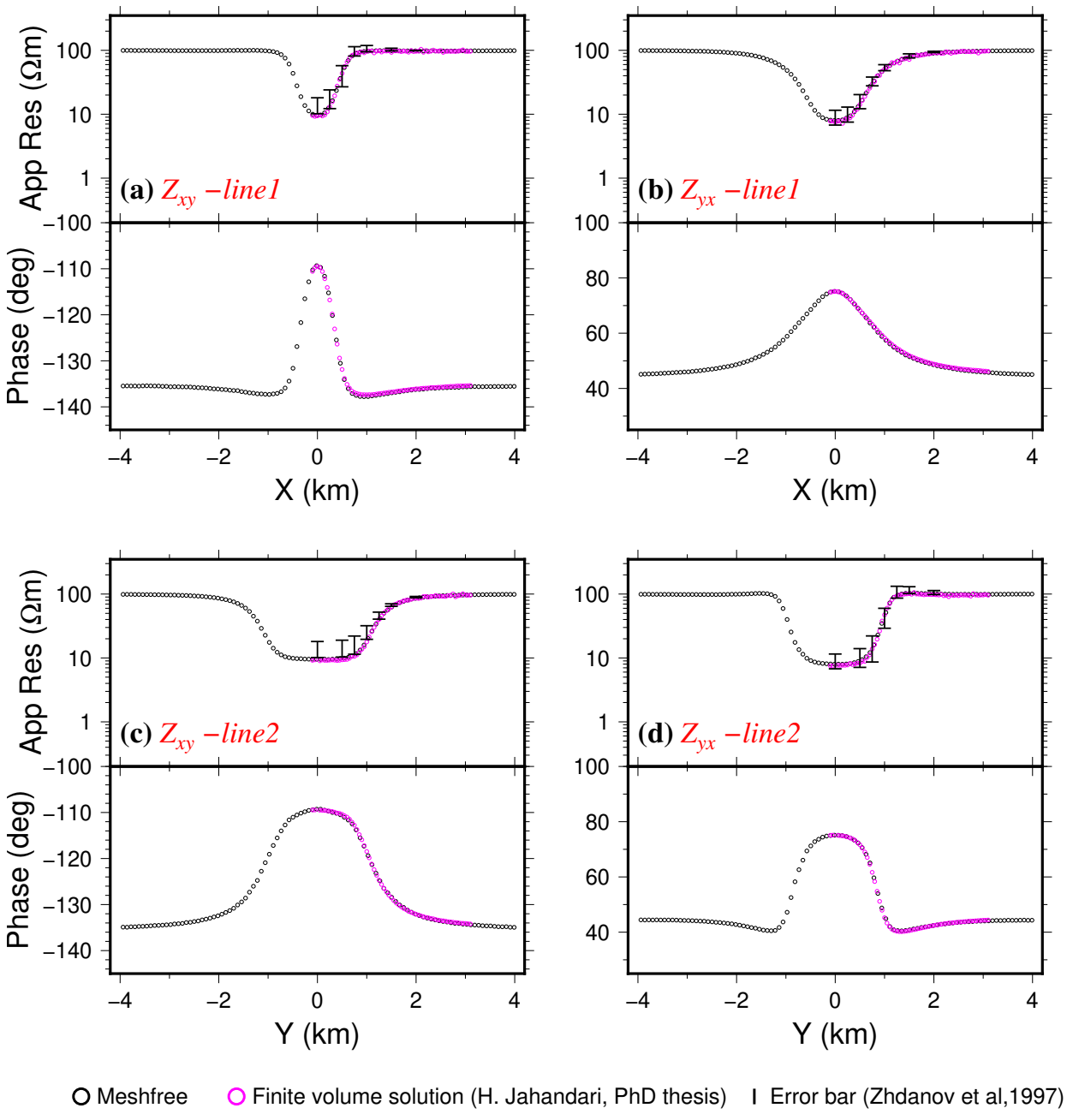

Figure 4.6. The same plots as Fig 4.5, but for the case of 10 Hz.

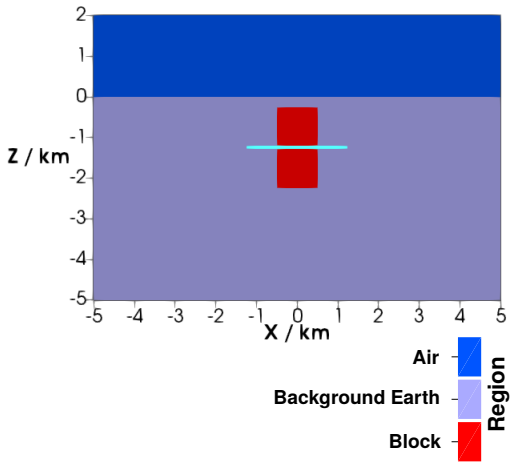

Figure 4.7. A 2-D section view of the COMMEMI 3D-1A model at $y = 0$. The solid cyan line is along the x direction ($-1.2 \leqslant x \leqslant 1.2$ km, $z = -1.25$ km), and intersects the conductive block (in red) at $x = -0.5$ km and $x = 0.5$ km.

The same continuity behaviours of these components are also plotted with the numerical results computed by the standard PHS RBF-FD meshfree method without incorporating the continuity condition (referred to as the continuous version of the RBF-FD meshfree method in the following) for comparison, which are shown in Fig 4.9. It is clearly seen from Fig 4.9 that, while the computed potentials (A_x and ψ) are continuous as expected, the computed $(\nabla\psi)_x$ and E_x are also smooth across the conductivity jumps, which is unphysical and causes the spurious solutions in the calculated MT impedance responses as shown in Fig 4.10. This is because of the intrinsic smoothness of a standard meshfree function approximation, as mentioned before. In addition, due to the forced smoothing effect, the computed potentials in the continuous RBF-FD version deviate from the correct ones when compared to the results in Fig 4.8.

The continuity behaviours are further examined by computing the **E** field in the horizontal plane with $z = -500$ m using the meshfree method. The 2-D vector arrow

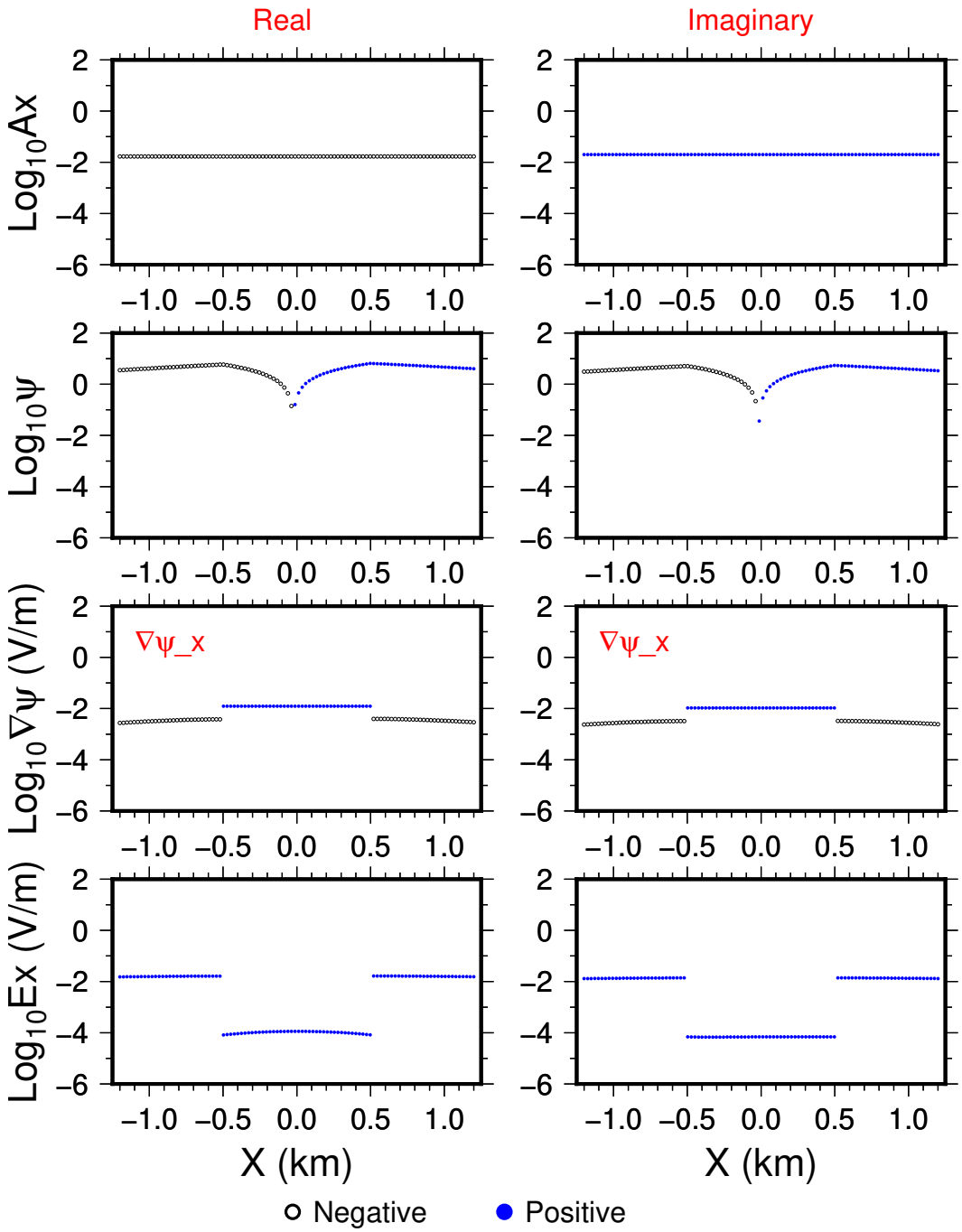

Figure 4.8. Continuity plots of the components A_x, ψ, $(\nabla\psi)_x$ and E_x for the horizontal line shown in Fig 4.7. The left column shows the plots of the real part of the four quantities, and the right column shows the imaginary part of them. The four components were calculated in the E-x polarization mode with $f = 0.1$ Hz using the mixed RBF-FD meshfree method. All values are plotted in the $\log_{10}$ scale. Unfilled black circles indicate that the values are negative, and filled blue circles represent positive values.

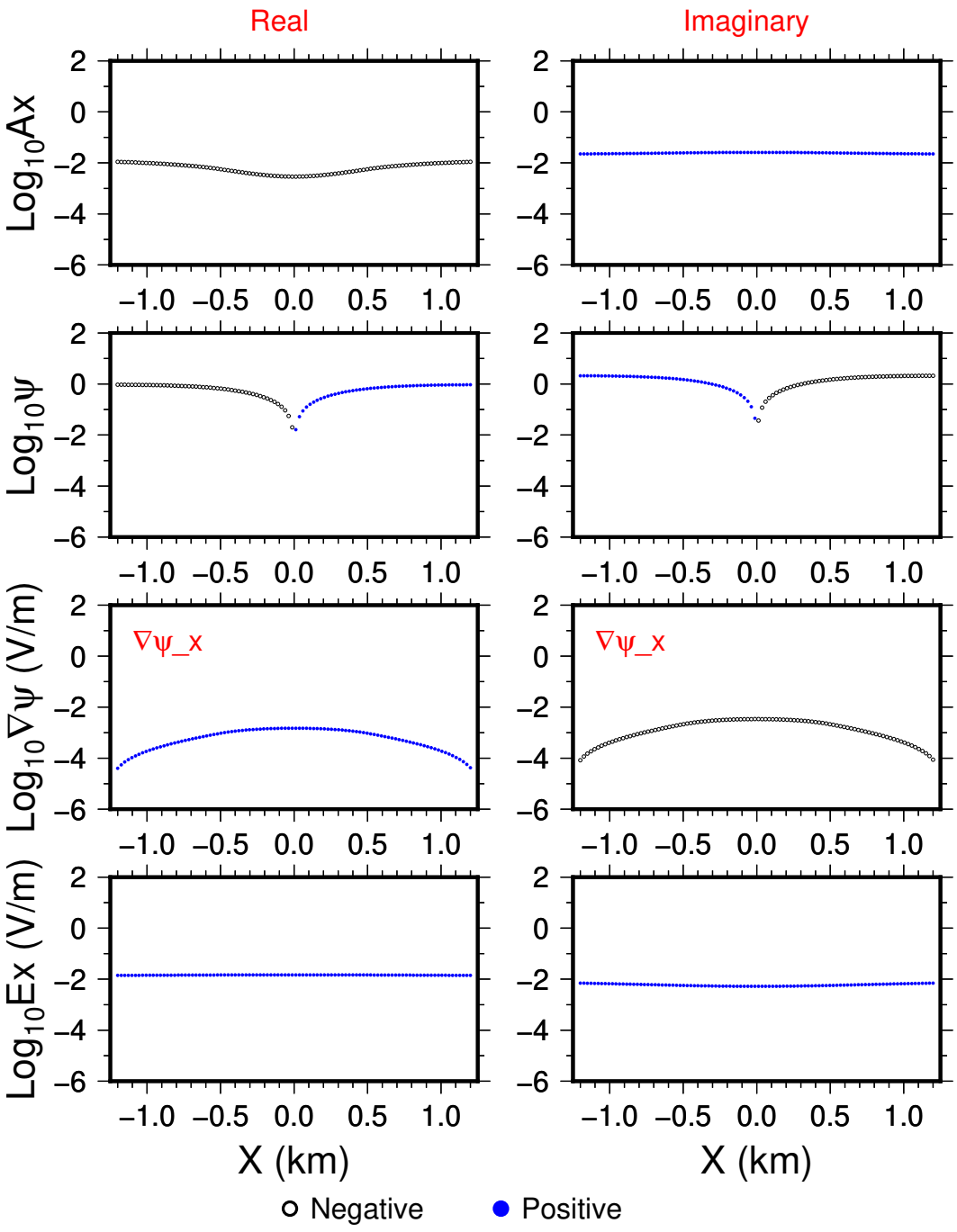

Figure 4.9. The same continuity plots as Fig 4.8 but with the impedance results calculated using the continuous version of the RBF-FD meshfree method.

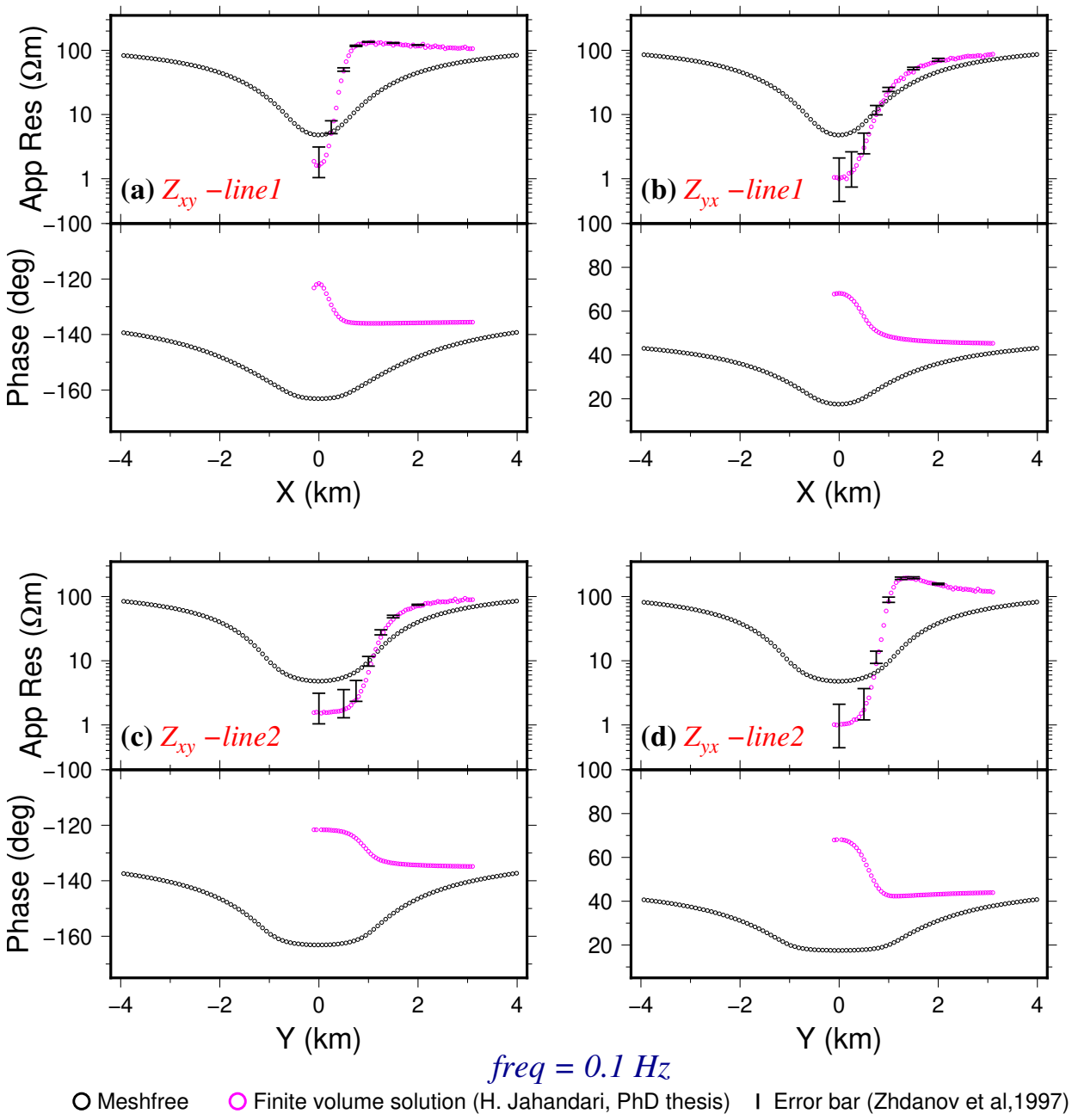

Figure 4.10. The same plots of the off-diagonal impedance components as Fig 4.5 but with the impedance results calculated using the continuous version of the RBF-FD meshfree method.

plots of the electric field are shown in Fig 4.11 and provide a graphical illustration of the overall discontinuity behaviours of $\mathbf{E}$ across the conductivity jumps. In Fig 4.11, the 3-D vector $\mathbf{E}$ fields projected on the 2-D plane ($z = -500$ m) for both source polarization modes at the frequency of 0.1 Hz are displayed. Here, abrupt changes of the magnitude of the normal electric field are clearly observed over the conductivity discontinuities. Also observed are anticipated channelling effects of the electric field along the conductivity contrasts that are parallel to the source electric field ($\mathbf{E}_s$), or the polarization direction. These physical behaviours are, however, not captured in the numerical solution using the continuous version of the RBF-FD meshfree method, as shown in Fig 4.12.

The gauge condition applied to the vector potential, $\nabla \cdot \mathbf{A} = 0$, is implicitly imposed when solving the pair of eqs (4.15) and (4.13). However, $\nabla \cdot \mathbf{A} = 0$ will not be satisfied exactly, but will rather be satisfied approximately in a numerical solution. To demonstrate this, Table 4.2 lists the computed normalized l_2 norm of $\nabla \cdot \mathbf{A}$ for coarse to finer quasi-uniform discretizations (i.e., uniform unstructured points without local refinements throughout the computational domain). The normalized l_2 norm of $\nabla \cdot \mathbf{A}$ is computed by firstly calculating the values of $\nabla \cdot \mathbf{A}$ at each point of the meshfree discretization. Then the square sum of the resulting vector values is normalized in the square root:

$$||\nabla \cdot \mathbf{A}||_2 = \sqrt{\frac{1}{N}\sum_{j=1}^{N}(\nabla \cdot \mathbf{A})_j^2}, \tag{4.31}$$

where N is the total number of points. It is seen in Table 4.2 that for both frequencies (0.1 Hz and 10 Hz) considered here, $||\nabla \cdot \mathbf{A}||_2$ has mostly the order of magnitude of

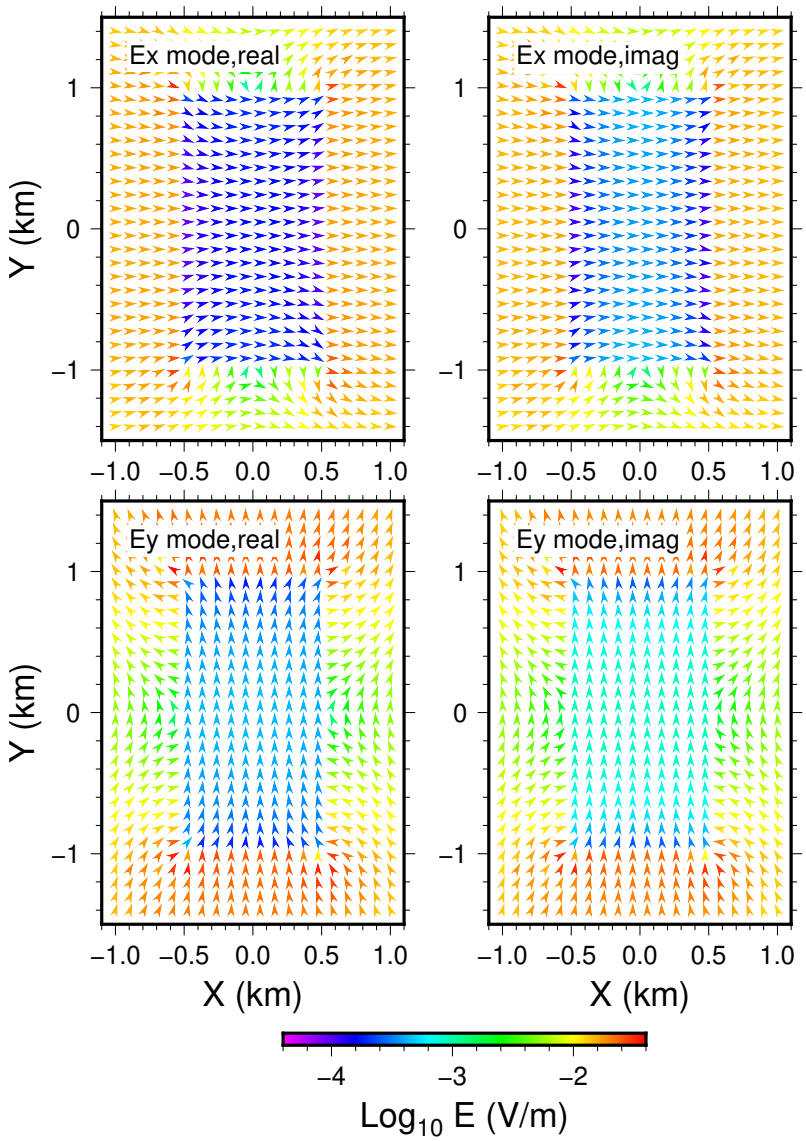

Figure 4.11. 2-D vector arrow plots of the **E** field in the horizontal plane $z = -500$ m for the COMMEMI 3D-1A model. The results were calculated using the mixed RBF-FD meshfree method for the frequency $f = 0.1$ Hz (the plots for $f = 10$ Hz are similar). The "Ex mode" in the labels means the external electric field of the MT source is parallel to the x direction (i.e., E-x polarization), and "Ey mode" means the E-y polarization mode. Both real (denoted by "real") and imaginary (denoted by "imag") parts of the field are shown here. The magnitude of the **E** field is indicated by the colour bar.

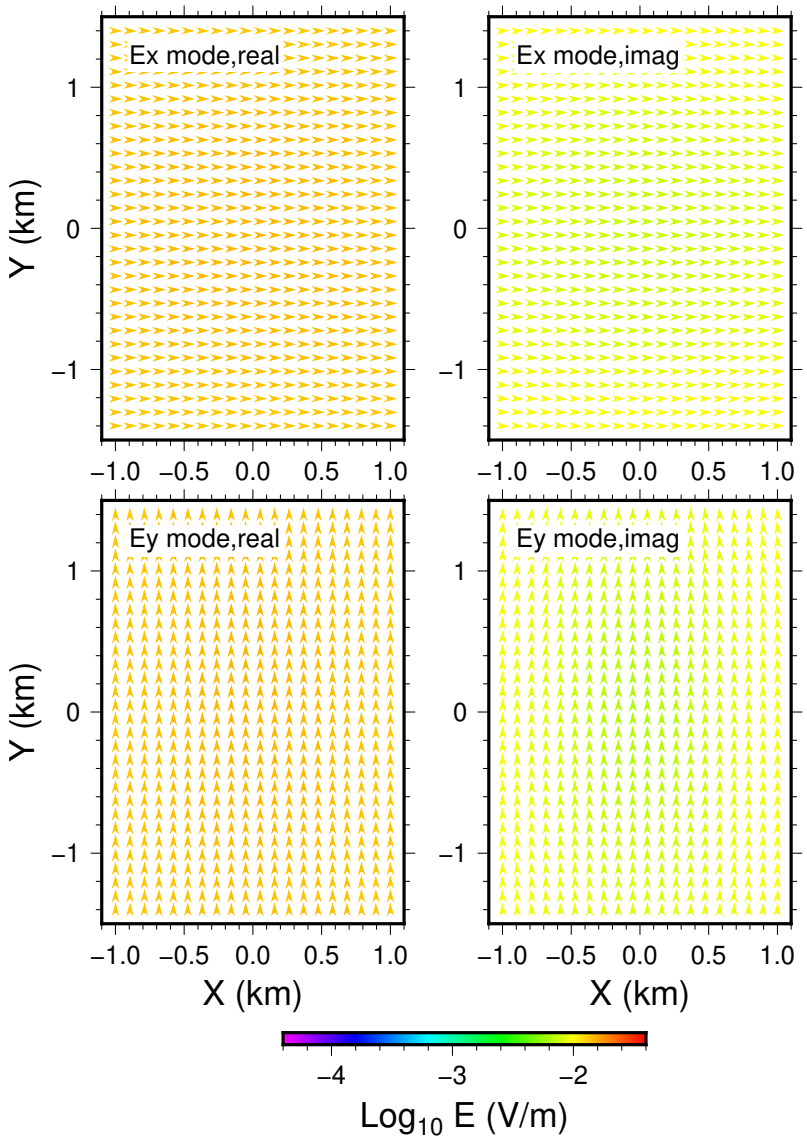

Figure 4.12. The same 2-D vector arrow plots as Fig 4.11 but with the results calculated using the continuous version of the RBF-FD meshfree method.

10^{-9} to 10^{-8}. These values are numerically zero, especially when they are compared with the values of $\nabla \cdot (\nabla \psi)$ (see the following discussion). Note that by increasing the density of points from a very coarse discretization (1st) to a very fine discretization (5th), the order of magnitude and the overall pattern of changes of $||\nabla \cdot \mathbf{A}||_2$ are not significantly affected, although using a finer discretization improves the numerical accuracy. This confirms the effectiveness of the boundary conditions in fulfilling the gauge condition. The numerical solution of the impedance using the discretization with $58,044$ points in total in Table 4.2 is comparable to that shown in Fig 4.5 (see Appendix D for plots). But the computed impedance has obvious fluctuations when the total number of points is reduced to $7,414$ (Appendix D). The similar accuracy difference can also be observed in the calculated $\nabla \cdot \mathbf{A}$ using these two discretizations. Fig 4.13 and Fig 4.14 show plots of $\nabla \cdot \mathbf{A}$, $\nabla \cdot (i\omega \mathbf{A})$ and $\nabla \cdot (\nabla \psi)$ in the horizontal plane $z = -500$ m, which cuts through the conductor in the background half space, for the two frequencies of 0.1 Hz and 10 Hz, respectively. It is observed that the use of the finer discretization clearly enhances the numerical accuracies. Another observation here is that the divergence of $\mathbf{A}$ has uniform values, although subject to numerical errors, within the computational domain which are small as predicted by the gauge condition. The comparison between $\nabla \cdot (i\omega \mathbf{A})$ and $\nabla \cdot (\nabla \psi)$ shows that the main contribution to $\nabla \cdot \mathbf{E} = \nabla \cdot (-i\omega \mathbf{A} - \nabla \psi)$ comes from $\nabla \cdot (\nabla \psi)$ at the conductivity jumps (i.e., the interface between the conductor and the background earth here). This is due to the build up of charges at the conductivity jumps.

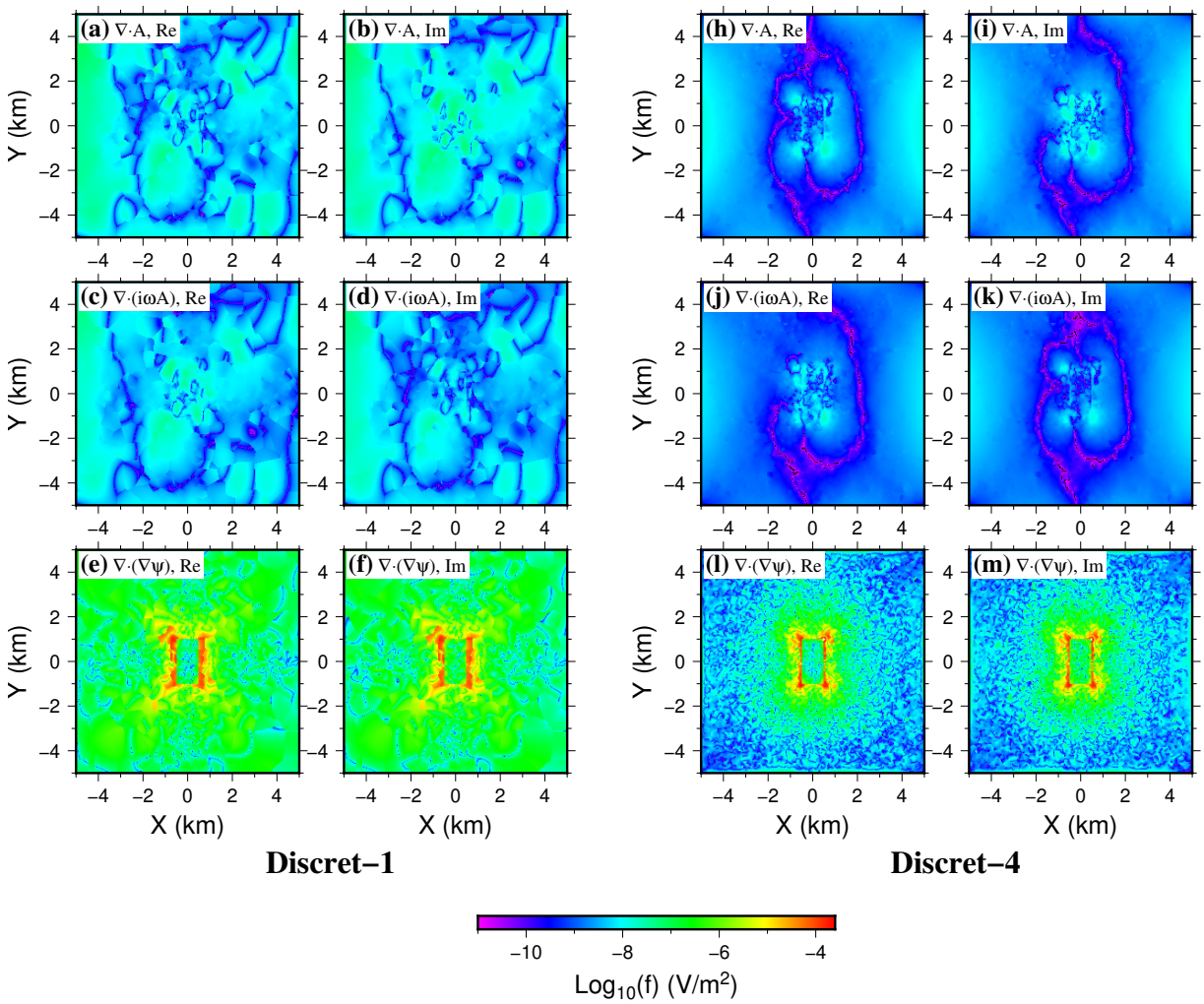

Figure 4.13. Coloured images of computed $\nabla \cdot \mathbf{A}$, $\nabla \cdot (i\omega\mathbf{A})$ and $\nabla \cdot (\nabla\psi)$ in the horizontal plane $z = -500$ m for the COMMEMI 3D-1A model. The frequency is 0.1 Hz. The source polarization mode is E-x polarization (the results for the E_y polarization mode are similar). Panels **(a)-(f)** show the divergence results using the first discretization in Table 4.2 (hence 'Discret-1') with 7,414 points. Similarly, panels **(h)-(m)** show the results using the 4th discretization in Table 4.2 ('Discret-4') with 58,044 points. The magnitudes of the values are indicated by the colour bar. The highest value in the colour bar is -3.6.

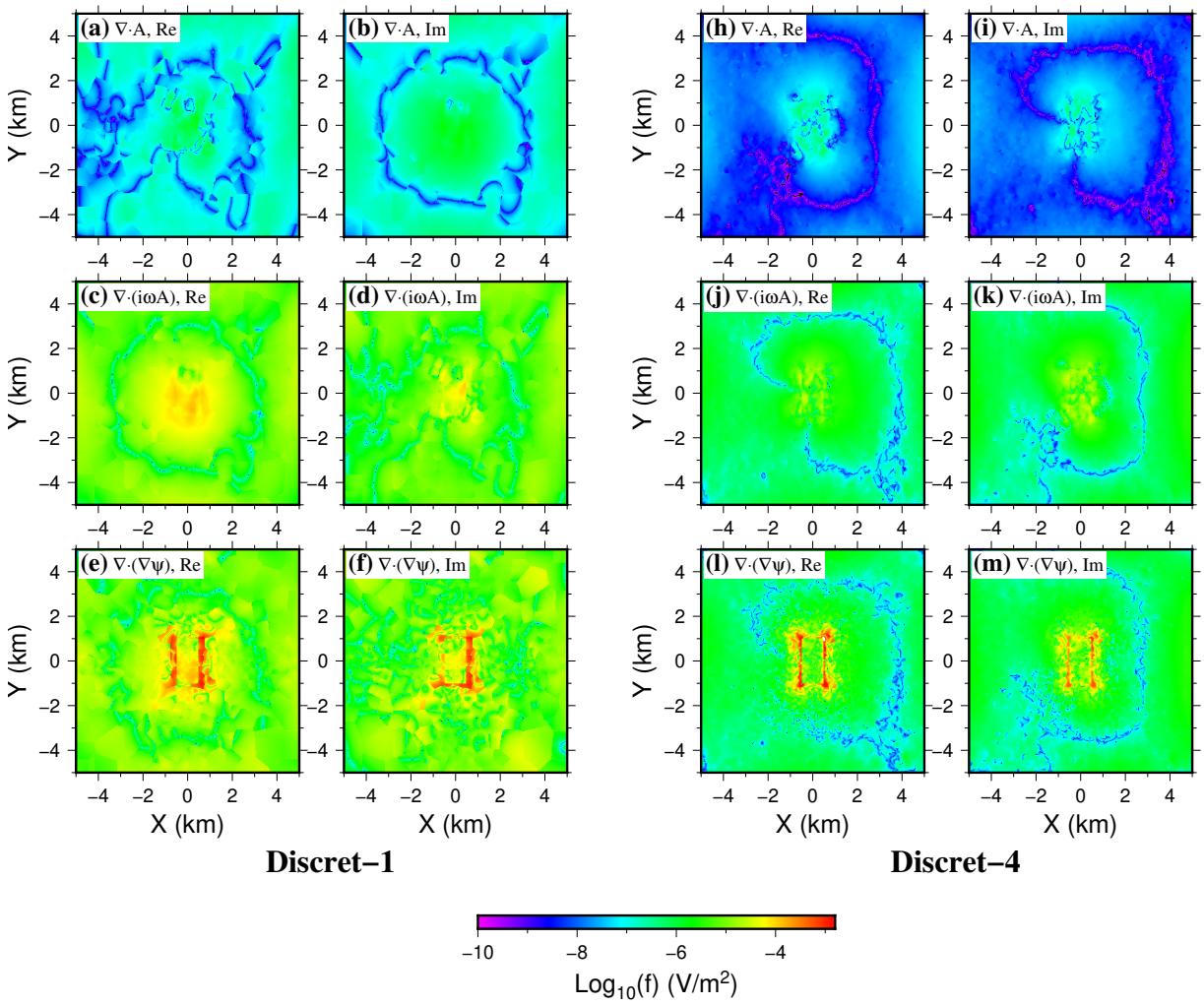

Figure 4.14. The same coloured image plots as in Fig 4.13, but for the frequency of 10 Hz. The highest value in the colour bar is -2.8.

Table 4.2. Calculated values (complex numbers) of normalized $||\nabla \cdot \mathbf{A}||_2$ with different discretizations. The mode is E-x polarization. The results are for the two frequencies: 0.1 Hz and 10 Hz, respectively.

Discretization	Total number of points	$\|\|\nabla \cdot \mathbf{A}\|\|_2$			
		$f = 0.1$ Hz		$f = 10.0$ Hz	
1	7414	9.1773e-9	1.4605e-8	4.3377e-7	9.4274e-7
2	20 311	3.0622e-9	3.8686e-9	7.9899e-8	1.1412e-7
3	31 049	3.3176e-9	3.6113e-9	1.1036e-7	7.3346e-8
4	58 044	3.3007e-9	3.2470e-9	4.0938e-8	5.6948e-8
5	123 768	3.1723e-9	2.9054e-9	3.0538e-8	2.6884e-8

4.4.2 COMMEMI model 3D-2A

In this example, the conductivity model is the COMMEMI 3D-2A model (Zhdanov et al., 1997), which is more complicated than the 3D-1A model. The 3-D model has 4 different conductivity layers along the depth (including the air layer). A diagram of the model is shown in Fig 4.15. The three layers in the subsurface from top to bottom have the conductivities 0.1 S/m, 0.01 S/m and 10 S/m, respectively. In the very top layer, there is one embedded conductor (conductivity $\sigma = 1$ S/m) having the dimension of $-20 \leqslant x \leqslant 0$ km, $-20 \leqslant y \leqslant 20$ km and $-10 \leqslant z \leqslant 0$ km. A rectangular resistive intrusion from the second subsurface layer having the same extents as the conductor is also located in the first layer and is adjacent to the conductor, as shown in Fig 4.15. The main task in this example is to simulate the MT impedance in the presence of strong effects of shallow inhomogeneities.

For the numerical tests, three EM frequencies are used: 0.1, 0.01 and 0.001 Hz. The computational domain was set to be $\Omega = \{(x, y, z)| -80 \leqslant x \leqslant 80 \text{ km}, -80 \leqslant y \leqslant 80 \text{ km}, -120 \leqslant z \leqslant 30 \text{ km}\}$. A measurement line ($y = 0$, $-60 \leqslant x \leqslant 60$ km)

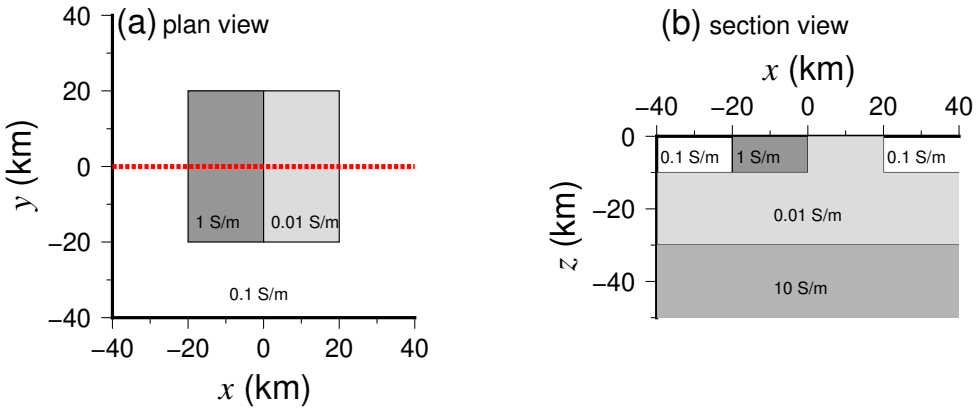

Figure 4.15. Plan (a) and section (b) views of the COMMEMI 3D-2A conductivity model. The subsurface ($z < 0$) has three layers with different conductivities as shown in the panel (b). In the first layer (the top layer, $\sigma = 0.1$ S/m), there are one rectangular conductor ($\sigma = 1$ S/m) and one intrusion block from the second more resistive layer ($\sigma = 0.01$ S/m). The red dotted line at $y = 0$ (plan view panel) represents the measurement sites at the air-Earth surface ($z = 0$) used to calculate the MT response for the model.

with 100 synthetic measurement sites, which is shown in Fig 4.15(a), was designed to compare the meshfree solutions to other numerical solutions. A point discretization with the total number $N = 96,637$ was used to compute the impedance for all three frequencies. In this discretization, the conductor and the intrusion part in the first layer were refined with $h_s \approx 1.25$ km. The measurement sites were refined with $h_s \geqslant 300$ m. A perspective 3-D view of the point discretization is shown in Fig 4.16.

The computed off-diagonals of the impedance tensor are plotted in Figs 4.17, 4.18 and 4.19 for the three frequencies 0.1 Hz, 0.01 Hz and 0.001 Hz, respectively. It is shown that the meshfree solution agrees well with other independent mesh-based solutions for each of the three frequencies. The linear system of equations for this discretization has the dimension of $386,548$ and the number of non-zeros as $23,839,450$. The peak memory storage used for each frequency was about 33.2 GB.

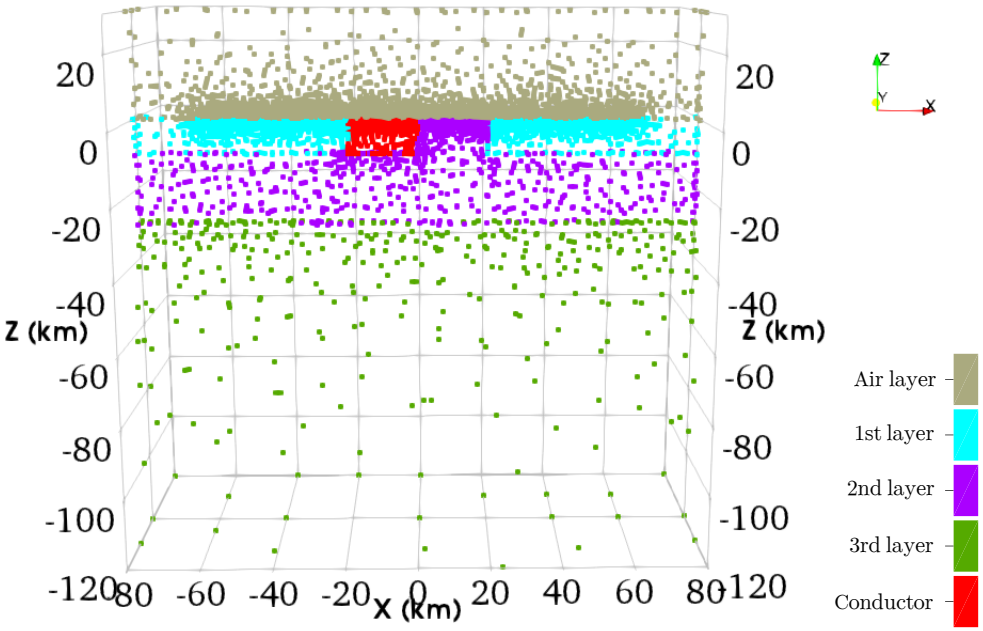

Figure 4.16. A 3-D perspective view of the meshfree point discretization of the COMMEMI 3D-2A model. The points are within the domain $\Omega = \{(x, y, z) | -80 \leqslant x \leqslant 80 \text{ km}, -5 \leqslant y \leqslant 5 \text{ km}, -120 \leqslant z \leqslant 30 \text{ km}\}$.

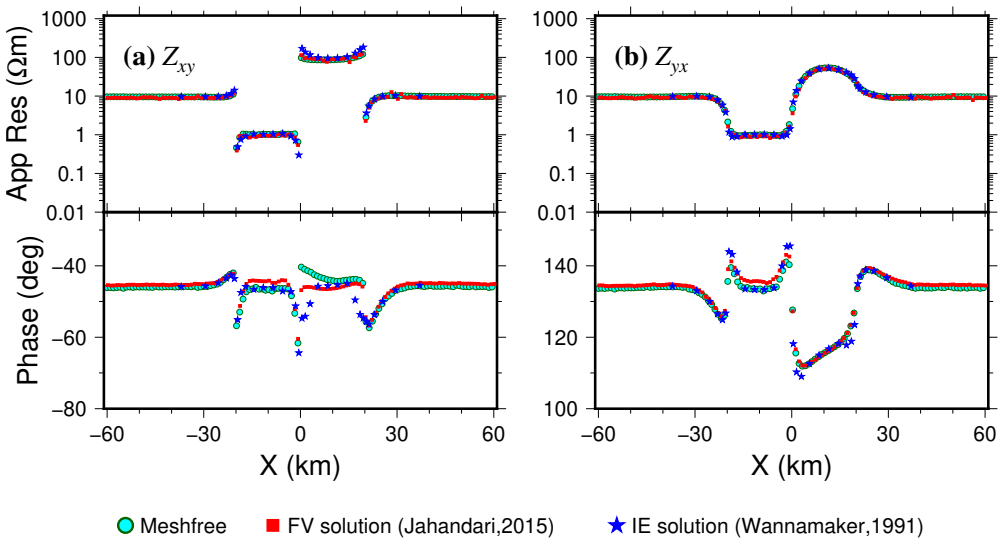

Figure 4.17. Computed Z_{xy} (panel **a**) and Z_{yx} (panel **b**) components of the impedance tensor for the COMMEMI model 3D-2A using the hybrid meshfree method. The frequency is $f = 0.1$ Hz. Also plotted are a FV solution (Jahandari, 2015) and an IE solution (Wannamaker, 1991) for comparison.

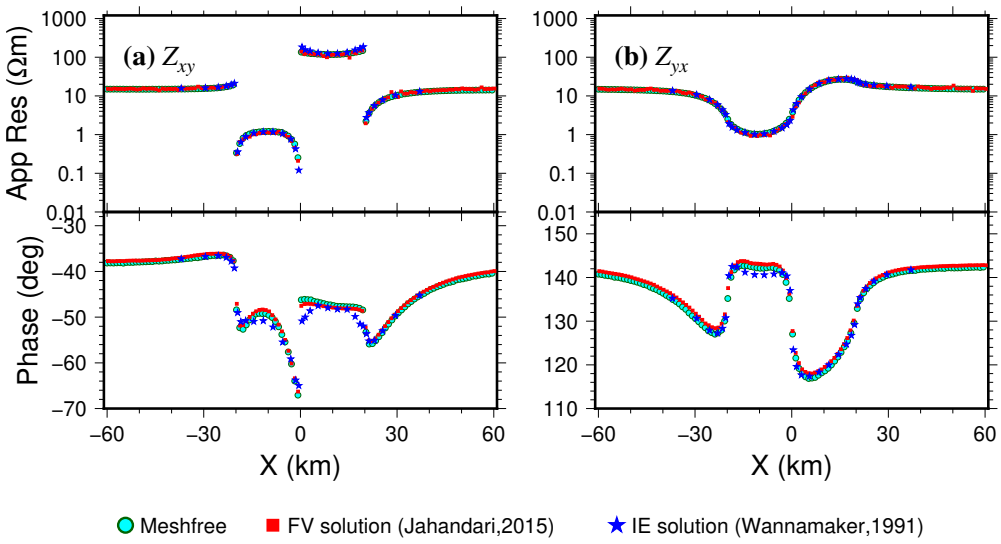

Figure 4.18. The same plots as in Fig 4.17, but for the case of $f = 0.01$ Hz.

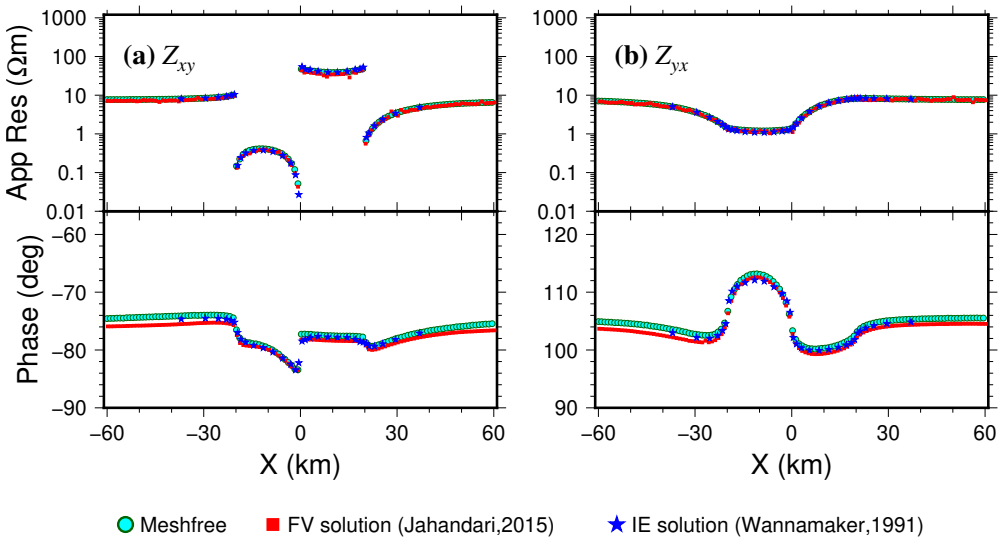

Figure 4.19. The same plots as in Fig 4.17, but for the case of $f = 0.001$ Hz.

4.4.3 Dublin Test model-1

The third example for the MT data modelling is the Dublin test model 1 (DTM-1) from the comparison study of Miensopust et al. (2013). The model has large conductivity contrasts among its three rectangular prisms embedded in the subsurface ($\sigma_b = 0.01$ S/m). The geometries, resistivities and dimensions of the prisms, as well as the locations of synthetic measurement sites, are illustrated in Fig 4.20. Additionally, 3-D perspective views of the model are shown in Fig 4.21 (panels a and b). For this example, 59 MT sites evenly distributed along the four measurement lines (Fig 4.20) were originally designed to compare modelling results from various codes/algorithms, as reported by Miensopust et al.. A total number of 21 frequencies that are logarithmically equispaced in the range of $f \in [10^{-4}, 10]$ Hz (i.e, the period range $T \in [0.1, 10000]$ seconds) are used for calculating the MT impedance responses.

For the hybrid meshfree solutions, the computational domain was set to be $\Omega = \{(x, y, z) | -40 \leqslant x \leqslant 40 \text{ km}, -40 \leqslant y \leqslant 40 \text{ km}, -60 \leqslant z \leqslant 20 \text{ km}\}$. A single meshfree point discretization of the model was used for all frequencies. The discretization, as shown in Fig 4.21(c), has $N = 120,598$ points in total, of which $1,428$ points are on the domain's boundaries. The points around the measurement sites were refined with $h_s \geqslant 300$ m, and the three prisms were appropriately refined ($h_s \approx 1.4$ km) to ensure an accurate solution. This generates a linear system of equations with the dimension of $482,392$ and the number of nonzeros as $31,060,412$.

The computed impedance responses at the origin site for the 21 frequencies are plotted in Fig 4.22. Also shown here are a number of other mesh-based solutions from Miensopust et al. (2013). It is observed that for this particular discretization, which

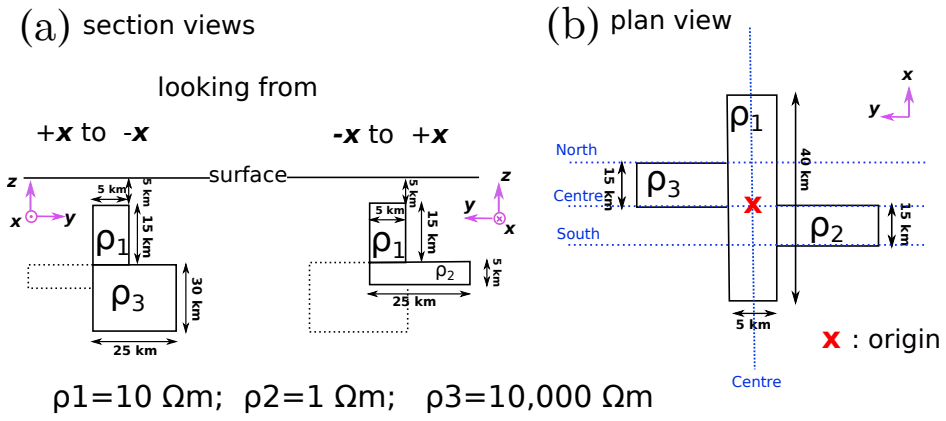

Figure 4.20. Section (a) and plan (b) views of the Dublin Test Model 1 (DTM-1). There are three rectangular prisms attached together in the subsurface with different resistivities (ρ_1, ρ_2, ρ_3) as shown above. The background subsurface has the conductivity of $\sigma_b = 0.01$ S/m ($\rho_b = 100$ Ωm). The origin of the coordinate system is at the surface and marked as the red X in the plan view. The four blue dotted lines in the plan view are the designed measurement lines at the air-Earth surface.

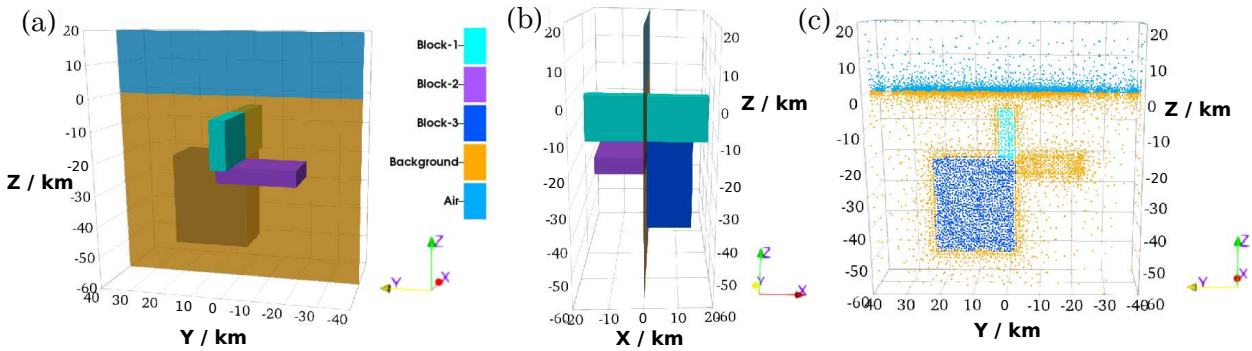

Figure 4.21. Perspective 3-D views of the DTM-1 model at the section $x = 0$. Panels (a) and (b) show the plane of the cross section and the three blocky targets at two different angles. Panel (c) shows the meshfree point discretization ($-10 \leqslant x \leqslant 10$ km) that was used in the meshfree calculation. The air-Earth surface is at $z = 0$.

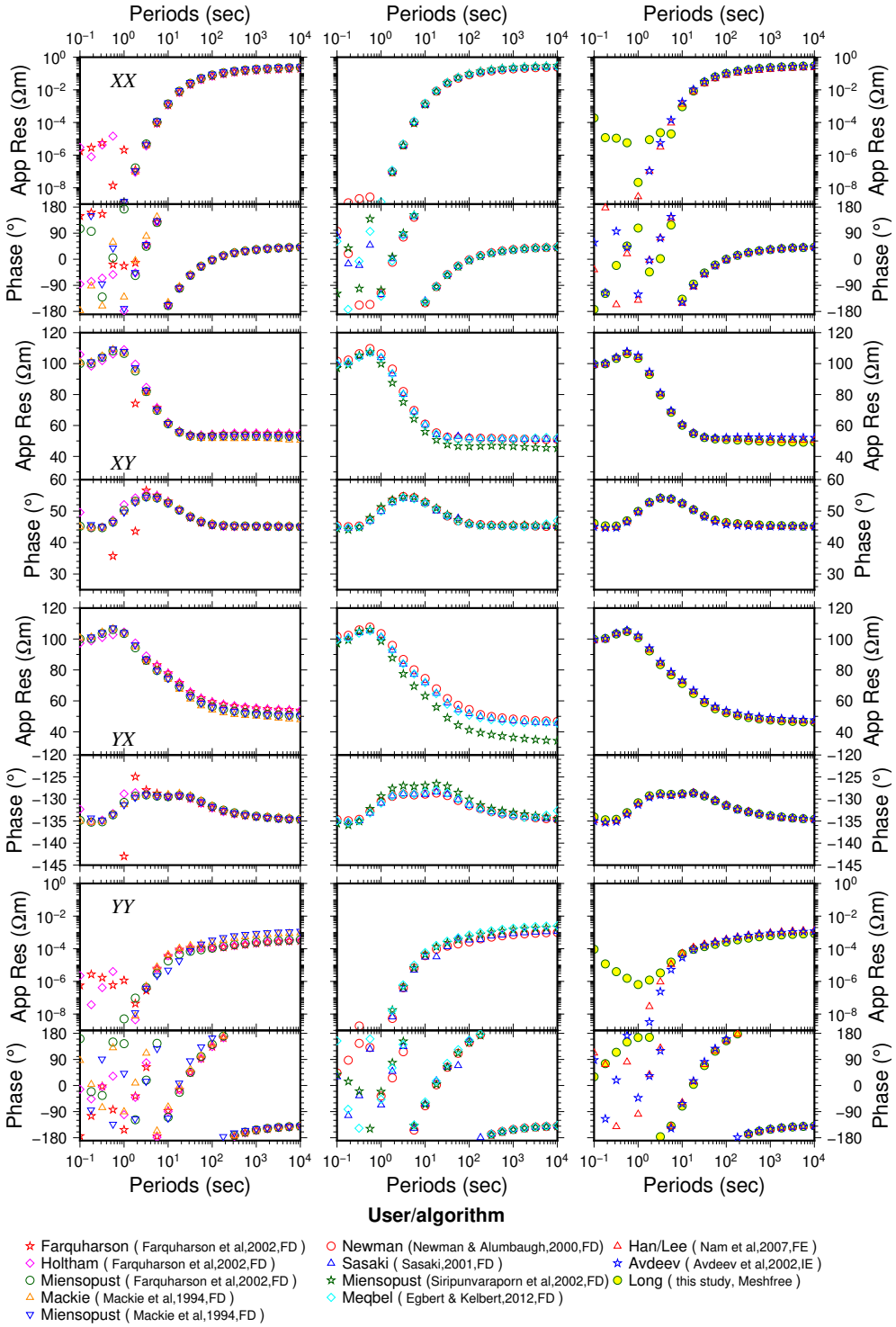

Figure 4.22. Computed meshfree results of impedance components compared with various other numerical solutions (Miensopust et al., 2013) for the period range $T \in [0.1, 10000]$ sec at the origin site (see Fig 4.20) for the DTM-1 model. The first column of the curves shows the solutions corresponding to the first column of the User/algorithm list at the bottom; the same corresponding relation also applies to the second and third columns of the curves.

has a moderate number of degrees of freedom compared to those of other numerical solutions, the meshfree solution has a good agreement with other solutions for all impedance components. The deviations in the solution of diagonal components (Z_{xx} and Z_{yy}) for high frequencies ($f > 0.1$ Hz) are due to insufficient point discretization in the shallow part of the subsurface, where the EM fields are expected to change more rapidly than those of lower frequencies.

The peak memory usage for this example is about 47 GB. With the employed computer resource (16-core Intel Xeon E5-2670 CPU with 2.6 GHz), the running time of the computation for all 21-frequency MT responses is listed in Table 4.3. The majority of computation is that of assembling and solving the linear system of equations. It is noted that for the first frequency, the computation time is approximately 1 min longer than that of all subsequent frequencies. This is because of the need to calculate RBF-FD weights and FE weights in the assembling, which is only required once for the same discretization. The formation of the coefficient matrix of the linear system of equations for subsequent frequencies can be done by simply modifying the frequency value in eq (4.21). The difference between the assembling time and solving time, as shown in Table 4.3, suggests that the most computationally expensive part in the meshfree method is the matrix equation solving process for moderate- to large-scale discretizations of models, which is typically observed in more traditional mesh-based methods.

Table 4.3. Computation time for the DTM-1 MT model. The computation running time includes the time amount of assembling and of solving the linear system of equations.

No. of frequency	**Computation time**
1st frequency	14 mins 18 s
the remaining 20 frequencies	4 hrs 25 mins 55 s (in average 13 min 17.7 s for each frequency)

4.5 Chapter summary

The PHS RBF-FD meshfree method incorporated with a Galerkin weak form approach to solve the difficulty of faithfully modelling possible function discontinuities is applied to simulate MT impedance data. The discontinuity issue is faced by standard meshfree numerical methods because standard meshfree function approximants are high order continuous. The numerical examples here show that the proposed discontinuity treatment is effective in reproducing possible discontinuities in the electric field over conductivity jumps or at the interfaces of high conductivity contrasts. The discontinuity treatments are not needed if the function of interest in a PDE is globally smooth or high-order continuous, of which some examples in the case of geophysical EM method are: 2-D MT data modelling regardless of the conductivity distribution, 3-D EM field simulation for a continuously changing or constant conductivity model, etc. In the case of continuously changing conductivity distribution, for example a smooth model constructed from a minimum structure style inversion, $\nabla\sigma$ is not zero and will be present in the governing EM potential equation (eq 4.19), and a standard meshfree implementation without the discontinuity treatments will suffice to accurately model the EM field.

Chapter 5

Simulation of controlled-source EM data using PHS RBF-FD

5.1 Introduction

In the frequency-domain controlled-source EM (CSEM) survey method, the EM source signals are man-made EM fields energized from EM transmitters. In practice, an EM transmitter can be a finite-length grounded wire source, or a loop wire source that is not grounded. In either case, the source carries an alternating electric current that generates the EM fields in the ground.

For numerically modelling the CSEM responses over a conductivity model, the same quasi-static (i.e, neglecting the displacement current term) Maxwell's equations described in the MT case are used. The only addition is that now the source terms are not zero. Therefore, the Coulomb gauged $\mathbf{A}$-ψ scheme is used in this chapter and is discretized the same way as in the MT case to forward model CSEM data.

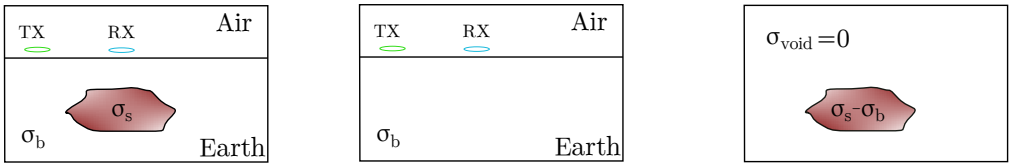

(a) Original model (b) 1-D background model (c) Anomalous model

Figure 5.1. Schematic illustration of the model separation in a primary-secondary field approach: (**a**) an original inhomogeneous conductivity model with EM transmitter (TX) and receiver (RX), (**b**) a 1-D half space model that is chosen as the background model and (**c**) the anomalous conductivity distribution in which $\sigma_{anomaly} = \sigma_{original} - \sigma_{background}$ as a result of the choice of the background model. The anomalous conductivity distribution acts as the source term when numerically solving for the scattered secondary EM field (see details in Appendix E)

The EM source functions are singular current density functions in a mathematical sense. Physically, this means that the total EM field in the frequency domain exhibits singularities or discontinuities at the places occupied by the wire sources. Although such singularities do not affect any real-life EM data measurements, since the measurement sites are never coincident with the source wire, they do pose a difficulty in numerically modelling the EM field. The difficulty is due to the non-trivial effort in accurately approximating the rapidly changing EM field near the source and the singular EM field at the source, as the function approximation in most numerical PDE-solving methods can only handle finite-valued functions.

A commonly used approach to tackle the above singularity issue in numerical methods is to separate the EM field into a primary part and a secondary part (called primary-secondary field approach, e.g., Coggon, 1971; Alumbaugh et al., 1996; Weiss & Constable, 2006; Streich, 2009; Puzyrev et al., 2013). The primary part is the EM field due to a controlled source over some simple background model (such as

1-D layered models), and the secondary part is called scattered EM field which is the difference between the total EM field for the original 3-D inhomogeneous model and the primary EM field for the background model. In this way, only the secondary EM field, which has no singularity, needs to be numerically solved. The primary field still has singularities at the source but now can be sought by analytical or semi-analytical ways because of the very ideal background conductivity distribution (Ward & Hohmann, 1988). Using the primary-secondary field approach, if the EM source is located outside the conductivity anomalies (i.e., the difference between the 3-D original conductivity distribution and the 1-D counterpart, see Fig 5.1), the scattered secondary field will be smoother than the total field near the source, thus circumventing the source singularity issue. However, if the EM source is located within the interested conductivity anomalies, the singularity issue cannot be avoided. Note that the 3-D anomalous conductivity distribution can also be complex, depending on the choice of the background conductivity model. Complex anomalous conductivity distributions appear when the original 3-D conductivity model is very different from the 1-D background model, such as a marine conductivity model with bathymetry. One disadvantage of the primary-secondary approach is that analytical solutions may not be available, resulting in non-trivial efforts in calculating the primary EM field. This can be due to either practical EM sources being used (e.g., arbitrarily shaped loop sources) or a lack of 1-D idealized background models (e.g., when the EM source resides on uneven topography or bathymetry).

The total-field approach incorporates the source terms in the mathematical equations and solves directly for the total field (Ansari & Farquharson, 2014; Jahandari & Farquharson, 2014). In the total-field approach, the source can be positioned wherever

it is needed for practical survey scenarios, making the approach more straightforward and more general than the primary-secondary field approach. The main challenge in the total-field approach lies in the proper approximation of the numerical singularity of source functions, resulting in a need of distributing small cells or elements in a 3-D mesh around the EM source in order to ensure numerical accuracy as well as efficiency. Generation of such non-uniform meshes nowadays can be accomplished more easily than it was done in the past (e.g., a decade ago) by adopting third-party open-source mesh generating software (e.g., Fabri et al., 2000; Si, 2015). Both primary-secondary and total-field approaches in the frame of PHS RBF-FD hybrid meshfree method are investigated here.

5.2 A-ψ potential equations with source terms

The same **A**-ψ equations described in Section 4.2.1 are used for modelling CSEM data with either electric type (electric dipole, finite-length grounded wires) or magnetic type (magnetic dipole, loop wires) EM sources. They are written with the source current terms as

$$-\nabla^2\mathbf{A} + i\omega\mu\sigma\mathbf{A} + \sigma\mu\nabla\psi = \mu\mathbf{J}_s + \nabla\times\mathbf{M}_s, \tag{5.1}$$

$$\nabla\cdot(i\omega\mu\sigma\mathbf{A} + \sigma\mu\nabla\psi) = \nabla\cdot(\mu\mathbf{J}_s), \tag{5.2}$$

where $\mathbf{J}_s$ is the electric source current density, and $\mathbf{M}_s$ is magnetic source induction vector (magnetic moment vector) which satisfies $\nabla\cdot\mathbf{M}_s = 0$. For a grounded wire source or a loop source, only $\mathbf{J}_s$ is present and $\mathbf{M}_s$ vanishes (for loop sources, $\nabla\cdot\mathbf{J}_s$

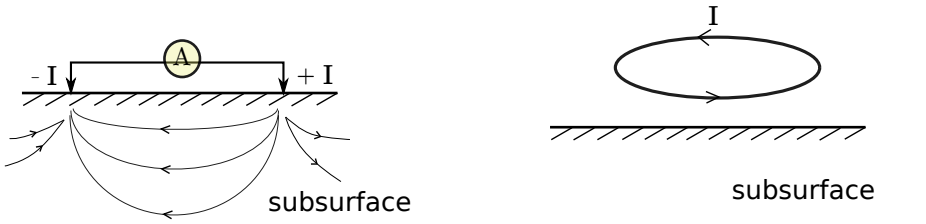

(**a**) Horizontal electric dipole (**b**) Horizontal magnetic loop

Figure 5.2. A diagram illustrating (**a**) a horizontal electric dipole source (the induced electric currents in the subsurface are represented as thin lines with arrow) and (**b**) a magnetic loop source.

also vanishes). For a magnetic dipole source, only $\mathbf{M}_s$ is present and $\mathbf{J}_s$ and its divergence would vanish. The spatial discretization of the eqs (5.1) and (5.2) is the same as that for the MT case, but now the source terms need to be incorporated into the discretization as well.

5.3 Treatment of EM sources

The current density of an electric grounded wire source is a singular function. In the case of a horizontal electric dipole that injects a time-varying current into the subsurface (Fig 5.2) and that aligns with x direction, the current density $\mathbf{J}_s$ can be mathematically represented as (Ward & Hohmann, 1988)

$$\mathbf{J}_s = I_0 \left[\mathcal{H}(x - x_1) - \mathcal{H}(x - x_2)\right] \delta(y - y_0)\delta(z - z_0)\mathbf{u}_x, \tag{5.3}$$

where I_0 is the current intensity, $\mathcal{H}(x)$ is Heaviside function, $|x_2 - x_1|$ is the length of the source wire, $\mathbf{u}_x$ is the unit vector along $+x$ direction, and δ is the Dirac delta

function, which is singular. The divergence of $\mathbf{J}_s$ is given as

$$\nabla \cdot \mathbf{J}_s = I_0[\delta(x - x_1) - \delta(x - x_2)]\delta(y - y_0)\delta(z - z_0) = I_0\delta(\mathbf{r} - \mathbf{r}_1) - I_0\delta(\mathbf{r} - \mathbf{r}_2), \quad (5.4)$$

where $\mathbf{r}_1$ and $\mathbf{r}_2$ are the two points of the injections. It is seen here that the singularity of $\mathbf{J}_s$ occurs in the directions perpendicular to the source line, and the singularity in $\nabla \cdot \mathbf{J}_s$ is point-based.

In discretizing eqs (5.1) and (5.2) using the RBF-FD meshfree method, large errors near the source in a numerical solution can occur if $\mathbf{J}_s$ and $\nabla \cdot \mathbf{J}_s$ are not approximated with an adequate accuracy (Long & Farquharson, 2017). On the other hand, it is anticipated by physics that the EM fields due to an electric source exhibit discontinuities at the two ends of the source wire where the current is injected into the subsurface, which poses a difficulty for a standard meshfree technique such as that investigated in the previous chapter of MT data simulation.

The field discontinuity at the EM source (mainly electric types) is different from the field discontinuity incurred by abrupt conductivity variations. In the former, the electric field at the two ends of a grounded wire source exhibits a point-based discontinuity of singularity in space (Fig 5.3a), while in the latter the field discontinuity only occurs in the normal direction for the conductivity interfaces (Fig 5.3b) in a quasi-static regime.

Based on these observations, a variation of the FE weak-form treatment for conductivity interfaces is proposed to handle the discretization of source terms in the total-field hybrid meshfree RBF-FD approach. This is in addition to the Galerkin FE treatment applied to any interfacial points in the conductivity model. The imple-

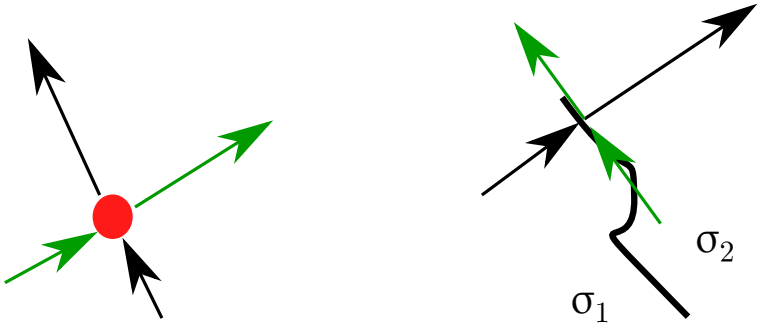

(a) Discontinuous **E** at an end of electric dipole source

(b) Discontinuous **E** at a conductivity interface

Figure 5.3. Different situations of **E** field discontinuity: (**a**) **E** is discontinuous at the ends of an electric dipole source in all directions and (**b**) **E** is discontinuous in the normal direction at the conductivity interfaces but continuous in the tangential direction in the case of $\sigma_1 \neq \sigma_2$. In the diagram, the length of an arrow represents the magnitude of **E** field.

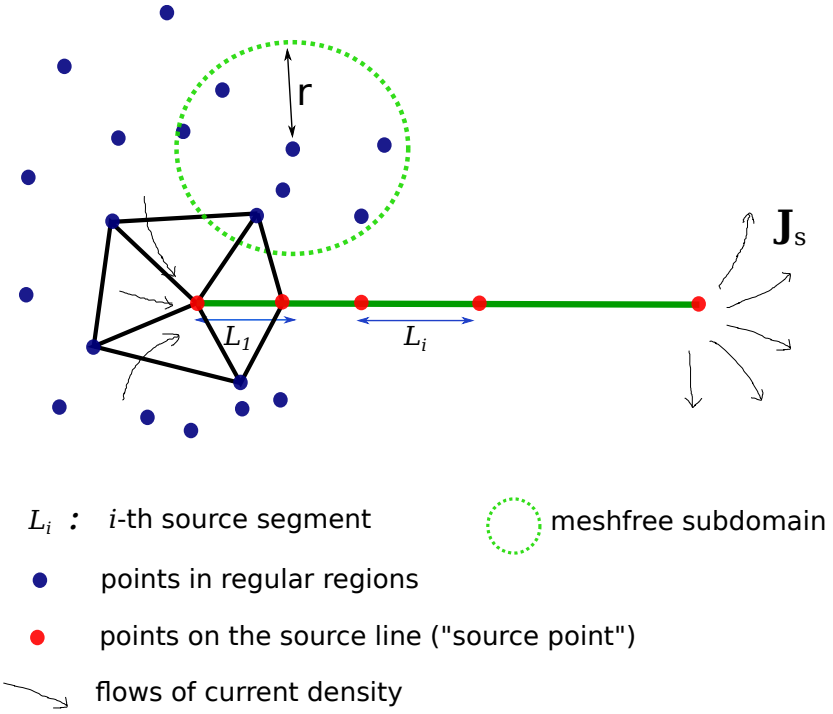

Figure 5.4. Schematic illustration of dealing with electric dipole source in the hybrid RBF-FD method. Shown above is a local mesh for the source point where EM fields are expected to be discontinuous.

mentation of the FE-coupled meshfree method (again referred to as hybrid meshfree solution hereinafter) then follows the procedure:

1. For all regular interior points in the meshfree discretization, use the PHS RBF-FD to approximate equations.

2. For any point that resides on the interfaces (if applicable), construct a local mesh and switch to scalar FE discretization.

3. For any point whose regular meshfree subdomain, as determined in the first step, intersects with points along the source wire (these points are denoted as "source points"), construct a local mesh and switch to scalar FE discretization.

4. For boundary points, use the homogeneous Dirichlet boundary condition $(\mathbf{A}, \psi) = (\mathbf{0}, 0)$.

For the primary-secondary field approach, there is no singular source function in the equations and therefore the above step of handling source terms is not needed. The implementation of the primary-secondary field approach is discussed later and is detailed in Appendix E.

5.4 Numerical examples

5.4.1 Total-field approach

In the total-field approach, the CSEM singular source functions are retained during the discretization of the equations. To allow for arbitrary shapes and positioning of a practical wire source (potentially with arbitrary geometry, either grounded or

loops) and efficient volume integration of the source function terms in an unstructured tetrahedral mesh, the wire is partitioned into a number of straight line segments, each of which is aligned with the edges of tetrahedra in the mesh. The number of the segments can be as many as needed. The implementation of the source terms in the scalar FE method is elaborated in Appendix F.

To examine the effectiveness of the proposed hybrid meshfree method for CSEM data modelling, analytical solutions (over simple and idealized models) and a scalar FE numerical solution are developed. The scalar FE method employs the total-field approach and unstructured tetrahedral meshes. The total-field FE algorithm is first validated so that it can be used as a benchmark solution for assessing hybrid meshfree solutions.

Validity of total-field FE implementation: whole space model

The conductivity model is the ideal homogeneous model, also called whole space model. The conductivity is uniform in this case, and analytical formulae for calculating EM fields due to an electric dipole or magnetic dipole are available. For an x-directed horizontal electric dipole source, the resulting electric field at the position $r = \sqrt{x^2 + y^2 + z^2}$ can be calculated via (eq 2.40 in Ward & Hohmann, 1988):

$$\mathbf{E}(r) = \frac{I_0}{4\pi\sigma r^3}\left[(\frac{x^2}{r^2}\mathbf{u}_x + \frac{xy}{r^2}\mathbf{u}_y + \frac{yz}{r^2}\mathbf{u}_z)(-k^2r^2 + 3ikr + 3) + (k^2r^2 - ikr - 1)\mathbf{u}_x\right], \tag{5.5}$$

where $k = \sqrt{-i\omega\mu_0\sigma}$ is wave number, $\omega = 2\pi f$ is angular frequency, $\mathbf{u}_k$ $(k = x, y, z)$ are unit vectors, and I_0 is the electric current intensity. In eq (5.5), the centre of the dipole is located at the origin $(x, y, z) = (0, 0, 0)$.

In this example, the uniform conductivity was chosen as $\sigma = 1.0$ S/m. The grounded wire of length $l_s = 200$ m was used, which is x-directed (the electric current flows from $x = -100$ m to $x = 100$ m) and has its two poles at $(-100, 0, 100)$ m and $(100, 0, 100)$ m, that is, the source wire is located at $y = 0$, $z = 100$ m. The synthetic measurement sites are at $z = 0$.

The mesh used for this example is a tetrahedral mesh with $144,601$ nodes and $901,084$ elements. The computational domain is $\Omega = \{(x, y, z)| -105 \text{ km} \leqslant x, y \leqslant 105 \text{ km}, -102 \text{ km} \leqslant z \leqslant 105 \text{ km}\}$. The 200 metre long wire source consists of 40 small segments, each of which is 5 m long. A local refinement at the source was applied such that the minimum edge length (MEL) in this region is $l = 5$ m. At the synthetic measurement locations that extend from $x = -14$ km to $x = 14$ km, a local refinement using a MEL of 10 m was also applied.

The computed E_x component of the electric field using the FE implementation at the frequencies $f = 1.0, 0.1$ and 10^{-4} Hz is shown in Fig 5.5. An analytical solution based on eq (5.5) was also plotted here. The analytical solution in the figure was obtained by scaling the solution in eq (5.5) by the length of the actual wire source, which is 200 m. It is observed that the FE results become increasingly more consistent with the analytical solution for the considered offsets as the frequency decreases. This is due to the same mesh discretization used for all frequencies. At high frequencies, the EM field oscillates and attenuates more rapidly in space, and therefore more refinements of the mesh would be required in order to obtain a comparable numerical accuracy to that of the low frequency solutions.

The formula in eq (5.5) is valid for a dipole source, namely, the calculated EM field response will be accurate for positions far away from the centre of the source

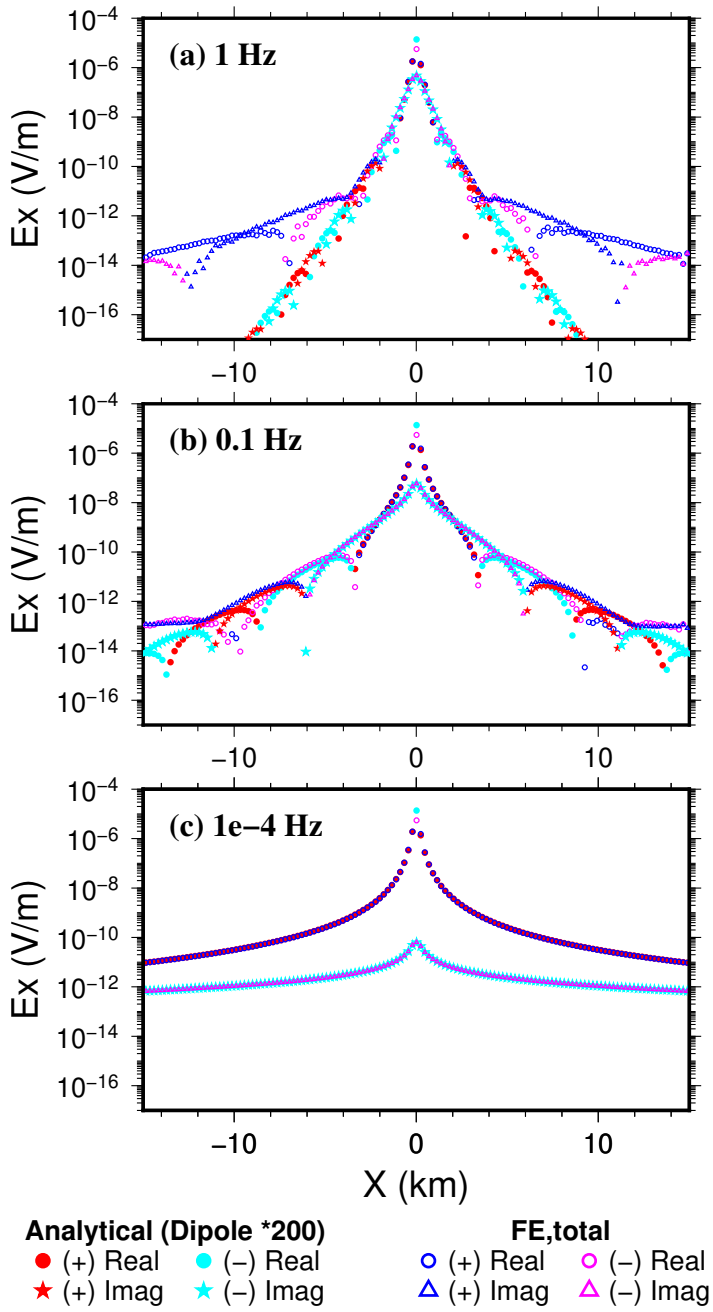

Figure 5.5. Comparison of the calculated E_x responses for the whole space model (σ = 1 S/m) using the total-field FE approach and the analytical approach. Positive and negative values are indicated by "+" and "-", respectively, in the figure's legends in addition to different colours of the symbols. Real and imaginary components of E_x are denoted by different symbols. The results are for three different frequencies: (a) 1 Hz, (b) 0.1 Hz and (c) 10^{-4} Hz.

for which the dipole geometry assumption of the source is valid. This is evident from Fig 5.6 which shows the same plots of E_x as in Fig 5.5 but for much shorter offsets from the wire source. At offsets that are more than 200 m away from $x = 0$, the FE solutions have excellent agreements with the scaled analytical ones.

Validity of total-field FE implementation: half space model

The second validation example for the total-field FE method is the so-called half space model where a uniform conductive layer is overlaid with a more resistive air layer. As before, the air layer's conductivity is approximated as 10^{-8} S/m in the diffusion regime. The conductive subsurface has the conductivity $\sigma = 0.01$ S/m, a common average value for near-surface Earth materials. To assess the numerical solutions, a number of measurement sites were distributed at the flat surface ($z = 0$) of the two layers.

Again, for this idealized case, analytical expressions for calculating the electric field at the surface are available. The E_x due to an x-directed horizontal electric dipole source can be calculated as (eq 4.159 in Ward & Hohmann, 1988)

$$E_x = \frac{I_0}{2\pi\sigma r^3}\left[1 + (ikr + 1)e^{-ikr} - \frac{3y^2}{r^2}\right], \tag{5.6}$$

where the meanings of the symbols are the same as those in eq (5.5).

For the FE discretization, a tetrahedral mesh with $63,823$ nodes and $395,298$ elements was used. The computational domain is $\Omega = \{(x, y, z)| - 40 \text{ km} \leqslant x, y, z \leqslant 40 \text{ km}\}$. The dipole source was represented by a 1 m grounded wire in the mesh that extends from $x = -0.5$ m to $x = 0.5$ m, which was refined with a MEL as 0.2

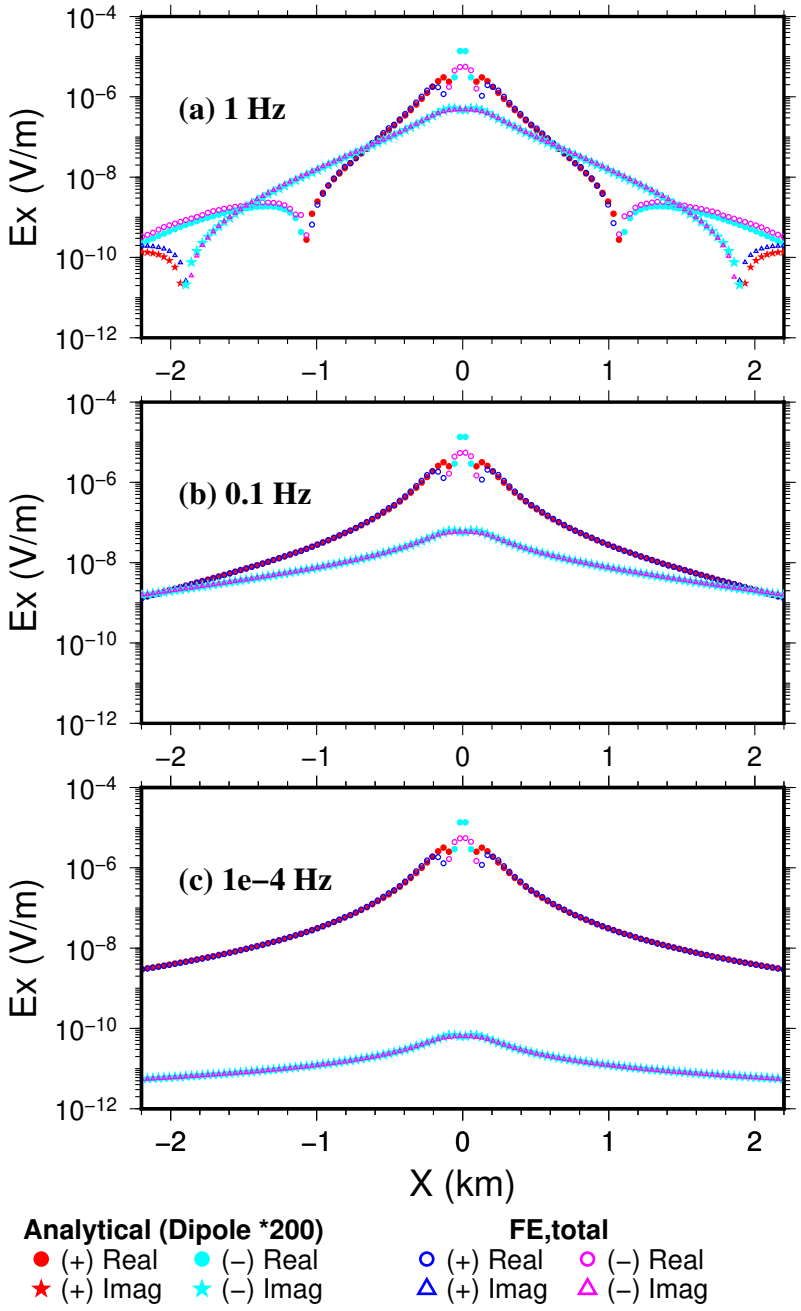

Figure 5.6. Same comparison plots as in Fig 5.5, but for shorter offsets from the source.

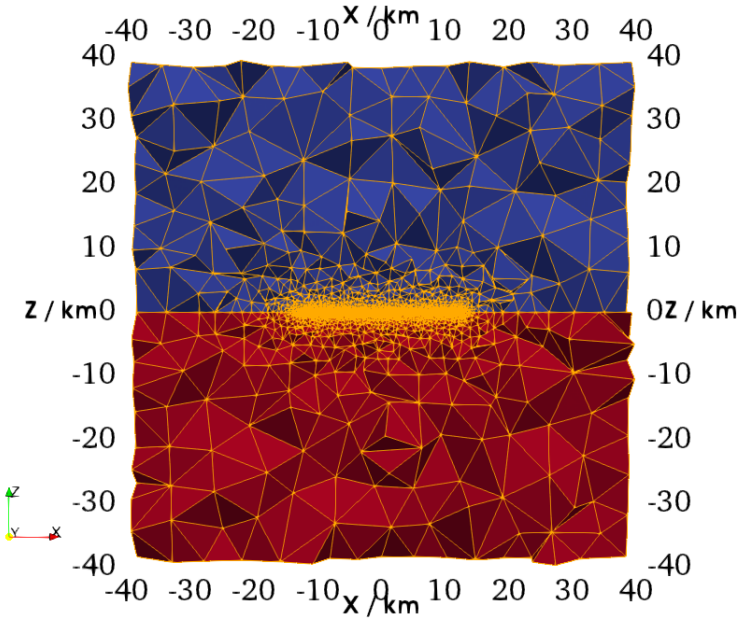

Figure 5.7. Vertical section of the unstructured tetrahedral mesh used for the half space model.

m. The measurement sites (-13 km $\leqslant x \leqslant 13$ km) were locally refined with a MEL of 30 m. A 3-D view of the mesh is shown in Fig 5.7. The computed E_x results using the total-field FE and the analytical means (eq (5.6)) at $f = 1$ Hz are shown in Fig 5.8. Again, the FE results are observed to match the analytical ones, validating the total-field FE algorithm.

Accuracy of total-field meshfree method: half space model

In order to assess the effectiveness of the implemented hybrid PHS RBF-FD meshfree method, the same half space model with appropriate local refinements as in the previous FE example was used. The grounded electric dipole source at the surface is extended to be 200 m long (from $x = -100$ m to $x = 100$ m) as a first attempt to investigate the effectiveness of the source implementation in the meshfree case. Since both dipole source and measurement sites are at the surface, discontinuities at the

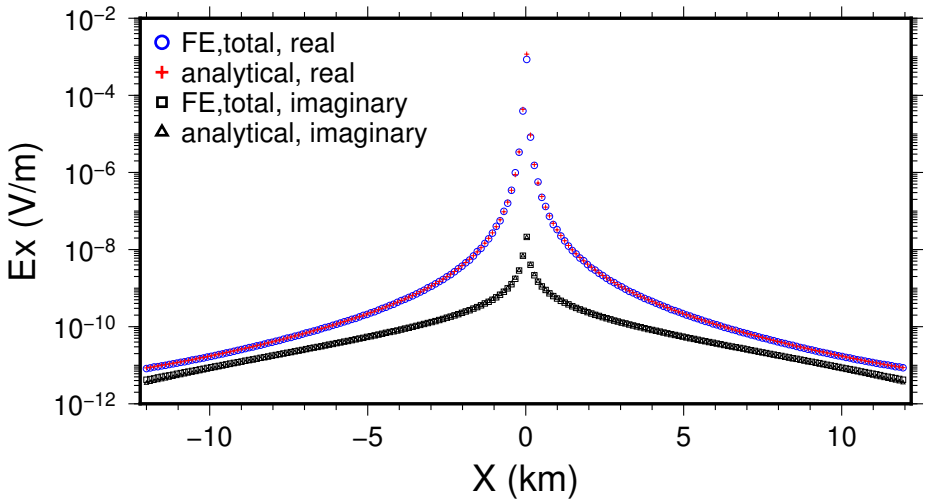

Figure 5.8. Total-field FE result of E_x component for the half space model compared with analytical solution. The source is a horizontal electric dipole. Positive values are indicated by coloured symbols, and negative values are indicated by black symbols. The frequency is $f = 1$ Hz.

source poles are expected in the numerical results for the electric field.

To compare the hybrid meshfree results to those of the total-field FE approach, a tetrahedral mesh was generated such that the MEL at the measurement locations is $l = 30$ m. The dipole source was represented by 40 straight line segments (5 m long each), where a MEL of 5 m was used for local refinements at the source points. This gives $26,027$ vertices and $158,269$ tetrahedral elements in the mesh. The meshfree point set is the vertices that were extracted from the mesh used for the FE method.

(i) Direct FE coupling with minimum FE discretizations

In this case, the FE discretization of equations is only used for the meshfree points whose subdomain intersects with the CSEM source points[1], as described in Section 5.3. This corresponds to the minimum amount of FE treatments for the

[1]Without explicit illustration otherwise, FE-like treatment is always used for meshfree points residing on the conductivity interfaces in a model.

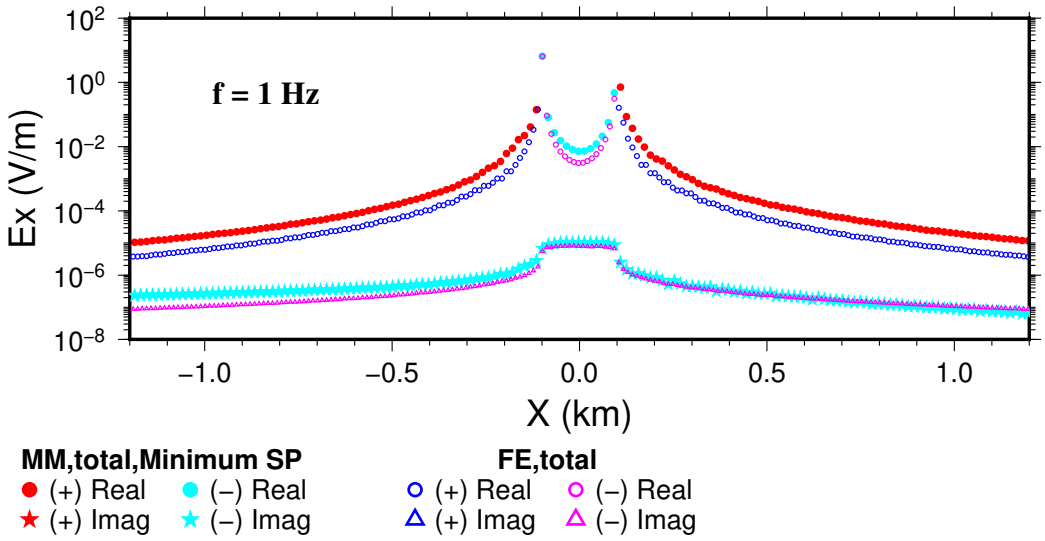

Figure 5.9. Hybrid meshfree (MM) numerical result of E_x component for the half space model compared with the total-field FE result. The frequency is $f = 1$ Hz. Minimum FE treatments for source points (SP) were used in the meshfree solution.

source term. The computed meshfree result along with the total-field FE result for the E_x component are shown in Fig 5.9. It is evident that the hybrid meshfree solution does have two discontinuities at exactly the source poles of the dipole source. However, the overall meshfree solution does not match exactly with that of the FE method. The stair-like pattern in the FE solution here (also in the following FE solutions) is due to the linear basis functions employed in each element (this means that the gradient of a function, e.g., E_x, within an element is a constant).

(ii) More FE treatments in direct FE-meshfree coupling

In this test, more FE-like treatments in discretizing the equations are used. The FE-like treatment region was increasingly extended from the source's centre. The points within $-R_s \leqslant x, y, z \leqslant R_s (R_s > 0)$ from the source centre were treated with the FE discretization, and were directly coupled with the rest of the points, which were treated with meshfree RBF-FD discretization. The calculated results in the case

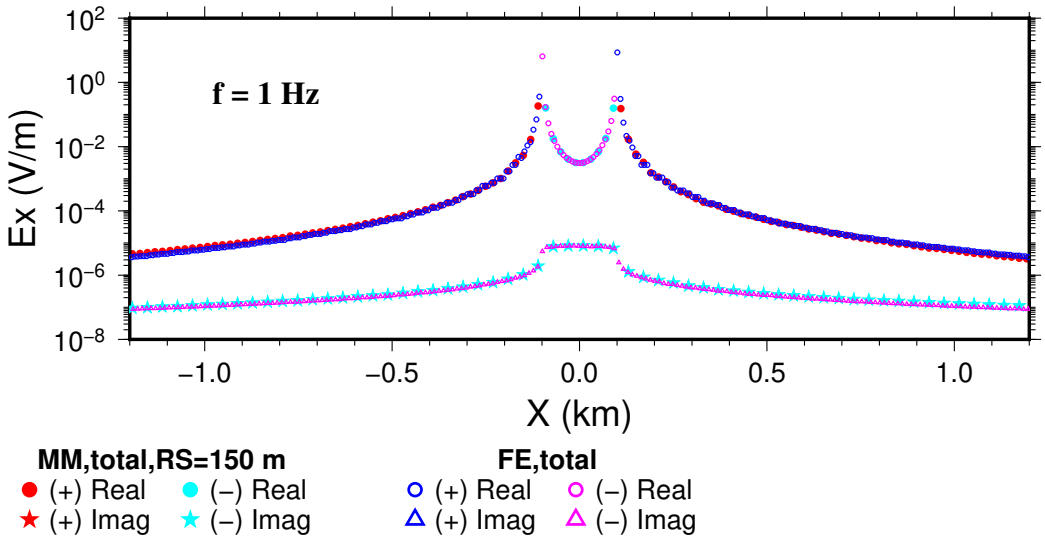

Figure 5.10. Hybrid meshfree numerical result of E_x component for the half space model compared with the total-field FE result. The frequency is $f = 1$ Hz. In the meshfree solution, FE treatments for source points were applied for any points within $R_s = max\{|x|, |y|, |z|\} = 150$ m in the meshfree point discretization.

of $R_s = 150$ m, 1 km and 3 km are shown in Figs 5.10, 5.11 and 5.12, respectively. It is seen that with more FE couplings, the hybrid meshfree result becomes more accurate. Fig 5.13 shows the comparison of the hybrid meshfree solutions and FE solutions over extended offsets in the case of $R_s = 3$ km.

In addition, three more remarks can be made from these observations: (1) the direct coupling of scalar FE and scalar meshfree RBF-FD can give continuous functions ($\mathbf{A}$ and ψ here) as well as continuous derivatives of the function (E_x) at the coupling boundary (e.g. $x = \pm 150$ m and $x = \pm 1$ km); (2) the FE coupling region for the controlled source does not need to be very large in order to obtain satisfactory overall numerical results; and (3) the direct coupling treatment for the source indeed enables the hybrid meshfree method to faithfully reproduce possible field discontinuities at the source, as predicted by the FE method. This is impossible in a standard meshfree

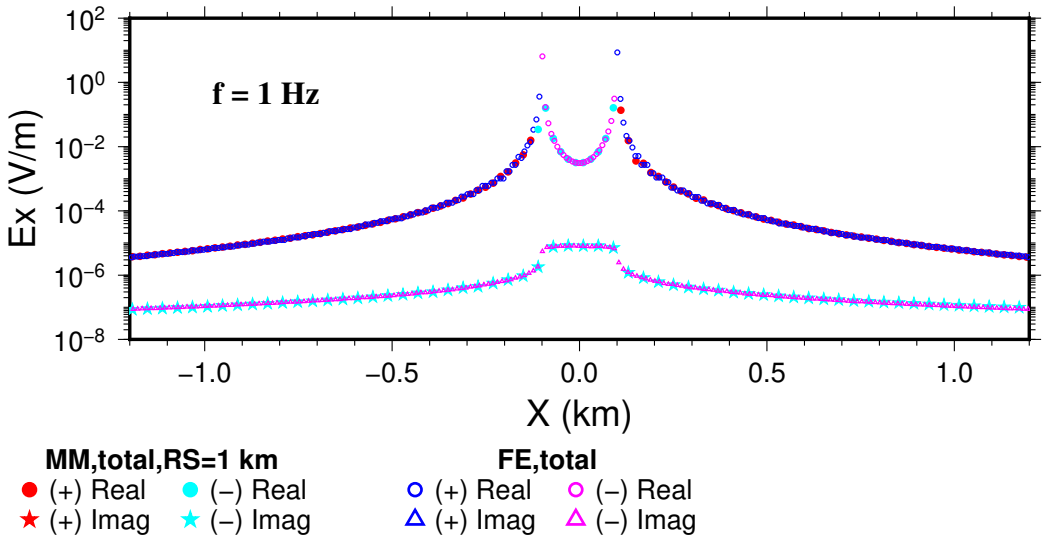

Figure 5.11. Same plots as in Fig 5.10, but with $R_s = 1$ km in the hybrid meshfree method.

method.

(iii) FE coupling for the homogeneous region containing the source

In this test, the horizontal 200 metre long dipole source is located at a depth of 500 m from the surface and the synthetic measurement locations are at the surface, which resembles borehole-to-surface EM surveys. The unstructured FE treatment was used for the conductive subsurface region containing the source, while the standard RBF-FD was used for the air layer. The calculated electric field responses (E_x) at the surface ($y = 0, z = 0$) using the hybrid meshfree and the total-field FE methods are shown in Fig 5.14. Again, the vertices of the unstructured tetrahedral mesh used by the FE method were employed as the meshfree point discretization. The stair-like feature in the FE solution is due to the use of linear basis functions which can be improved and smoothed if using finer local refinements at the measurement locations. The higher accuracy and better smoothness in the hybrid meshfree solution is due to the high-order accuracy in meshfree function approximation. An excellent agreement

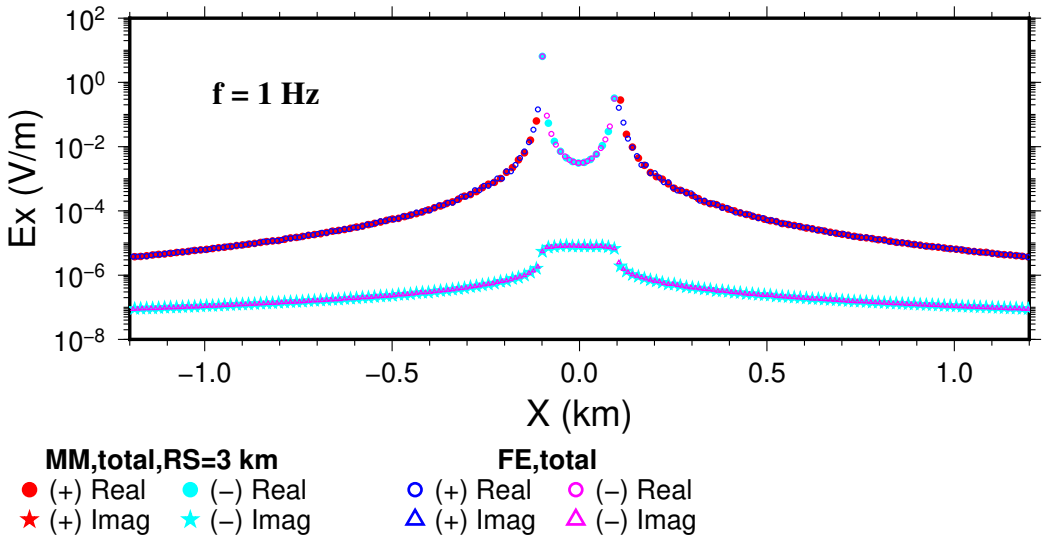

Figure 5.12. Same plots as in Fig 5.10, but with $R_s = 3$ km in the hybrid meshfree method.

between these two solutions is evident.

One issue remaining however is about the direct coupling with minimum FE point treatments, which gives unsatisfactory numerical results in the tests. One may try the trial-and-error method to determine the optimal direct coupling boundary for a particular problem if using as few FE treatments as possible is preferred. However, being able to determine this boundary prior to solving the problem would be useful. The main reason behind this issue is, at this stage, suspected to be the difference between meshfree shape functions and scalar linear FE shape functions. The shape functions in these two cases are constructed from different functional spaces. More investigations are needed to address this issue.

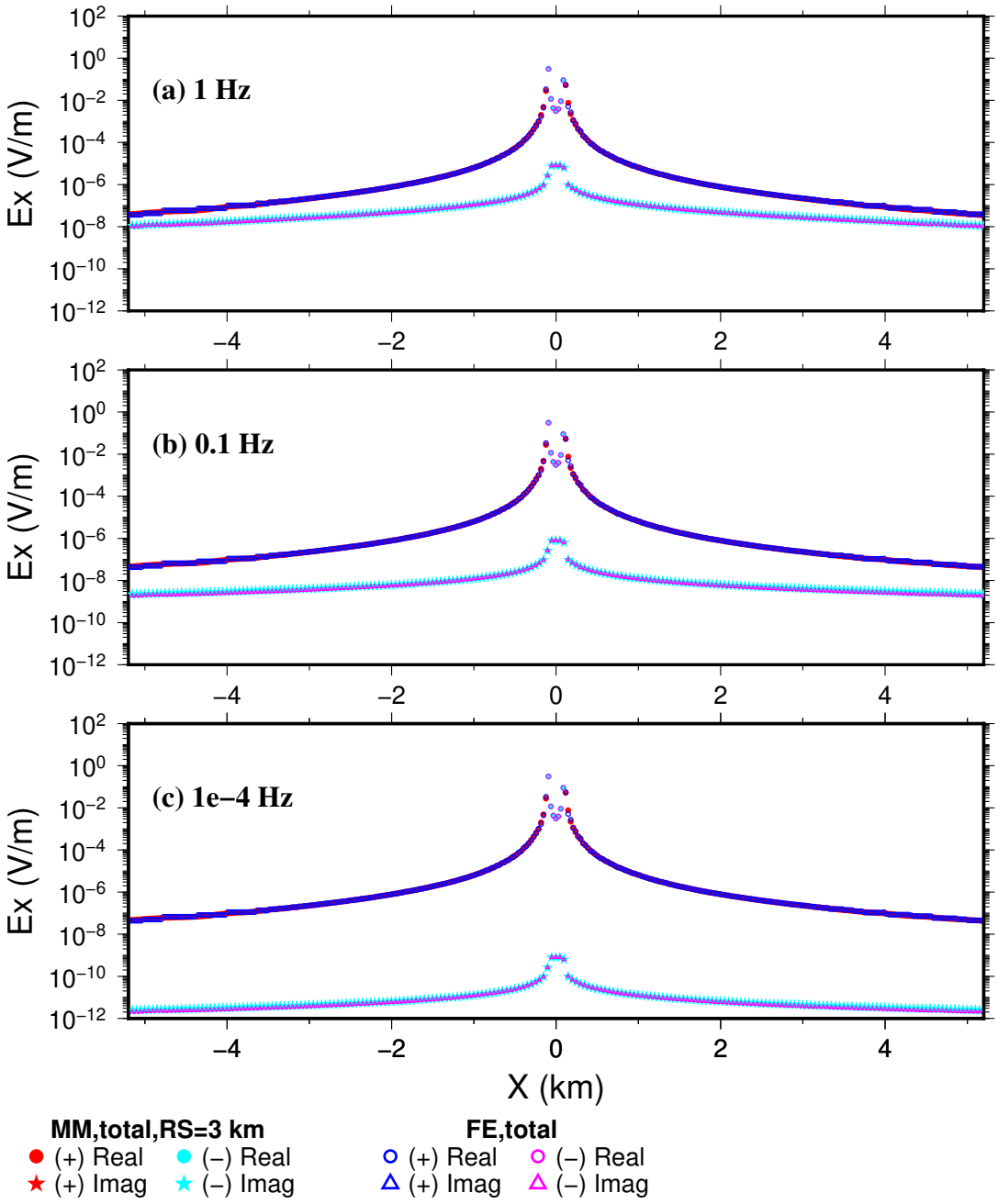

Figure 5.13. Same plots as in Fig 5.12, but over extended offsets and using more frequencies: (a) 1 Hz, (b) 0.1 Hz and (c) 10^{-4} Hz.

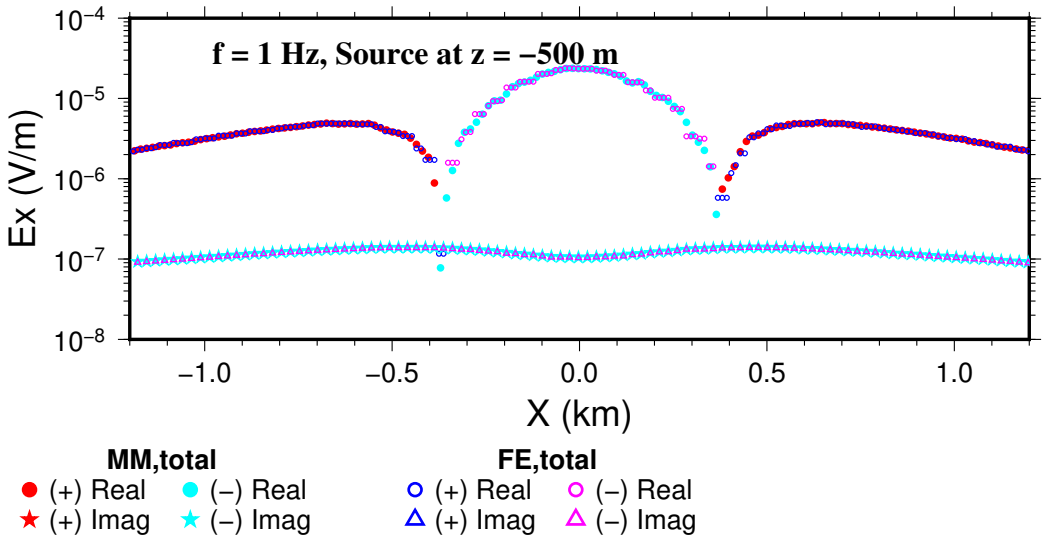

Figure 5.14. Hybrid meshfree (MM) numerical result of E_x component for the half space model compared with the total-field FE result. The 200 m long dipole source is located at $z = -500$ m. The frequency is $f = 1$ Hz.

5.4.2 Primary-secondary field approach

In the primary-secondary (PS) approach, a primary EM field response over some simple background conductivity model is first sought, for which analytical or semi-analytical formula are frequently used. A secondary EM field, or scattered field, is then caused only by the anomalous conductivity distribution $\sigma_{ano} = \sigma_{original} - \sigma_{background}$ (see Fig 5.1), which is the conductivity difference between the original conductivity distribution and the background conductivity model. The choice of the background model is subject to the user's discretion as long as the primary fields can be accurately and efficiently calculated. For a given discretization of the original conductivity model, the primary EM fields at the degrees of freedom where σ_{ano} is not zero are required before seeking a numerical solution for the secondary EM fields. Derivations of mathematical equations and algorithm implementations of the

PS approach in the frame of Coulomb-gauged **A**-ψ potential scheme are presented in Appendix E. The main steps for a PS approach-based numerical solution are:

1. Determine a background conductivity model, and calculate the primary EM response due to a controlled source over the background model for all measurement sites and for all regions where σ_{ano} is not zero.

2. Discretize the original conductivity model domain with appropriate meshes or meshfree points, and solve Maxwell's equations (here, **A**-ψ potential equations) for the secondary EM response.

3. Compute the total EM response due to the controlled source by summing up the primary and secondary EM responses.

Note that in a PS method, the singular CSEM source functions are avoided at the equation level. Here, scalar FE and hybrid scalar meshfree implementations using PS approach are developed. In this case, even the meshfree method does not face the difficulty caused by field discontinuities at the source. The FE PS implementation is investigated in order to provide an additional check on the PS algorithm implementations.

Validity of PS FE implementation

To first verify the validity of the PS approach-based FE implementation, the marine hydrocarbon disk model (also known as canonical disk model, Constable & Weiss, 2006; Ansari & Farquharson, 2014) is considered here. The model is graphically depicted in Fig 5.15. The model has a sea water layer at the top with conductivity

$\sigma = 3.2$ S/m, and a seabed layer beneath the sea water ($\sigma = 1.0$ S/m). A circular disk of resistive medium, which could be hydrocarbons or other less conductive materials, is embedded 1 km below the sea floor and has the radius of 1 km. The thickness of the disk (along z direction) is 100 m. This gives the centre of the disk as $(x, y, z) = (0, 0, -1000)$ m in the coordinate system here. A grounded electric dipole source[2] is typically used in the marine environment (Chave et al., 1991). In this example, an x-directed electric dipole source extending from -100 m to 0 m is adopted and is set to be at a height of 100 m above the sea floor.

In order to use the PS approach, a background model needs to be prescribed. Here, a homogeneous conductivity model with $\sigma = 3.2$ S/m is employed. The background model is simple enough such that the primary EM response can be efficiently computed. The analytical electric field is calculated by eq (5.5).

The measurement sites in a marine CSEM survey are normally distributed at the sea floor ($z = 0$) to maximize the signal amplitude from the exploration targets within the seabed due to the rapid attenuation of the EM field in sea water. For an actual grounded 100 m long line source, the field responses can be obtained from the dipole source response scaled by the length $l_s = 100$ m. Since in this example, the synthetic measurement sites and the regions where $\sigma_{ano} \neq 0$ are sufficiently far away from the source, the scaled responses from the dipole source are adequate for approximating the primary field.

The total electric field over the disk model was calculated using the PS FE approach (with the above scaling method for calculating the primary field) and the total-field FE method. The comparison between the two solutions of the E_x com-

[2]In this case, the electric current is injected into the conductive sea water.

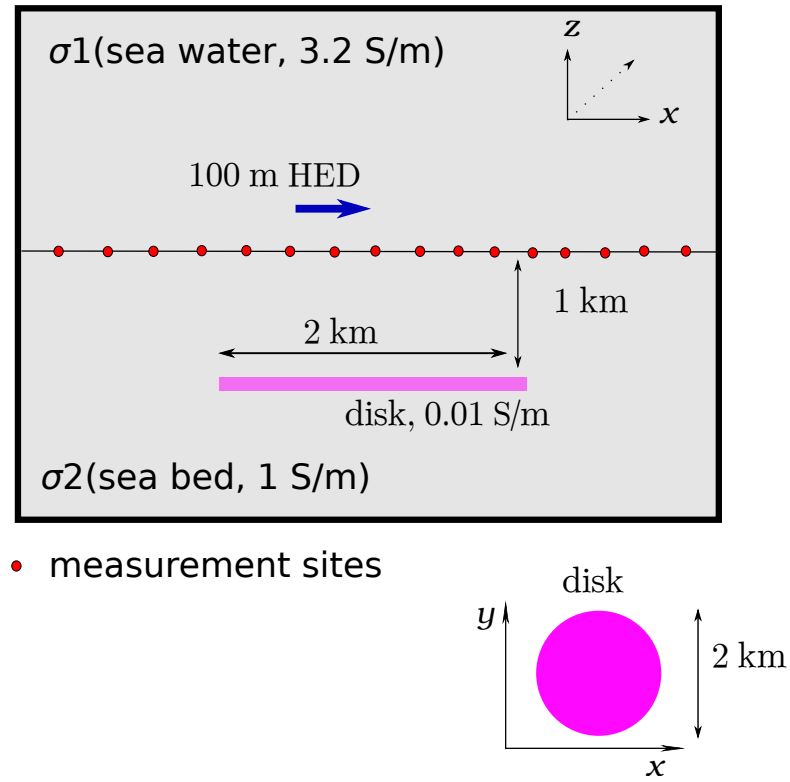

Figure 5.15. Diagram of the marine hydrocarbon disk model. The disk is located in the sea bed layer.

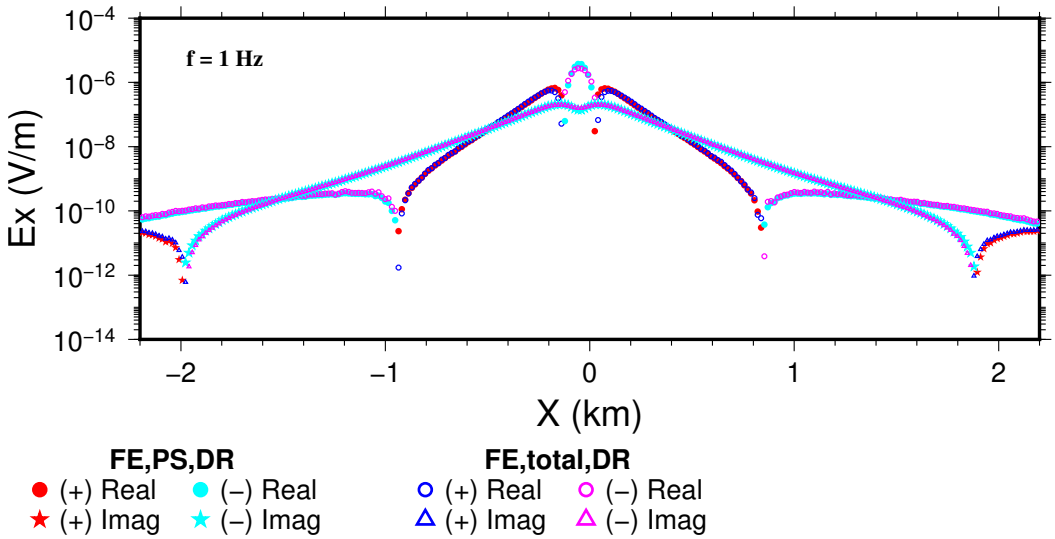

Figure 5.16. Comparison of the calculated E_x responses for the canonical disk model using the primary-secondary (PS) FE approach and total-field FE approach. In both implementations, the linear systems of equations were solved using a direct solver ("DR"). Positive and negative values are indicated by "+" and "-", respectively, in the figure in addition to different colours of the symbols. The frequency is $f = 1$ Hz.

ponent from these two implementations is shown in Fig 5.16 (1 Hz) and Fig 5.17 (10^{-4} Hz). The mesh discretization of the model is the same for both cases. The computational domain is $\Omega = \{(x, y, z)| - 10 \text{ km} \leqslant x, y, z \leqslant 10 \text{ km}\}$, which was discretized using an unstructured tetrahedral mesh. The mesh has local refinements at the synthetic measurement line (-6.5 km $\leqslant x \leqslant 6.5$ km, y=0, z=0) with a MEL of 5 m. The source and the disk were also refined to improve numerical accuracy for the total-field FE approach and PS FE implementations, respectively. The maximum edge length of tetrahedra in these regions was $l_{tra} \leq \frac{l_{skin}}{10}$ where l_{skin} is the approximate skin depth assuming a uniform space of conductivity $\sigma = 2.0$ S/m. This results in $1,773,558$ elements and $281,387$ nodes in the mesh.

The PS FE and total-field FE solutions have a good agreement with each other, as

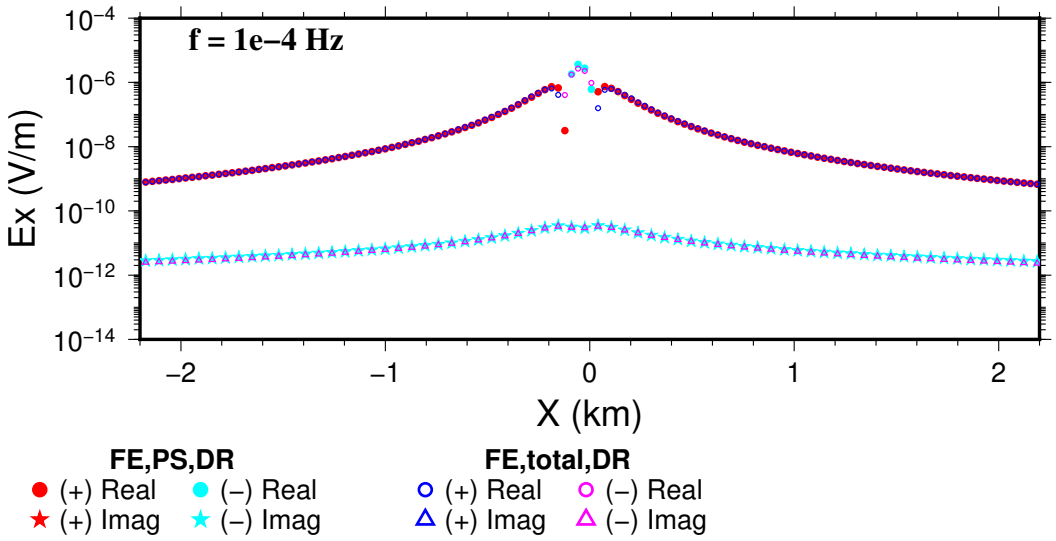

Figure 5.17. Same comparison plots as in Fig 5.16, but for the frequency $f = 10^{-4}$ Hz.

shown in the figures, confirming the accuracy of the PS FE implementation. Although a much coarser mesh would be adequate for low frequencies (such as 10^{-4} Hz here), the result of the low frequency using the fine mesh is presented here for confirmation of the stability of the implemented PS FE algorithm. The PS FE solution is further compared with a vector FE solution from the literature (Ansari & Farquharson, 2014), which uses a total-field approach, and the match is displayed in Fig 5.18. It is seen that the PS FE solution is consistent with the independent vector FE solution.

Accuracy of PS meshfree method

To examine the accuracy of the PS meshfree method, the same E_x component over the canonical disk model was calculated and compared first with the vector FE solution (Ansari & Farquharson, 2014) at 1 Hz. The meshfree discretization uses the same set of points (vertices) generated for the FE mesh. Fig 5.19 shows the comparison. From Fig 5.18 and Fig 5.19 it is seen that both the PS meshfree and PS FE solutions are

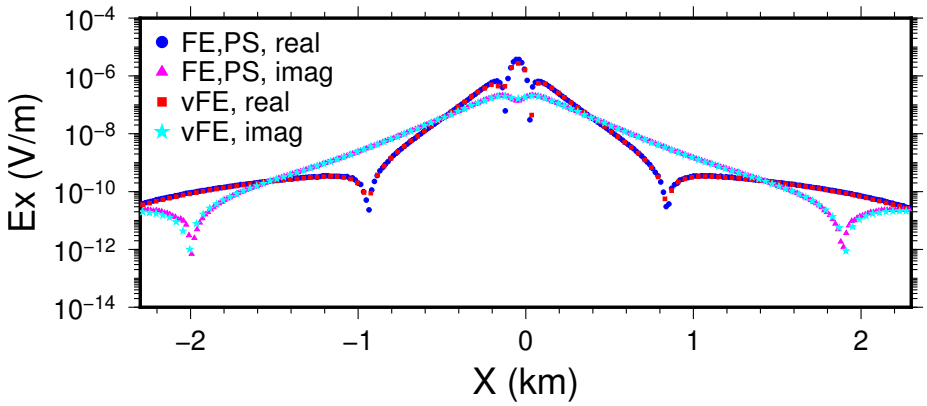

Figure 5.18. Scatter plot of the primary-secondary (PS) scalar FE solution of E_x in a comparison with a total-field vector FE solution (Ansari & Farquharson, 2014) for the frequency $f = 1$ Hz. Symbols of the vector FE solution are indicated as "vFE".

consistent with the vector FE solution, especially at offsets near the wire source. The meshfree solution at 1 Hz is found to be less accurate at far offsets in this example.

To further examine the accuracy of PS meshfree solution, the meshfree solution is compared against that of the PS scalar FE implementation for different frequencies. At high frequency (100 Hz), it is found that both numerical solutions are noisy. This is due to insufficient spatial discretization in the mesh or meshfree points. As the frequency decreases, in which case the EM field oscillates more slowly, both solutions become increasingly more accurate. The match between the PS meshfree and PS FE solutions is displayed in Fig 5.20 which shows the comparison for three lower frequencies. The case of 10^{-8} Hz corresponds to extremely low frequency or near static situation (i.e. DC case). In DC resistivity surveys ($f = 0$ Hz), the measured signals of electric potential (and therefore electric field) become real-valued measurements. This is the reason why the imaginary part of the solutions in Fig 5.20 is rapidly approaching 0 as $f \to 0$.

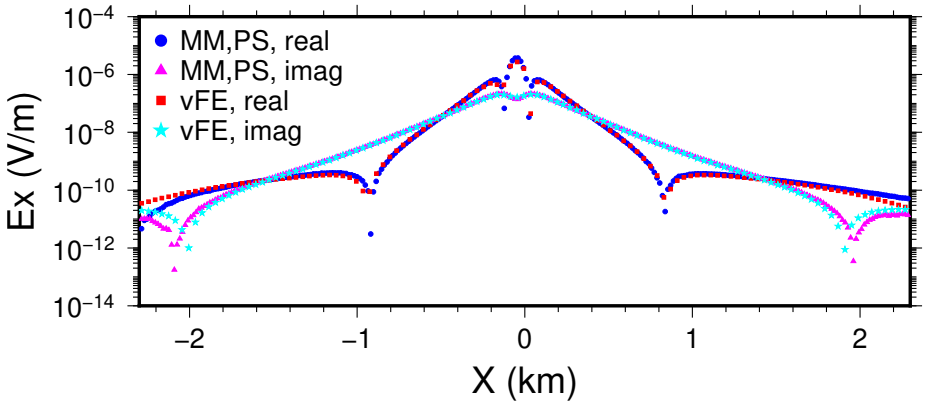

Figure 5.19. Scatter plot of the primary-secondary (PS) meshfree ("MM") solution of E_x in a comparison with a total-field vector FE ("vFE") solution (Ansari & Farquharson, 2014) for the frequency $f = 1$ Hz.

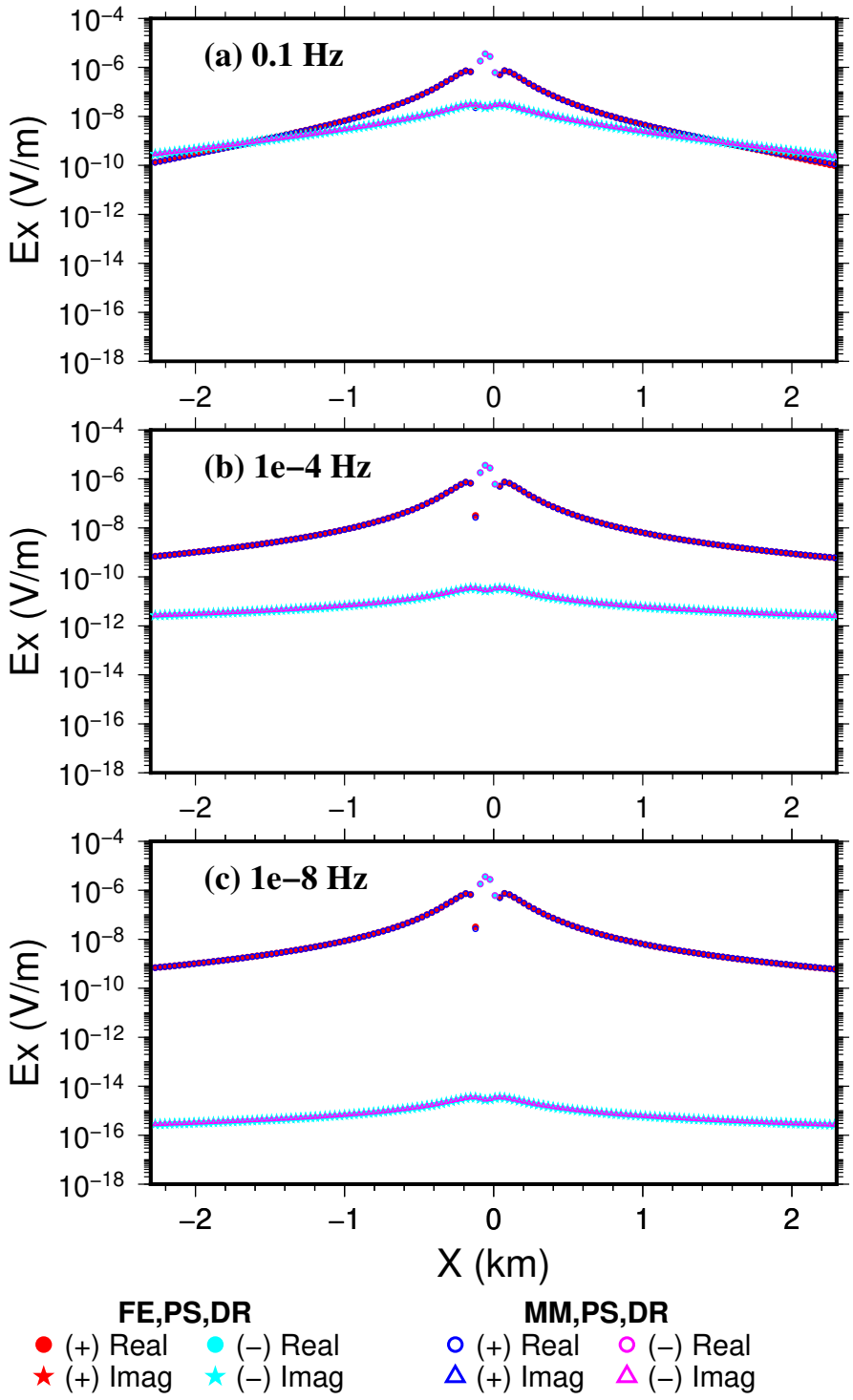

Figure 5.20. Comparison plots of the primary-secondary (PS) mesh-free ("MM") solution and PS FE solution of E_x in the canonical disk model for three different frequencies $f = 0.1, 10^{-4}$ and 10^{-8} Hz.

5.5 Chapter summary

The hybrid PHS RBF-FD meshfree method is further extended to solve CSEM forward modelling in this chapter. The modelling difficulty introduced by EM controlled sources is the infinity discontinuities, or singularities, at the source which are different from the field discontinuities encountered in the MT case. To overcome the difficulty, both total-field and primary-secondary field approaches in the frame of RBF-FD meshfree method are investigated. In the total-field approach, direct coupling with FE treatment is proposed and tested. It shows that the strong-weak form coupling scheme works if the coupling domain is appropriate. The primary-secondary approach does not face the singularity issue inherently. The primary-secondary meshfree method is shown to be able to synthesize correctly the CSEM responses using dipole sources.

Chapter 6

Discussion

This thesis attempts to address the fundamental problems encountered when developing new meshfree algorithms that are capable of modelling EM data over complex conductivity models. The novelties of the work include introducing a new class of RBFs in applying the RBF-FD method for modelling geophysical data, the use of 3-D completely unstructured meshfree points in discretizing models, a new technique for reproducing discontinuous derivatives in meshfree solutions and the use of meshfree methods in the frame of both total-field and primary-secondary field approaches for modelling CSEM data.

In RBF-FD, various RBFs can be employed. The quintic order polyharmonic (PHS) RBFs studied here have the advantages: (1) they do not have a shape parameter that requires extra computational effort to determine an optimal value in each meshfree subdomain in a set of unstructured points, and (2) the resulting linear system of equations in the meshfree interpolation does not become very ill-conditioned. As such, a standard Lagrange interpolation condition can be used, making the im-

plementation of Dirichlet boundary conditions straightforward and efficient. The use of the strong-form RBF-FD method also avoids numerical integration when discretizing continuous PDEs into algebraic equations, a computationally costly procedure in common weak-form meshfree methods.

Other PHS RBFs can also be used in principle, as long as they are capable of approximating the highest order derivatives. In this thesis, the quintic order PHS RBFs are sufficient to approximate the second-order differential operators. Using higher order RBFs would increase the computation in meshfree interpolation by increasing arithmetic operations.

There are other means to generate 3-D unstructured points. The way used here (Tetgen, Si, 2015) is certainly not the most efficient one, but it provides a means to also generate an unstructured tetrahedral mesh with which comparison studies, in terms of algorithm implementation and computational efficiency, with other numerical algorithms (e.g., FE) are allowed. The use of unstructured model discretizations is a key requirement during the development of the meshfree techniques here. This is the reason that all example meshfree discretizations have used unstructured points, even though the considered geophysical models are sometimes simple and ideal (e.g., EM models). More examples of discretizing realistically complex models using meshfree points are presented in Long & Farquharson (2019a).

It would be reasonable to argue that the accuracy of a meshfree numerical solution depends on the quality or regularity of the meshfree points, just as the solution of mesh-based methods (e.g., FE, FV, grid-based FD) depends on the mesh quality. A quantitative analysis of the effect of the point regularity on accuracy has not been addressed here. Part of the reason for this is that there is still a lack of accessible

software to generate point discretizations tuned for meshfree methods. The tool used here (Tetgen, Si, 2015) was originally designed for generating meshes. The criteria for a quality mesh are different from those for a set of quality points. This means that the vertices from a quality tetrahedral mesh are not necessarily of good quality when used for a meshfree solution. As such, it is inconsistent to ensure a set of quality points by generating a quality mesh.

Unlike the gravity field, the geophysical EM field has well-known discontinuities in the electric field. In order to faithfully reproduce possibly discontinuous electric field at the conductivity jumps in a quasi-static regime, a hybrid meshfree discretization that couples scalar FE discretization of equations for interfacial points is proposed. This is based on the fact that the electric field, thus the first-order derivative of ψ, is discontinuous across any conductivity jumps, while the functions approximated by standard meshfree methods are undesirably smooth everywhere. The coupling method is proposed with the goal of minimizing the algorithm's reliance on the information of interfacial geometries which are complex in nature for 3-D realistic Earth models.

The coupling strategy is not needed if the functions in the PDEs are globally smooth, which is true in the EM scenario if, for example, the conductivity variation is smooth everywhere (e.g., a smooth model generated by standard minimum-structure style inversion algorithms that encourage a certain smoothness), or the conductivity is a 1-D distribution with a plane wave source excitation (i.e., MT). In these cases, the standard RBF-FD technique, as used in modelling gravity data, would suffice.

In synthesizing CSEM data using the primary-secondary field approach, the singular source terms are avoided in the equation system and therefore there is no numerical

singularity in the meshfree solution. However, there are situations where finding a primary field response becomes difficult or not computationally efficient, as mentioned in Section 5.1. The total-field approach may thus become the only option. The direct coupling between the linear FE and RBF-FD discretizations of potential equations is shown to be able to correctly model CSEM responses. Traditionally, the purpose of coupling meshfree methods with other numerical methods is to take advantage of the flexibility of meshfree methods in conforming with irregular geometries. Here, the main purpose is to take advantage of the better approximation of singular functions in the FE method.

Another worthy discussion would be about how to apply the meshfree-based modelling solvers in an inversion computation, which is frequently encountered in geophysical data interpretation. As the whole problem domain is discretized by points, the usual, standard cell-based or pixel-based inversion method will not be practical. Since in the cell-based inversions where the cells' conductivities (or other physical properties) are to be inverted, the conductivity jumps arising from iterative changes of those conductivity values can be arbitrary and thus difficult to predict. However, the meshfree point discretization is very suitable for an inversion philosophy where contact surface geometries of rock units are the primary degrees of freedom (Lelièvre et al., 2012, 2016). The idea is to mainly invert the surface structures such as wireframes of lithological units. A closely-related inversion application in the EM case for this idea is discrete conductor inversion where the conductor is described using ideal surfaces (e.g., spheres) such that analytical solutions can be used (Vallée, 2015). Models recovered from a surface inversion have sharp contact surfaces among different rock units, and are thus more consistent with geological models than those smooth

models recovered from standard cell-based minimum-structure style inversions.

Chapter 7

Conclusions

This thesis investigates the feasibility and applicability of RBF-FD meshfree techniques in forward modelling geophysical EM data over 3-D Earth models. Given the potential advantage of meshfree point discretization in dealing with complicated real-life Earth models, the thesis is focused on developing numerical meshfree methods that are capable of faithfully synthesizing EM responses for 3-D inhomogeneous conductivity models.

RBF-FD method is a strong-form meshfree method, therefore there is no need to construct any background mesh and no need to carry out numerical integration in discretizing continuous PDEs into algebraic equations. The quintic order polyharmonic (PHS) RBFs are employed in this thesis to discretize up to second-order derivatives in PDEs. A convergence analysis of PHS RBF-FD is presented and demonstrated numerically in the context of synthesizing geophysical gravity data first. Since the model discretization uses unstructured points, both global and local point refinements are considered and it is shown that the meshfree solution converges to the true so-

lution under both types of refinements (h refinements). The rate of convergence of the meshfree method under h refinements is shown to be determined by the order of enriched polynomials. The RBF-FD stencil size, which is defined as the number of points in a meshfree subdomain, affects the accuracy and computational efficiency of a numerical solution. Choosing the stencil size approximately as 30 proves to be adequate for approximating second-order differential operators (e.g., Laplacian) in 3D while at the same time maintaining the sparsity structure of the global linear system of equations.

Using PHS RBF-FD (enriched with quadratic polynomials) and linear scalar FE methods to synthesize gravity and gravity gradient data, it is concluded that both numerical solutions converge to the analytical solution, but with different convergence rates: the meshfree method has a quadratic convergence rate whereas the FE method has only a linear convergence rate. The RBF-FD solution however requires more computational efforts than the FE counterpart, provided the meshfree point discretization and FE mesh are already available. The capability of dealing with irregular model geometry with the unstructured points used by the meshfree method is also demonstrated. The RBF-FD method is concluded as an effective numerical method in forward modelling the smooth gravity field.

In synthesizing MT data by PHS RBF-FD method, Maxwell's equations in terms of electric field and magnetic field are transformed into EM potential functions, namely, the vector magnetic potential ($\mathbf{A}$) and scalar electric potential (ψ). This allows the PHS RBF-FD, a scalar meshfree method, to be directly used for approximating globally continuous EM potentials. A hybrid meshfree discretization of equations coupled with linear scalar FE treatment for interfacial points is proposed to

overcome the difficulty of possible EM field discontinuities. The effectiveness of the proposed hybrid RBF-FD meshfree method is verified with three synthetic MT examples. For all examples, the meshfree solutions are validated with other independent numerical solutions. The possible discontinuities in the electric field are found to be faithfully modelled in the meshfree solution. It is also confirmed that the coupling strategy is capable of dealing with high conductivity contrast in the forward modelling problem. These observations establish the hybrid meshfree method as a new option in forward modelling MT data over 3-D conductivity models with complex geometry.

The use of the above hybrid meshfree RBF-FD in synthesizing frequency-domain CSEM data is also investigated. In this scenario, numerical singularities at the electric dipole source positions arise in the numerical solution. To overcome this issue in the meshfree method, both total-field approach and primary-secondary approach have been experimented.

In the total-field approach, the direct coupling with scalar FE discretization of equations for source regions is proposed. The FE coupling is direct in the sense that there is no need to modify FE or meshfree shape functions at the coupling boundaries. For the direct coupling strategy, different degrees of the FE coupling are explored and tested. It is found that while in all cases the hybrid meshfree solution honestly reproduces the numerical singularities in the electric field, the overall meshfree solution in the case of minimum FE coupling does not match well the correct solution. The mismatch is resolved by using more FE coupling around the source region. It is numerically demonstrated that accurate overall meshfree solutions for CSEM data modelling with an electric dipole source (finite length or point) can be

obtained without using too many FE coupling discretizations. However, an optimal amount of FE couplings in discretizing equations in the hybrid RBF-FD is not clear yet.

The primary-secondary field approach is also implemented, using both hybrid meshfree method and more traditional FE method. The implementation of the primary-secondary field approach in the frame of Coulomb-gauged potential system is first validated by using scalar FE method for the marine canonical disk model with a grounded dipole source. The same implementation using the hybrid meshfree method is then validated by comparing the meshfree solution to the corresponding FE solution. It is shown that the primary-secondary meshfree solution yields satisfactory numerical accuracies, confirming the capability of the hybrid meshfree method in accurately synthesizing CSEM data. It is concluded here that in both approaches (total-field and primary-secondary), the proposed hybrid meshfree method is shown to be effective in obtaining accurate CSEM responses over the tested models.

The proposed meshfree methods are far from replacing the traditional mesh-based FE and FD methods for routine 3-D EM modelling tasks. The main concern is the slower computation in assembling the matrix of the linear system of equations in the meshfree methods. However, in situations where 3-D quality meshing for complex geometric features becomes very difficult or even not computationally feasible, the meshfree methods now become a feasible, and likely the only viable, option. Further research in the future in coupling meshfree methods with mesh-based methods (therefore speeding up the matrix assembling) and in developing 3-D meshfree point generation software would benefit greatly the geophysical community.

Bibliography

Alumbaugh, D. L., Newman, G. A., Prevost, L., & Shadid, J. N., 1996. Three-dimensional wideband electromagnetic modeling on massively parallel computers, *Radio Science*, **31**(1), 1–23.

Anderson, E., Bai, Z., Bischof, C., Blackford, S., Demmel, J., Dongarra, J., Du Croz, J., Greenbaum, A., Hammarling, S., McKenney, A., & Sorensen, D., 1999. *LAPACK Users' Guide*, Society for Industrial and Applied Mathematics, Philadelphia, PA, 3rd edn.

Ansari, S. & Farquharson, C. G., 2014. 3D finite-element forward modeling of electromagnetic data using vector and scalar potentials and unstructured grids, *Geophysics*, **79**(4), E149–E165.

Ansari, S., Farquharson, C., & MacLachlan, S., 2017. A gauged finite-element potential formulation for accurate inductive and galvanic modelling of 3-D electromagnetic problems, *Geophysical Journal International*, **210**(1), 105–129.

Atluri, S. N. & Shen, S., 2002. The Meshless Local Petrov-Galerkin (MLPG) method: A simple & less-costly alternative to the finite element and boundary element methods, *CMES - Computer Modeling in Engineering and Sciences*, **3**(1), 11–51.

Atluri, S. N. & Zhu, T., 1998. A new meshless local Petrov-Galerkin (MLPG) approach in computational mechanics, *Computational Mechanics*, **22**(2), 117–127.

Atluri, S. N., Kim, H. G., & Cho, J. Y., 1999. Critical assessment of the truly Meshless Local Petrov-Galerkin (MLPG), and Local Boundary Integral Equation (LBIE) methods, *Computational Mechanics*, **24**, 348–372.

Badea, E. a., Everett, M. E., Newman, G. a., & Biro, O., 2001. Finite-element analysis of controlled-source electromagnetic induction using Coulomb-gauged potentials, *Geophysics*, **66**(3), 786–799.

Banerjee, B. & Das Gupta, S., 1977. Gravitational attraction of a rectangular paral-

lelepiped, *Geophysics*, **42**(5), 1053–1055.

Barnett, C., 1976. Theoretical modeling of the magnetic and gravitational fields of an arbitrarily shaped three-dimensional body, *Geophysics*, **41**(6), 1353–1364.

Batra, R., Porfiri, M., & Spinello, D., 2004. Treatment of material discontinuity in two meshless local Petrov-Galerkin (MLPG) formulations of axisymmetric transient heat conduction, *International Journal for Numerical Methods in Engineering*, **61**(14), 2461–2479.

Bayona, V., Moscoso, M., Carretero, M., & Kindelan, M., 2010. RBF-FD formulas and convergence properties, *Journal of Computational Physics*, **229**(22), 8281–8295.

Bayona, V., Flyer, N., Fornberg, B., & Barnett, G. A., 2017. On the role of polynomials in RBF-FD approximations: II. Numerical solution of elliptic PDEs, *Journal of Computational Physics*, **332**, 257–273.

Bear, G. W., Al-Shukri, H. J., & Rudman, A. J., 1995. Linear inversion of gravity data for 3-d density distributions, *Geophysics*, **60**(5), 1354–1364.

Belytschko, T., Lu, Y. Y., & Gu, L., 1994. Element-free Galerkin methods, *International Journal for Numerical Methods in Engineering*, **37**(April 1993), 229–256.

Belytschko, T., Krongauz, Y., Organ, D., Fleming, M., & Krysl, P., 1996. Meshless methods: An overview and recent developments, *Computer Methods in Applied Mechanics and Engineering*, **139**(1-4), 3–47.

Biro, O. & Preis, K., 1989. On the use of the magnetic vector potential in the finite-element analysis of three-dimensional eddy currents, *IEEE Transactions on magnetics*, **25**(4), 3145–3159.

Biro, O. & Preis, K., 1990. Finite element analysis of 3-D eddy currents, *IEEE Transactions on Magnetics*, **26**(2), 418–423.

Blakely, R. J., 1996. *Potential theory in gravity and magnetic applications*, Cambridge University Press.

Börner, R.-U., 2010. Numerical Modelling in Geo-Electromagnetics: Advances and Challenges, *Surveys in Geophysics*, **31**(2), 225–245.

Brenner, S. & Scott, R., 2007. *The mathematical theory of finite element methods*, vol. 15, Springer Science & Business Media.

Buhmann, M. D., 2003. *Radial Basis Functions*, Cambridge University Press, Cam-

bridge.

Cai, Y. & Wang, C.-y., 2005. Fast finite-element calculation of gravity anomaly in complex geological regions, *Geophysical Journal International*, **162**(3), 696–708.

Chandhini, G. & Sanyasiraju, Y., 2007. Local RBF-FD solutions for steady convection-diffusion problems, *International Journal for Numerical Methods in Engineering*, **72**(3), 352–378.

Chasseriau, P. & Chouteau, M., 2003. 3D gravity inversion using a model of parameter covariance, *Journal of applied geophysics*, **52**(1), 59–74.

Chave, A. D., Constable, S. C., & Edwards, R. N., 1991. Electrical exploration methods for the seafloor, in *Electromagnetic Methods in Applied Geophysics: Volume 2, Application, Parts A and B*, pp. 931–966, Society of Exploration Geophysicists.

Chen, J.-S., Hillman, M., & Chi, S.-W., 2017. Meshfree methods: Progress made after 20 years, *Journal of Engineering Mechanics*, **143**(4), 04017001: 1–38.

Coggon, J. H., 1971. Electromagnetic and electrical modeling by the finite element method, *Geophysics*, **36**(1), 132–155.

Constable, S. & Weiss, C. J., 2006. Mapping thin resistors and hydrocarbons with marine EM methods: Insights from 1D modeling, *Geophysics*, **71**(2), G43–G51.

Cordes, L. & Moran, B., 1996. Treatment of material discontinuity in the element-free Galerkin method, *Computer Methods in Applied Mechanics and Engineering*, **139**(1-4), 75–89.

Davis, K. & Li, Y., 2011. Fast solution of geophysical inversion using adaptive mesh, space-filling curves and wavelet compression, *Geophysical Journal International*, **185**(1), 157–166.

Davydov, O. & Oanh, D. T., 2011a. Adaptive meshless centres and RBF stencils for Poisson equation, *Journal of Computational Physics*, **230**(2), 287–304.

Davydov, O. & Oanh, D. T., 2011b. On the optimal shape parameter for Gaussian radial basis function finite difference approximation of the Poisson equation, *Computers & Mathematics with Applications*, **62**(5), 2143–2161.

Davydov, O. & Schaback, R., 2016. Error bounds for kernel-based numerical differentiation, *Numerische Mathematik*, **132**(2), 243–269.

Ding, H., Shu, C., & Tang, D., 2005. Error estimates of local multiquadric-based differential quadrature (LMQDQ) method through numerical experiments, *Inter-*

national journal for numerical methods in engineering, **63**(11), 1513–1529.

Dolbow, J. & Belytschko, T., 1999. Numerical integration of the Galerkin weak form in meshfree methods, *Computational mechanics*, **23**(3), 219–230.

Du, Q., Gunzburger, M., & Ju, L., 2002. Meshfree, probabilistic determination of point sets and support regions for meshless computing, *Computer methods in applied mechanics and engineering*, **191**(13-14), 1349–1366.

Du, Q., Wang, D., & Zhu, L., 2009. On mesh geometry and stiffness matrix conditioning for general finite element spaces, *SIAM Journal on Numerical Analysis*, **47**(2), 1421–1444.

Duarte, C. A. & Oden, J. T., 1996a. Hp clouds-an hp meshless method, *Numerical methods for partial differential equations*, **12**(6), 673–706.

Duarte, C. A. & Oden, J. T., 1996b. An h-p adaptive method using clouds, *Computer methods in applied mechanics and engineering*, **139**(1-4), 237–262.

Dunham, M. W., Ansari, S., & Farquharson, C. G., 2018. Application of 3D marine controlled-source electromagnetic finite-element forward modeling to hydrocarbon exploration in the Flemish Pass Basin offshore Newfoundland, Canada, *Geophysics*, **83**(2), WB33–WB49.

Dyck, A. V. & West, G. F., 1984. The role of simple computer models in interpretations of wide-band, drill-hole electromagnetic surveys in mineral exploration, *Geophysics*, **49**(7), 957–980.

D'Urso, M., 2014a. Analytical computation of gravity effects for polyhedral bodies, *Journal of Geodesy*, **88**(1), 13–29.

D'Urso, M., 2014b. Gravity effects of polyhedral bodies with linearly varying density, *Celestial Mechanics and Dynamical Astronomy*, **120**(4), 349–372.

Evans, R. L., 2012. Earth's electromagnetic environment, in *The Magnetotelluric Method, Theory and Practice*, pp. 50–121, Cambridge University Press, Cambridge.

Everett, M. E., 2013. *Near-surface applied geophysics*, Cambridge University Press.

Fabri, A., Giezeman, G.-J., Kettner, L., Schirra, S., & Schönherr, S., 2000. On the design of CGAL a computational geometry algorithms library, *Software: Practice and Experience*, **30**(11), 1167–1202.

Farquharson, C. & Mosher, C., 2009. Three-dimensional modelling of gravity data using finite differences, *Journal of Applied Geophysics*, **68**(3), 417 – 422.

Farquharson, C. G., 2008. Constructing piecewise-constant models in multidimensional minimum-structure inversions, *Geophysics*, **73**(1), K1–K9.

Farquharson, C. G. & Miensopust, M. P., 2011. Three-dimensional finite-element modelling of magnetotelluric data with a divergence correction, *Journal of Applied Geophysics*, **75**(4), 699–710.

Fasshauer, G. E., 1996. Solving partial differential equations by collocation with radial basis functions, in *Proceedings of Chamonix*, vol. 1997, pp. 1–8, Vanderbilt University Press Nashville, TN.

Fasshauer, G. E., 2007. *Meshfree Approximation Methods with Matlab*, vol. 6 of **Interdisciplinary Mathematical Sciences**, World Scientific.

Fasshauer, G. E. & McCourt, M. J., 2012. Stable Evaluation of Gaussian Radial Basis Function Interpolants, *SIAM Journal on Scientific Computing*, **34**(2), A737–A762.

Fasshauer, G. E. & Zhang, J. G., 2007. On choosing "optimal" shape parameters for RBF approximation, *Numerical Algorithms*, **45**(1-4), 345–368.

Flyer, N., Barnett, G. A., & Wicker, L. J., 2016a. Enhancing finite differences with radial basis functions: Experiments on the Navier–Stokes equations, *Journal of Computational Physics*, **316**, 39–62.

Flyer, N., Fornberg, B., Bayona, V., & Barnett, G. A., 2016b. On the role of polynomials in RBF-FD approximations: I. Interpolation and accuracy, *Journal of Computational Physics*, **321**, 21–38.

Fornberg, B. & Flyer, N., 2015a. *A primer on radial basis functions with applications to the geosciences*, SIAM.

Fornberg, B. & Flyer, N., 2015b. Fast generation of 2-D node distributions for mesh-free PDE discretizations, *Computers & Mathematics with Applications*, **69**(7), 531–544.

Fornberg, B. & Piret, C., 2007. A stable algorithm for flat radial basis functions on a sphere, *SIAM Journal on Scientific Computing*, **30**(1), 60–80.

Fornberg, B. & Wright, G., 2004. Stable computation of multiquadric interpolants for all values of the shape parameter, *Computers & Mathematics with Applications*, **48**(5-6), 853–867.

Fornberg, B., Driscoll, T. A., Wright, G., & Charles, R., 2002. Observations on the behavior of radial basis function approximations near boundaries, *Computers &*

Mathematics with Applications, **43**(3-5), 473–490.

Fornberg, B., Larsson, E., & Flyer, N., 2011. Stable Computations with Gaussian Radial Basis Functions, *SIAM Journal on Scientific Computing*, **33**(2), 869–892.

Fornberg, B., Lehto, E., & Powell, C., 2013. Stable calculation of Gaussian-based RBF-FD stencils, *Computers & Mathematics with Applications*, **65**(4), 627–637.

Franke, A., Börner, R.-U., & Spitzer, K., 2007. Adaptive unstructured grid finite element simulation of two-dimensional magnetotelluric fields for arbitrary surface and seafloor topography, *Geophysical Journal International*, **171**(1), 71–86.

Franke, C. & Schaback, R., 1998. Solving partial differential equations by collocation using radial basis functions, *Applied Mathematics and Computation*, **93**(1), 73–82.

Fullagar, P. & Pears, G., 2007. Towards geologically realistic inversion, in *Proceeding of the 5th Decennial International Conference on Mineral Exploration*, vol. 7, pp. 444–460.

Gingold, R. A. & Monaghan, J. J., 1977. Smoothed particle hydrodynamics: theory and application to non-spherical stars, *Monthly notices of the royal astronomical society*, **181**(3), 375–389.

Gockenbach, M. S., 2006. *Understanding and implementing the finite element method*, vol. 97, SIAM.

Grayver, A. V. & Burg, M., 2014. Robust and scalable 3-D geo-electromagnetic modelling approach using the finite element method, *Geophysical Journal International*, **198**(1), 110–125.

Gross, L., Altinay, C., & Shaw, S., 2015. Inversion of potential field data using the finite element method on parallel computers, *Computers & Geosciences*, **84**, 61–71.

Guillen, A. & Menichetti, V., 1984. Gravity and magnetic inversion with minimization of a specific functional, *Geophysics*, **49**(8), 1354–1360.

Günther, T., Rücker, C., & Spitzer, K., 2006. Three-dimensional modelling and inversion of DC resistivity data incorporating topography-II. Inversion, *Geophysical Journal International*, **166**(2), 506–517.

Haber, E. & Heldmann, S., 2007. An octree multigrid method for quasi-static Maxwell's equations with highly discontinuous coefficients, *Journal of Computational Physics*, **223**(2), 783–796.

Haber, E., Holtham, E., & Davis, K., 2014. Large-scale inversion of gravity gradiom-

etry with differential equations, in *SEG Technical Program Expanded Abstracts 2014*, pp. 1302–1307, Society of Exploration Geophysicists.

Hansen, R., 1999. An analytical expression for the gravity field of a polyhedral body with linearly varying density, *Geophysics*, **64**(1), 75–77.

Hardy, R. L., 1971. Multiquadric equations of topography and other irregular surfaces, *Journal of Geophysical Research*, **76**(8), 1905–1915.

Harrington, R. F., 2001. *Time-harmonic electromagnetic fields*, IEEE press series on electromagnetic wave theory, John Wiley & Sons, Piscataway, NJ.

Herault, C. & Marechal, Y., 1999. Boundary and interface conditions in meshless methods [for EM field analysis], *IEEE Transactions on Magnetics*, **35**(3), 1450–1453.

Hillman, M. & Chen, J.-S., 2016. An accelerated, convergent, and stable nodal integration in Galerkin meshfree methods for linear and nonlinear mechanics, *International Journal for Numerical Methods in Engineering*, **107**(7), 603–630.

Hohmann, G. W., 1975. Three-dimensional induced polarization and electromagnetic modeling, *Geophysics*, **40**(2), 309–324.

Hohmann, G. W., 1983. Three-dimensional EM modeling, *Geophysical Surveys*, **6**(1-2), 27–53.

Holstein, H., 2002. Gravimagnetic similarity in anomaly formulas for uniform polyhedra, *Geophysics*, **67**(4), 1126–1133.

Holstein, H., 2003. Gravimagnetic anomaly formulas for polyhedra of spatially linear media, *Geophysics*, **68**(1), 157–167.

Iske, A., 2003. On the approximation order and numerical stability of local Lagrange interpolation by polyharmonic splines, *Modern Developments in Multivariate Approximation: Fifth International Series of Numerical Mathematics*, pp. 153–166.

Jahandari, H., 2015. *Three-dimensional numerical modelling of gravity and electromagnetic data using unstructured tetrahedral grids*, Ph.D. thesis, Memorial University of Newfoundland.

Jahandari, H. & Farquharson, C., 2017. 3-D minimum-structure inversion of magnetotelluric data using the finite-element method and tetrahedral grids, *Geophysical Journal International*, **211**(2), 1189–1205.

Jahandari, H. & Farquharson, C. G., 2013. Forward modeling of gravity data using

finite-volume and finite-element methods on unstructured grids, *Geophysics*, **78**(3), G69–G80.

Jahandari, H. & Farquharson, C. G., 2014. A finite-volume solution to the geophysical electromagnetic forward problem using unstructured grids, *Geophysics*, **79**(6), E287–E302.

Jahandari, H. & Farquharson, C. G., 2015. Finite-volume modelling of geophysical electromagnetic data on unstructured grids using potentials, *Geophysical Journal International*, **202**(3), 1859–1876.

Jalušić, B., Sorić, J., & Jarak, T., 2017. Mixed meshless local Petrov-Galerkin collocation method for modeling of material discontinuity, *Computational mechanics*, **59**(1), 1–19.

Ji, Y., Huang, T., Huang, W., & Rong, L., 2018. Meshfree method in geophysical electromagnetic prospecting: the 2D magnetotelluric example, *International Journal of Computational Methods*, **15**(02), 1750084.

Jia, X. & Hu, T., 2006. Element-free precise integration method and its applications in seismic modelling and imaging, *Geophysical Journal International*, **166**(1), 349–372.

Jin, J.-M., 2014. *The finite element method in electromagnetics*, John Wiley & Sons, 3rd edn.

Jones, F. W. & Pascoe, L. J., 1972. The perturbation of alternating geomagnetic fields by three-dimensional conductivity inhomogeneities, *Geophysical Journal International*, **27**(5), 479–485.

Joyot, P., Trunzler, J., & Chinesta, F., 2005. Enriched reproducing kernel approximation: Reproducing functions with discontinuous derivatives, in *Meshfree Methods for Partial Differential Equations II*, pp. 93–107, Springer.

Jurgens, T. G., Taflove, A., Umashankar, K., & Moore, T. G., 1992. Finite-difference time-domain modeling of curved surfaces (EM scattering), *IEEE Transactions on Antennas and Propagation*, **40**(4), 357–366.

Kansa, E., 1990a. Multiquadrics-A scattered data approximation scheme with applications to computational fluid-dynamics - I:surface approximations and partial derivative estimates, *Computers and Mathematics with Applications*, **19**(8-9), 127–145.

Kansa, E., 1990b. Multiquadrics-A scattered data approximation scheme with ap-

plications to computational fluid-dynamics -II: solutions to parabolic, hyperbolic and elliptic partial differential equations, *Computers and Mathematics with Applications*, **19**(8-9), 147–161.

Kellogg, O. D., 1967. *Foundations of potential theory*, vol. 31, Springer Science & Business Media.

Key, K. & Ovall, J., 2011. A parallel goal-oriented adaptive finite element method for 2.5-D electromagnetic modelling, *Geophysical Journal International*, **186**(1), 137–154.

Kordy, M., Wannamaker, P., Maris, V., Cherkaev, E., & Hill, G., 2016. 3-D magnetotelluric inversion including topography using deformed hexahedral edge finite elements and direct solvers parallelized on SMP computers - Part I: forward problem and parameter Jacobians, *Geophysical Journal International*, **204**(1), 74–93.

Krongauz, Y. & Belytschko, T., 1998. EFG approximation with discontinuous derivatives, *International journal for numerical methods in engineering*, **41**(7), 1215–1233.

Larsson, E. & Fornberg, B., 2003. A numerical study of some radial basis function based solution methods for elliptic PDEs, *Computers & Mathematics with Applications*, **46**(5-6), 891–902.

Larsson, E., Lehto, E., Heryudono, A., & Fornberg, B., 2013. Stable computation of differentiation matrices and scattered node stencils based on Gaussian radial basis functions, *SIAM Journal on Scientific Computing*, **35**(4), A2096–A2119.

Last, B. & Kubik, K., 1983. Compact gravity inversion, *Geophysics*, **48**(6), 713–721.

Lelièvre, P. G. & Farquharson, C. G., 2016. Integrated imaging for mineral exploration, *Integrated imaging of the earth: theory and applications. Wiley*, pp. 137–166.

Lelièvre, P. G., Zheglova, P., Danek, T., & Farquharson, C. G., 2012. Geophysical inversion for contact surfaces, in *SEG Technical Program Expanded Abstracts 2012*, pp. 1–5, Society of Exploration Geophysicists.

Lelièvre, P. G., Farquharson, C. G., & Butler, K., 2016. Inversion for wireframe surface geometry applied to the Cocagne Subbasin, New Brunswick, Canada, in *SEG Technical Program Expanded Abstracts 2016*, pp. 1617–1621, Society of Exploration Geophysicists.

Leonard, A., 1985. Computing three-dimensional incompressible flows with vortex elements, *Annual Review of Fluid Mechanics*, **17**(1), 523–559.

Li, B., Liu, Y., Sen, M. K., & Ren, Z., 2017. Time-space-domain mesh-free finite difference based on least squares for 2D acoustic-wave modeling, *Geophysics*, **82**(4), T143–T157.

Li, J.-J., Yan, J.-B., & Huang, X.-Y., 2015. Precision of meshfree methods and application to forward modeling of two-dimensional electromagnetic sources, *Applied Geophysics*, **12**(4), 503–515.

Li, Q., Shen, S., Han, Z., & Atluri, S., 2003. Application of meshless local Petrov-Galerkin (MLPG) to problems with singularities, and material discontinuities, in 3-D elasticity, *Computer Modeling in Engineering and Sciences*, **4**(5), 571–586.

Li, S. & Liu, W. K., 2002. Meshfree and particle methods and their applications, *Applied Mechanics Reviews*, **55**(1), 1–34.

Li, X. & Chouteau, M., 1998. Three-dimensional gravity modeling in all space, *Surveys in Geophysics*, **19**(4), 339–368.

Li, Y. & Key, K., 2007. 2D marine controlled-source electromagnetic modeling: Part 1-An adaptive finite-element algorithm, *Geophysics*, **72**(2), WA51–WA62.

Li, Y. & Oldenburg, D. W., 1998. 3-D inversion of gravity data, *Geophysics*, **63**(1), 109–119.

Li, Y. & Oldenburg, D. W., 2003. Fast inversion of large-scale magnetic data using wavelet transforms and a logarithmic barrier method, *Geophysical Journal International*, **152**(2), 251–265.

Lima, N. Z., Fonseca, A. R., & Mesquita, R. C., 2012. Application of local point interpolation method to electromagnetic problems with material discontinuities using a new visibility criterion, *IEEE Transactions on Magnetics*, **48**(2), 615–618.

Liszka, T. & Orkisz, J., 1980. The finite difference method at arbitrary irregular grids and its application in applied mechanics, *Computers and Structures*, **11**(1-2), 83–95.

Liu, C., Ren, Z., Tang, J., & Yan, Y., 2008. Three-dimensional magnetotellurics modeling using edge-based finite-element unstructured meshes, *Applied Geophysics*, **5**(3), 170–180.

Liu, W. K., Jun, S., & Zhang, Y. F., 1995. Reproducing kernel particle methods, *International journal for numerical methods in fluids*, **20**(8-9), 1081–1106.

Long, J. & Farquharson, C. G., 2017. Three-dimensional controlled-source EM mod-

eling with radial basis function-generated finite differences: A meshless approach, in *SEG Technical Program Expanded Abstracts 2017*, pp. 1209–1213, Society of Exploration Geophysicists.

Long, J. & Farquharson, C. G., 2019a. Three-dimensional forward modelling of gravity data using mesh-free methods with radial basis functions and unstructured nodes, *Geophysical Journal International*, **217**(3), 1577–1601.

Long, J. & Farquharson, C. G., 2019b. Meshfree modelling of 3-D controlled-source EM data: A new method to treat the singular source terms, in *SEG Technical Program Expanded Abstracts 2019*, pp. 1050–1054, Society of Exploration Geophysicists.

Long, J. & Farquharson, C. G., 2019c. On the forward modelling of three-dimensional magnetotelluric data using a radial-basis-function-based mesh-free method, *Geophysical Journal International*, **219**(1), 394–416.

Mackie, R. L., Madden, T. R., & Wannamaker, P. E., 1993. Three-dimensional magnetotelluric modeling using difference equations—Theory and comparisons to integral equation solutions, *Geophysics*, **58**(2), 215–226.

Mackie, R. L., Smith, J. T., & Madden, T. R., 1994. Three-dimensional electromagnetic modeling using finite difference equations: The magnetotelluric example, *Radio Science*, **29**(4), 923–935.

Martin, B., Fornberg, B., & St-Cyr, A., 2015. Seismic modeling with radial-basis-function-generated finite differences, *Geophysics*, **80**(4), T137–T146.

May, D. A. & Knepley, M. G., 2011. Optimal, scalable forward models for computing gravity anomalies, *Geophysical Journal International*, **187**(1), 161–177.

McGaughey, J., 2007. Geological models, rock properties, and the 3D inversion of geophysical data, in *Proceeding of the 5th Decennial International Conference on Mineral Exploration*, vol. 7, pp. 473–483.

Melenk, J. M. & Babuška, I., 1996. The partition of unity finite element method: basic theory and applications, *Computer methods in applied mechanics and engineering*, **139**(1-4), 289–314.

Miensopust, M. P., Queralt, P., Jones, A. G., & the 3D MT modellers, 2013. Magnetotelluric 3-D inversion-a review of two successful workshops on forward and inversion code testing and comparison, *Geophysical Journal International*, **193**(3), 1216–1238.

Moorkamp, M., Heincke, B., Jegen, M., Roberts, A. W., & Hobbs, R. W., 2011. A framework for 3-D joint inversion of MT, gravity and seismic refraction data, *Geophysical Journal International*, **184**(1), 477–493.

Morisue, T., 1982. Magnetic vector potential and electric scalar potential in three-dimensional eddy current problem, *IEEE Transactions on magnetics*, **18**(2), 531–535.

Munz, C.-D., Schneider, R., Sonnendrücker, E., Stein, E., Voss, U., & Westermann, T., 1999. A finite-volume particle-in-cell method for the numerical treatment of Maxwell-Lorentz equations on boundary-fitted meshes, *International journal for numerical methods in engineering*, **44**(4), 461–487.

ed. Nabighian, M. N., 1988. *Electromagnetic Methods in Applied Geophysics: Volume 1, Theory*, Society of Exploration Geophysicists.

ed. Nabighian, M. N., 1991. *Electromagnetic Methods in Applied Geophysics: Volume 2, Application, Parts A and B*, Society of Exploration Geophysicists.

Nabighian, M. N. & Asten, M. W., 2002. Metalliferous mining geophysics-state of the art in the last decade of the 20th century and the beginning of the new millennium, *Geophysics*, **67**(3), 964–978.

Nagy, D., 1966. The gravitational attraction of a right rectangular prism, *Geophysics*, **31**(2), 362–371.

Nalepa, M., 2016. *Synthetic modelling study of marine controlled-source electromagnetic data for hydrocarbon exploration*, Master's thesis, Memorial University of Newfoundland.

Nalepa, M., Ansari, S., & Farquharson, C., 2016. Finite-element simulation of 3D CSEM data on unstructured meshes: An example from the East Coast of Canada, in *SEG Technical Program Expanded Abstracts 2016*, pp. 1048–1052, Society of Exploration Geophysicists.

Nam, M. J., Kim, H. J., Song, Y., Lee, T. J., Son, J.-S., & Suh, J. H., 2007. 3D magnetotelluric modelling including surface topography, *Geophysical Prospecting*, **55**(2), 277–287.

Nayroles, B., Touzot, G., & Villon, P., 1992. Generalizing the finite element method: diffuse approximation and diffuse elements, *Computational mechanics*, **10**(5), 307–318.

Newman, G. A., 2014. A review of high-performance computational strategies for

modeling and imaging of electromagnetic induction data, *Surveys in Geophysics*, **35**(1), 85–100.

Newman, G. A. & Alumbaugh, D. L., 1995. Frequency-domain modelling of airborne electromagnetic responses using staggered finite differences, *Geophysical Prospecting*, **43**(8), 1021–1042.

Newman, G. A., Hohmann, G. W., & Anderson, W. L., 1986. Transient electromagnetic response of a three-dimensional body in a layered earth, *Geophysics*, **51**(8), 1608–1627.

Nguyen, V. P., Rabczuk, T., Bordas, S., & Duflot, M., 2008. Meshless methods: A review and computer implementation aspects, *Mathematics and Computers in Simulation*, **79**(3), 763–813.

Nicomedes, W. L., Mesquita, R. C., & Moreira, F. J., 2011. A meshless local Petrov-Galerkin method for three-dimensional scalar problems, *IEEE Transactions on Magnetics*, **47**(5), 1214–1217.

Oden, J. T. & Prudhomme, S., 2001. Goal-oriented error estimation and adaptivity for the finite element method, *Computers and mathematics with applications*, **41**(5), 735–756.

Okabe, M., 1979. Analytical expressions for gravity anomalies due to homogeneous polyhedral bodies and translations into magnetic anomalies, *Geophysics*, **44**(4), 730–741.

Oldenburg, D. & Pratt, D., 2007. Geophysical inversion for mineral exploration: a decade of progress in theory and practice, in *Proceedings of exploration*, vol. 7, pp. 61–95.

Parker, R. L., 1977. Understanding inverse theory, *Annual Review of Earth and Planetary Sciences*, **5**(1), 35–64.

Paul, M., 1974. The gravity effect of a homogeneous polyhedron for three-dimensional interpretation, *Pure and Applied Geophysics*, **112**(3), 553–561.

Pears, G. & Chalke, T., 2016. Geological and geophysical integrated interpretation and modelling techniques, in *ASEG Extended Abstracts 2016: 25th International Geophysical Conference and Exhibition*, pp. 793–799, Australian Society of Exploration Geophysicists.

Pellerin, L., 2002. Applications of electrical and electromagnetic methods for environmental and geotechnical investigations, *Surveys in Geophysics*, **23**(2-3), 101–132.

Petrović, S., 1996. Determination of the potential of homogeneous polyhedral bodies using line integrals, *Journal of Geodesy*, **71**(1), 44–52.

Pilkington, M., 2009. 3D magnetic data-space inversion with sparseness constraints, *Geophysics*, **74**(1), L7–L15.

Pohánka, V., 1988. Optimum expression for computation of the gravity field of a homogeneous polyhedral body, *Geophysical Prospecting*, **36**(7), 733–751.

Pohánka, V., 1998. Optimum expression for computation of the gravity field of a polyhedral body with linearly increasing density, *Geophysical Prospecting*, **46**(4), 391–404.

Pridmore, D., Hohmann, G., Ward, S., & Sill, W., 1981. An investigation of finite-element modeling for electrical and electromagnetic data in three dimensions, *Geophysics*, **46**(7), 1009–1024.

Puzyrev, V., Koldan, J., de la Puente, J., Houzeaux, G., Vazquez, M., & Cela, J. M., 2013. A parallel finite-element method for three-dimensional controlled-source electromagnetic forward modelling, *Geophysical Journal International*, **193**(2), 678–693.

Rabczuk, T. & Belytschko, T., 2005. Adaptivity for structured meshfree particle methods in 2D and 3D, *International Journal for Numerical Methods in Engineering*, **63**(11), 1559–1582.

Ren, Z., Kalscheuer, T., Greenhalgh, S., & Maurer, H., 2013. A goal-oriented adaptive finite-element approach for plane wave 3-D electromagnetic modelling, *Geophysical Journal International*, **194**(2), 700–718.

Ren, Z., Chen, C., Pan, K., Kalscheuer, T., Maurer, H., & Tang, J., 2017a. Gravity anomalies of arbitrary 3D polyhedral bodies with horizontal and vertical mass contrasts, *Surveys in geophysics*, **38**(2), 479–502.

Ren, Z., Tang, J., Kalscheuer, T., & Maurer, H., 2017b. Fast 3-D large-scale gravity and magnetic modeling using unstructured grids and an adaptive multilevel fast multipole method, *Journal of Geophysical Research: Solid Earth*, **122**(1), 79–109.

Rippa, S., 1999. An algorithm for selecting a good value for the parameter c in radial basis function interpolation, *Advances in Computational Mathematics*, **11**(2), 193–210.

Saad, Y., 2003. *Iterative methods for sparse linear systems*, vol. 8, SIAM.

Schaback, R., 1995. Error estimates and condition numbers for radial basis function interpolation, *Advances in Computational Mathematics*, **3**(3), 251–264.

Schaback, R., 2007. Convergence of unsymmetric kernel-based meshless collocation methods, *SIAM Journal on Numerical Analysis*, **45**(1), 333–351.

Schaback, R., 2017. Error analysis of nodal meshless methods, in *Meshfree Methods for Partial Differential Equations VIII*, pp. 117–143, Springer.

Schaback, R. & Wendland, H., 1999. Using compactly support radial basis functions to solve partial differential equations, *Boundary Element Technology*, **13**, 311–324.

Schwarzbach, C., Börner, R.-U., & Spitzer, K., 2011. Three-dimensional adaptive higher order finite element simulation for geo-electromagnetics-a marine CSEM example, *Geophysical Journal International*, **187**(1), 63–74.

Shewchuk, J., 1996. Triangle: Engineering a 2D quality mesh generator and Delaunay triangulator, *Applied computational geometry towards geometric engineering*, pp. 203–222.

Shu, C., Ding, H., & Yeo, K., 2003. Local radial basis function-based differential quadrature method and its application to solve two-dimensional incompressible Navier-Stokes equations, *Computer Methods in Applied Mechanics and Engineering*, **192**(7-8), 941–954.

Si, H., 2015. TetGen, a Delaunay-Based Quality Tetrahedral Mesh Generator, *ACM Transactions on Mathematical Software*, **41**(2), 1–36.

Siripunvaraporn, W., Egbert, G., & Lenbury, Y., 2002. Numerical accuracy of magnetotelluric modeling: a comparison of finite difference approximations, *Earth, planets and space*, **54**(6), 721–725.

Slak, J. & Kosec, G., 2019. On generation of node distributions for meshless PDE discretizations, *SIAM Journal on Scientific Computing*, **41**(5), A3202–A3229.

Spies, B. R. & Frischknecht, F. C., 1991. Electromagnetic sounding, in *Electromagnetic Methods in Applied Geophysics*, chap. 5, pp. 285–425, ed. Nabighian, M. N., Society of Exploration Geophysicists.

Stratton, J. A., 2007. *Electromagnetic theory*, John Wiley & Sons.

Streich, R., 2009. 3D finite-difference frequency-domain modeling of controlled-source electromagnetic data: Direct solution and optimization for high accuracy, *Geophysics*, **74**(5), F95–F105.

Taflove, A. & Umashankar, K. R., 1990. The finite-difference time-domain method for numerical modeling of electromagnetic wave interactions, *Electromagnetics*, **10**(1-2), 105–126.

Takekawa, J. & Mikada, H., 2016. An absorbing boundary condition for acoustic-wave propagation using a mesh-free method, *Geophysics*, **81**(4), T145–T154.

Takekawa, J. & Mikada, H., 2018. A mesh-free finite-difference method for elastic wave propagation in the frequency-domain, *Computers & Geosciences*.

Takekawa, J., Mikada, H., & Imamura, N., 2015. A mesh-free method with arbitrary-order accuracy for acoustic wave propagation, *Computers & Geosciences*, **78**, 15–25.

Tarantola, A. & Valette, B., 1982. Inverse problems = quest for information, *Journal of geophysics*, **50**(3), 150–170.

Tolstykh, A. & Shirobokov, D., 2003. On using radial basis functions in a "finite difference mode" with applications to elasticity problems, *Computational Mechanics*, **33**(1), 68–79.

Tsoulis, D., 2012. Analytical computation of the full gravity tensor of a homogeneous arbitrarily shaped polyhedral source using line integrals, *Geophysics*, **77**(2), F1–F11.

Uddin, M., 2014. On the selection of a good value of shape parameter in solving time-dependent partial differential equations using RBF approximation method, *Applied Mathematical Modelling*, **38**(1), 135–144.

Um, E. S., Commer, M., Newman, G. A., & Hoversten, G. M., 2015. Finite element modelling of transient electromagnetic fields near steel-cased wells, *Geophysical Journal International*, **202**(2), 901–913.

Usui, Y., 2015. 3-D inversion of magnetotelluric data using unstructured tetrahedral elements: applicability to data affected by topography, *Geophysical Journal International*, **202**(2), 828–849.

Usui, Y., Ogawa, Y., Aizawa, K., Kanda, W., Hashimoto, T., Koyama, T., Yamaya, Y., & Kagiyama, T., 2017. Three-dimensional resistivity structure of Asama Volcano revealed by data-space magnetotelluric inversion using unstructured tetrahedral elements, *Geophysical Journal International*, **208**(3), 1359–1372.

Vallée, M. A., 2015. New developments in AEM discrete conductor modelling and inversion, *Exploration Geophysics*, **46**(1), 97–111.

Waldvogel, J., 1976. The Newtonian potential of a homogeneous cube, *Zeitschrift für angewandte Mathematik und Physik ZAMP*, **27**(6), 867–871.

Waldvogel, J., 1979. The Newtonian potential of homogeneous polyhedra, *Zeitschrift für Angewandte Mathematik und Physik (ZAMP)*, **30**(2), 388–398.

Wang, F., Morten, J. P., & Spitzer, K., 2018. Anisotropic three-dimensional inversion of CSEM data using finite-element techniques on unstructured grids, *Geophysical Journal International*, **213**(2), 1056–1072.

Wang, J. G. & Liu, G. R., 2002a. A point interpolation meshless method based on radial basis functions, *International Journal for Numerical Methods in Engineering*, **54**(11), 1623–1648.

Wang, J. G. & Liu, G. R., 2002b. On the optimal shape parameters of radial basis functions used for 2-D meshless methods, *Computer methods in applied mechanics and engineering*, **191**(23), 2611–2630.

Wang, T. & Hohmann, G. W., 1993. A finite-difference, time-domain solution for three-dimensional electromagnetic modeling, *Geophysics*, **58**(6), 797–809.

Wannamaker, P. E., 1991. Advances in three-dimensional magnetotelluric modeling using integral equations, *Geophysics*, **56**(11), 1716–1728.

Ward, S. H. & Hohmann, G. W., 1988. Electromagnetic theory for geophysical applications, in *Electromagnetic Methods in Applied Geophysics: Voume 1, Theory*, pp. 130–311, Society of Exploration Geophysicists.

Weaver, J. T., 1994. *Mathematical methods for geo-electromagnetic induction*, Research Studies Press.

Weiss, C. J. & Constable, S., 2006. Mapping thin resistors and hydrocarbons with marine EM methods, Part II-Modeling and analysis in 3D, *Geophysics*, **71**(6), G321–G332.

Wittke, J. & Tezkan, B., 2014. Meshfree magnetotelluric modelling, *Geophysical Journal International*, **198**(2), 1255–1268.

Wright, G. B., 2003. *Radial basis function interpolation: numerical and analytical developments*, Ph.D. thesis, University of Colorado at Boulder.

Wright, G. B. & Fornberg, B., 2006. Scattered node compact finite difference-type formulas generated from radial basis functions, *Journal of Computational Physics*, **212**(1), 99–123.

Wright, G. B., Flyer, N., & Yuen, D. A., 2010. A hybrid radial basis function–pseudospectral method for thermal convection in a 3-D spherical shell, *Geochemistry, Geophysics, Geosystems*, **11**(7).

Wu, Y. & Liu, G., 2003. A meshfree formulation of local radial point interpolation method (LRPIM) for incompressible flow simulation, *Computational Mechanics*, **30**(5-6), 355–365.

Xu, J. & Belytschko, T., 2005. Discontinuous radial basis function approximations for meshfree methods, in *Meshfree methods for partial differential equations II*, pp. 231–253, Springer.

Yagawa, G. & Yamada, T., 1996. Free mesh method: a new meshless finite element method, *Computational Mechanics*, **18**(5), 383–386.

Yee, K. S., 1966. Numerical solution of initial boundary value problems involving Maxwell's equations in isotropic media, *IEEE Transactions on Antennas and Propagation*, **14**(3), 302–307.

Yu, Y. & Chen, Z., 2011. Implementation of material interface conditions in the radial point interpolation meshless method, *IEEE Transactions on Antennas and Propagation*, **59**(8), 2916–2923.

Zhang, J., Wang, C.-Y., Shi, Y., Cai, Y., Chi, W.-C., Dreger, D., Cheng, W.-B., & Yuan, Y.-H., 2004. Three-dimensional crustal structure in central Taiwan from gravity inversion with a parallel genetic algorithm, *Geophysics*, **69**(4), 917–924.

Zhdanov, M., Varentsov, I., Weaver, J., Golubev, N., & Krylov, V., 1997. Methods for modelling electromagnetic fields results from COMMEMI-the international project on the comparison of modelling methods for electromagnetic induction, *Journal of Applied Geophysics*, **37**(3-4), 133–271.

Zhdanov, M. S., 2009. *Geophysical electromagnetic theory and methods*, vol. 43, Elsevier.

Zhou, X., 2009. 3D vector gravity potential and line integrals for the gravity anomaly of a rectangular prism with 3D variable density contrast, *Geophysics*, **74**(6), I43–I53.

Appendices

Appendix A

Differentiability of 3-D PHS RBFs

In the 3-D case, the Euclidean distance from a position (x_0, y_0, z_0) is

$$r = \sqrt{(x - x_0)^2 + (y - y_0)^2 + (z - z_0)^2}, \tag{A.1}$$

which is also the expression of a linear polyharmonic (PHS) RBF with its centre at (x_0, y_0, z_0). To see the differentiability of the linear PHS RBFs up to second order, it is sufficient to examine the following derivatives

$$\begin{cases} dr/dx = \frac{x-x_0}{r}, \quad dr/dy = \frac{y-y_0}{r}, \quad dr/dz = \frac{z-z_0}{r}, \\ d^2r/dx^2 = \frac{r-(x-x_0)*(dr/dx)}{r^2} = \frac{r-(x-x_0)^2/r}{r^2} = \frac{r^2-(x-x_0)^2}{r^3} = \frac{(y-y_0)^2+(z-z_0)^2}{r^3}, \\ d^2r/dy^2 = \frac{(x-x_0)^2+(z-z_0)^2}{r^3}, \\ d^2r/dz^2 = \frac{(x-x_0)^2+(y-y_0)^2}{r^3}, \\ \nabla^2 r = d^2r/dx^2 + d^2r/dy^2 + d^2r/dz^2 = \frac{2}{r}. \end{cases} \tag{A.2}$$

Similarly, for cubic PHS RBFs $P = r^3$, we have

$$\begin{cases} \nabla P = 3r^2 \nabla r = 3r^2[\frac{x-x_0}{r}, \frac{y-y_0}{r}, \frac{z-z_0}{r}] = 3r[x-x_0, y-y_0, z-z_0], \\ dP/dx^2 = d(dP/dx)/dx = 3[dr/dx * (x-x_0) + r] = 3[\frac{(x-x_0)^2}{r} + r], \\ \nabla^2 P = d^2P/dx^2 + d^2P/dy^2 + d^2P/dz^2 = 12r. \end{cases} \tag{A.3}$$

For quintic PHS RBFs $Q = r^5$, we have

$$\begin{cases} \nabla Q = 5r^4 \nabla r = 5r^3[x-x_0, y-y_0, z-z_0], \\ d^2Q/dx^2 = d(dQ/dx)/dx = 5[(x-x_0)dP/dx + r^3] = 5[3r(x-x_0)^2 + r^3], \\ \nabla^2 Q = d^2Q/dx^2 + d^2Q/dy^2 + d^2Q/dz^2 = 30r^3. \end{cases} \tag{A.4}$$

Note that $1/r$ has singularities at the centre (x_0, y_0, z_0), therefore only the quintic PHS RBFs are completely free of singularities in the derivatives up to second order. For the cubic PHS RBFs, although their Laplacian derivatives are continuous, they have singularities in their second-order partial derivatives and thus cannot approximate all differential operators in the EM modelling problem.

Appendix B

Implied divergence condition $\nabla \cdot \mathbf{A} = 0$

In the Coulomb gauged $\mathbf{A}$-ψ system, the pair of eqs (4.15) and (4.13), which is re-written here for convenience as

$$-\nabla^2 \mathbf{A} + i\omega\mu\sigma\mathbf{A} + \sigma\mu\nabla\psi = \mathbf{0}, \tag{B.1}$$

$$\nabla \cdot (i\omega\mu\sigma\mathbf{A} + \sigma\mu\nabla\psi) = 0, \tag{B.2}$$

is numerically solved. Following the discussions of Morisue (1982) and Biro & Preis (1989), taking the divergence of eq (B.1) and subtracting eq (B.2) from it results in

$$\nabla^2(\nabla \cdot \mathbf{A}) = 0. \tag{B.3}$$

Eq (B.3) indicates that $\nabla \cdot \mathbf{A}$ satisfies Laplace's equation in the computational domain, or equivalently, $\nabla \cdot \mathbf{A}$ is a harmonic function. It is well known that for a harmonic function f, if $f = 0$ holds at the computational boundaries, then it also holds everywhere within the computational domain. This means that the divergence condition $\nabla \cdot \mathbf{A} = 0$ will be implicitly imposed everywhere within the computational domain for a numerical solution if it is satisfied at the boundaries. The condition

$\nabla \cdot \mathbf{A} = 0$ at the boundaries is fulfilled by using Dirichlet boundary conditions for $\mathbf{A}$ and ψ with 1-D background models in which the boundary is far from inhomogeneities of the model.

Appendix C

Formulation for computing 1-D MT boundary values

In the case of 1-D conductivity models, the EM fields in the MT method propagate downwards in the subsurface as a plane wave. When the 1-D model consists of only an air layer (the air conductivity is approximated as the small value 10^{-8} S/m) and a uniform subsurface, which is so-called half space model, the analytical formulations from Weaver (1994, eqs 2.211-2.213)

$$f(z) = -\frac{1}{\alpha\sqrt{i}} \begin{cases} 1 + z\alpha\sqrt{i} & (0 \leqslant z < h_s) \\ e^{z\alpha\sqrt{i}} & (z < 0) \end{cases}, \tag{C.1}$$

and

$$E_x = -2i\omega B_0 f(z), \tag{C.2}$$

are used to compute the **E** field under the E-x mode which is regarded as boundary values on the computational boundaries of 3-D models. In eqs (C.1) and (C.2), the $+z$ direction is upwards in the Cartesian coordinate system. The air layer ($0 < z < h_s$) has a thickness of h_s. The air-Earth surface of the half space model is located at $z = 0$. $\alpha = \sqrt{\omega\mu\sigma_s}$ and σ_s is the conductivity of the subsurface, with i, ω and

μ already defined in the text in Section 4.2. B_0 is the initial magnetic induction amplitude at the top of the computational domain, i.e., at $z = h_s$ in this case. B_0 is set to be μI_0 with the predefined current intensity $I_0 = 1.0$ A for all numerical examples ($B_0 > 0$ can be set to be any positive numeric values without affecting the MT impedance computation). It is noted that E_x only depends on z and is uniform in the x-y plane. The computation of the electric field under E-y mode is exactly the same as above, but with E_x being replaced by E_y.

For a n-layer ($n > 2$) 1-D conductivity model, the analytical formulae in Ward & Hohmann (1988, p194 - p197) are used to compute the electric field at an arbitrary position. The process comprises the following basic steps:

1. Compute characteristic impedance within each layer and the apparent impedance at the top interface of the 1-D model.

2. Compute E_x (and H_y) fields at subsequent interfaces of the 1-D model using the recursive relations therein, for a chosen initial E_x value at the top interface (At this interface, if E_x (or H_y) is given, then H_y (or E_x) can be determined using the apparent impedance).

3. Calculate E_x field at an arbitrary position between two consecutive interfaces using the field decomposition formula for a Helmholtz solution (Ward & Hohmann, 1988, p195, eq 3.101).

Appendix D

Additional plots for MT COMMEMI 3D-1A model

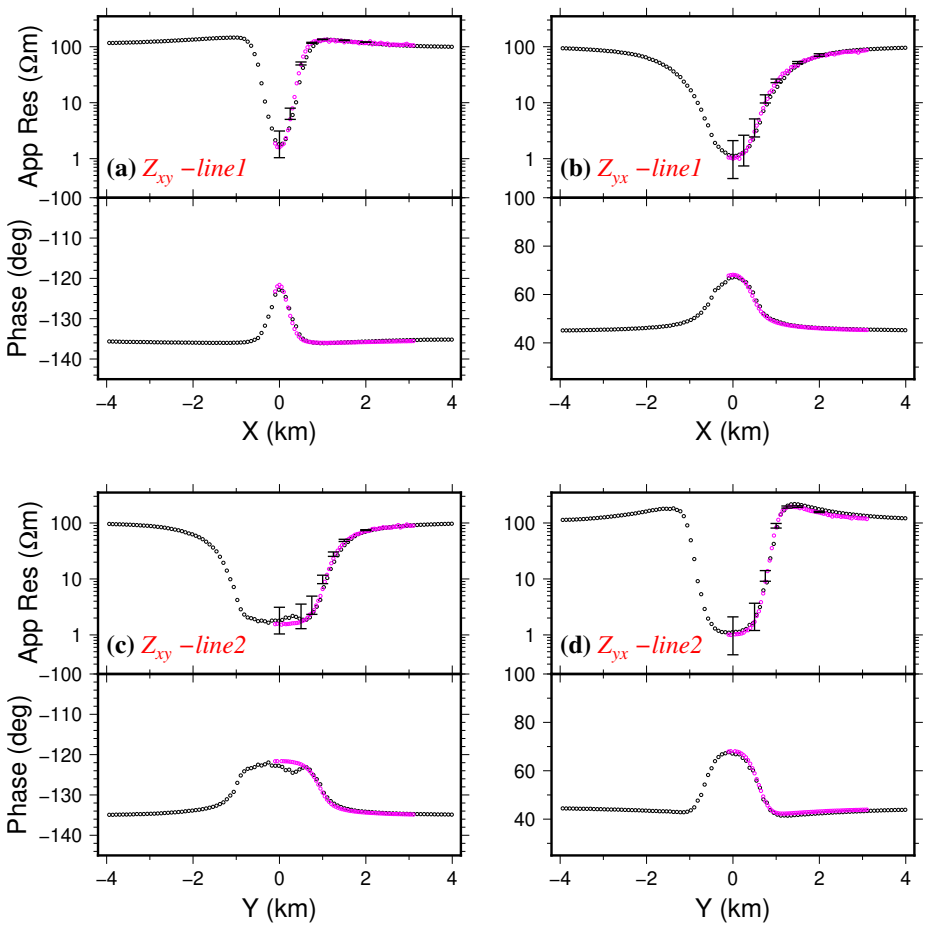

Figure D.1. Computed impedance components Z_{xy} and Z_{yx} at the frequency of 0.1 Hz for line 1 (panel **a**, **b**) and line 2 (panel **c**, **d**) using the hybrid meshfree method for the 1st discretization (total number of points equal to 7,414) in Table 4.2. Also shown are a finite volume solution and other mesh-based solutions (see Fig 4.5).

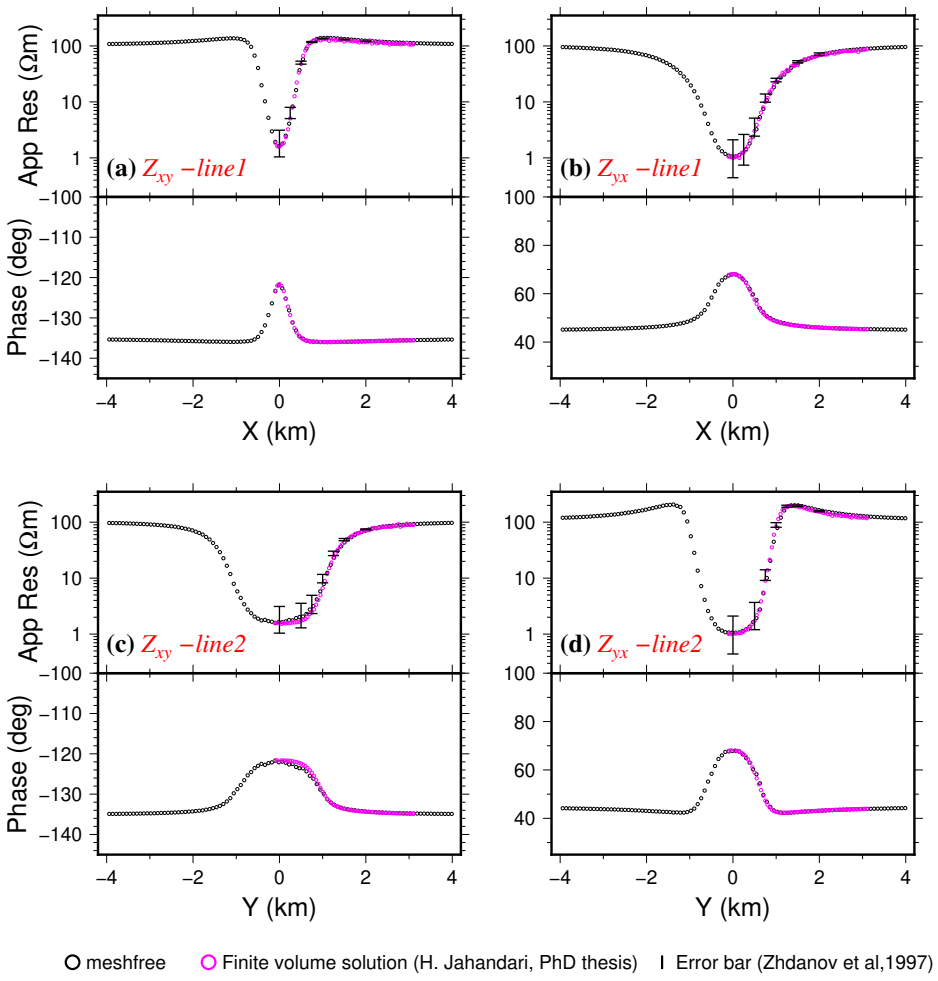

Figure D.2. The same plots as in Fig D.1 but using the 4th discretization (total number of points equal to 58,044) in Table 4.2.

Appendix E

Primary-secondary field approach for CSEM modelling

The $\mathbf{A}$-ψ equations for the total potentials, with $\sigma = \sigma_p + \sigma_s$ ($\sigma_s = \sigma - \sigma_p$ is the conductivity difference between the total conductivity model σ and the primary, or background, conductivity model σ_p), are

$$-\nabla^2\mathbf{A} + i\omega\mu(\sigma_p + \sigma_s)\mathbf{A} + (\sigma_p + \sigma_s)\mu\nabla\psi = \mu\mathbf{J}_s + \nabla \times \mathbf{M}_s, \tag{E.1}$$

$$\nabla \cdot [i\omega\mu(\sigma_p + \sigma_s)\mathbf{A} + (\sigma_p + \sigma_s)\mu\nabla\psi] = \nabla \cdot (\mu\mathbf{J}_s). \tag{E.2}$$

Similarly, the $\mathbf{A}$-ψ equations for the primary potentials ($\mathbf{A}_p$, ψ_p) are

$$-\nabla^2\mathbf{A}_p + i\omega\mu\sigma_p\mathbf{A}_p + \sigma_p\mu\nabla\psi_p = \mu\mathbf{J}_s + \nabla \times \mathbf{M}_s, \tag{E.3}$$

$$\nabla \cdot (i\omega\mu\sigma_p\mathbf{A}_p + \sigma_p\mu\nabla\psi_p) = \nabla \cdot (\mu\mathbf{J}_s), \tag{E.4}$$

since both the primary EM fields over the background conductivity model and the total EM fields over the total conductivity model are induced by the same source. By using the relations $\mathbf{A} = \mathbf{A}_p + \mathbf{A}_s$ and $\psi = \psi_p + \psi_s$ and subtracting eqs (E.3)-(E.4)

from corresponding eqs (E.1)-(E.2), one obtains

$$-\nabla^2 \mathbf{A}_s + i\omega\mu(\sigma_s \mathbf{A}_p + \sigma \mathbf{A}_s) + \mu(\sigma_s \nabla\psi_p + \sigma\nabla\psi_s) = \mathbf{0}, \tag{E.5}$$

$$\nabla \cdot [i\omega\mu(\sigma_s \mathbf{A}_p + \sigma \mathbf{A}_s)] + \nabla \cdot [\mu(\sigma_s \nabla\psi_p + \sigma\nabla\psi_s)] = 0. \tag{E.6}$$

In eqs (E.5) and (E.6), since σ, σ_s, $\mathbf{A}_p$ and ψ_p are known before solving for a numerical solution for the secondary potentials ($\mathbf{A}_s$, ψ_s), they are re-arranged as

$$-\nabla^2 \mathbf{A}_s + i\omega\mu\sigma \mathbf{A}_s + \mu\sigma\nabla\psi_s = -i\omega\mu\sigma_s \mathbf{A}_p - \mu\sigma_s\nabla\psi_p, \tag{E.7}$$

$$\nabla \cdot (i\omega\mu\sigma \mathbf{A}_s) + \nabla \cdot (\mu\sigma\nabla\psi_s) = -\nabla \cdot (i\omega\mu\sigma_s \mathbf{A}_p) - \nabla \cdot (\mu\sigma_s\nabla\psi_p). \tag{E.8}$$

It is seen here that only the secondary potentials need to be numerically solved. Also, it is noted that the primary electric field, $\mathbf{E}_p$, satisfies

$$\mathbf{E}_p = -i\omega \mathbf{A}_p - \nabla\psi_p, \tag{E.9}$$

eqs (E.7) and (E.8) can be further re-arranged in terms of $\mathbf{E}_p$ as

$$-\nabla^2 \mathbf{A}_s + i\omega\mu\sigma \mathbf{A}_s + \mu\sigma\nabla\psi_s = \mu\sigma_s \mathbf{E}_p, \tag{E.10}$$

$$\nabla \cdot (i\omega\mu\sigma \mathbf{A}_s) + \nabla \cdot (\mu\sigma\nabla\psi_s) = \nabla \cdot (\mu\sigma_s \mathbf{E}_p). \tag{E.11}$$

By using eqs (E.10) and (E.11), computation of the Coulomb-gauged primary vector potential is avoided and calculation of the primary fields is thus simplified. Once the secondary electric field ($\mathbf{E}_s$) and magnetic field ($\mathbf{H}_s$) are numerically computed from

$\mathbf{A}_s$ and ψ_s, the total electric field and magnetic field are obtained as

$$\mathbf{E} = \mathbf{E}_p + \mathbf{E}_s, \tag{E.12}$$

$$\mathbf{H} = \mathbf{H}_p + \mathbf{H}_s. \tag{E.13}$$

The system of eqs (E.10) and (E.11) can be solved in a number of numerical ways. Here, scalar FE using unstructured tetrahedral meshes and scalar hybrid meshfree (RBF-FD) methods are employed.

FE discretization

For the FE method, the standard Galerkin method and linear basis functions are used. The mesh comprises tetrahedral elements. The discretization of the left-hand side of eqs (E.10) and (E.11) is the same as that in total-field FE method. The integration of the right-hand side in eq (E.10) with a test function, v, is

$$\int_{\Omega_{test}} v(\mu\sigma_s E_{p,k})\, dV = \mu \sum_{j=1}^{n} \int_{e_j} v_j \sigma_{s,j} \tilde{E}_j\, dV, \quad k = x, y, z. \tag{E.14}$$

In eq (E.14), n is the number of elements whose union is the support of the test function v, v_j is the part of v over the element e_j, and similarly, $\sigma_{s,j}$ and $\tilde{E}_j$ are the residual conductivity and primary electric field component ($E_{p,k}, k = x, y, z$), respectively, over the element e_j. In each element, $\sigma_{s,j}$ is a constant, but $\tilde{E}_j$ is a continuous scalar function. Here, $\tilde{E}_j$ is approximated within each element as a linear function by taking advantage of the point-based field values at the four vertices of

the element. Eq (E.14) then becomes

$$\int_{\Omega_{test}} v(\mu\sigma_s E_{p,k})\, dV = \mu \sum_{j=1}^{n} \sigma_{s,j} \int_{e_j} v_j \sum_{m=1}^{4} N_{j,m}\tilde{E}_{j,m}\, dV, \tag{E.15}$$

where $N_{j,m} = N_{j,m}(x, y, z)$ are the FE shape functions over the jth element, $\tilde{E}_{j,m}$ are the nodal electric field component values on the vertices. Depending on the nodal connectivity, v_j is one of $N_{j,m}$ in each FE element. Denoting

$$\int_{e_j} v_j \sum_{m=1}^{4} N_{j,m}\tilde{E}_{j,m}\, dV = \sum_{m=1}^{4} \tilde{E}_{j,m} \int_{e_j} v_j N_{j,m}\, dV = M_j, \tag{E.16}$$

eq (E.15) is re-written as

$$\int_{\Omega_{test}} v(\mu\sigma_s E_{p,k})\, dV = \mu \sum_{j=1}^{n} \sigma_{s,j} M_j. \tag{E.17}$$

Similarly, the integration of the right-hand side in eq (E.11) with a scalar test function is

$$\begin{aligned}\int_{\Omega_{test}} v\nabla\cdot(\mu\sigma_s\mathbf{E}_p)\, dV &= \int_{\Omega_{test}} \nabla\cdot(v\mu\sigma_s\mathbf{E}_p)\, dV - \int_{\Omega_{test}} \mu\sigma_s\mathbf{E}_p\cdot\nabla v\, dV \\ &= \int_{\partial\Omega_{test}} v\mu\sigma_s\mathbf{E}_p\cdot\mathbf{n}_s\, dS - \int_{\Omega_{test}} \mu\sigma_s\mathbf{E}_p\cdot\nabla v\, dV\end{aligned} \tag{E.18}$$

In the first term of the right-hand side in eq (E.18), $\mathbf{n}_s$ is the outward normal unit vector for the closed surface $\partial\Omega_{test}$. In the linear scalar FE method with tetrahedral elements, each test function (associated with nodes) is exactly zero by construction

at the boundary of Ω_{test}, therefore the first term vanishes and eq (E.18) becomes

$$\begin{aligned}\int_{\Omega_{test}} v\nabla\cdot(\mu\sigma_s\mathbf{E}_p)\,dV &= -\int_{\Omega_{test}} \mu\sigma_s\mathbf{E}_p\cdot\nabla v\,dV \\ &= -\int_{\Omega_{test}} \mu\sigma_s(\frac{\partial v}{\partial x}E_{p,x}+\frac{\partial v}{\partial y}E_{p,y}+\frac{\partial v}{\partial z}E_{p,z})\,dV. \end{aligned} \tag{E.19}$$

The calculation of the above integration is then similar to the process described for eq (E.10):

1. The integration over Ω_{test} is first broken into parts of integrations over connected elements for a particular test function v_j;

2. Over each element, each component of primary electric field $E_{p,k}$ $(k = x, y, z)$ is represented using FE shape functions, and v_j is one of the 4 shape functions;

3. Carry out the elemental integrations analytically. The conductivity σ_s is considered as a constant over each element.

Hybrid meshfree discretization

For the hybrid RBF-FD method, the combination of strong-form and weak-form discretizations of eqs (E.10) and (E.11) follows the MT treatment, in which Galerkin FE discretization of equations is only used for interfacial points. In deriving algebraic equations in the case of RBF-FD, primary **E** fields at the degrees of freedom (i.e. the interior points) are directly used for the right-hand sides of eqs (E.10) and (E.11).

Appendix F

Integration of source term functions in unstructured meshes

In scalar FE methods, an unknown function is typically approximated within an element (the cell unit in a mesh) by a complete set of polynomials of some degree:

$$f(x, y, z) \approx \hat{f} = \sum_{j=1}^{n} \phi_j(x, y, z) c_j, \tag{F.1}$$

where the polynomials ϕ_j are called basis functions, c_j are interpolation coefficients to be determined. An example set of complete linear polynomials (i.e., degree p =1) is $[1, x, y, z]$ in the 3-D case. Once a specific type of element is chosen (e.g., triangles in 2D), the coefficients in eq (F.1) can be determined by using Lagrange interpolation conditions, and eq (F.1) can then be re-arranged as (Jin, 2014)

$$f(x, y, z) \approx \hat{f} = \sum_{j=1}^{n} \phi_j(x, y, z) c_j = \sum_{j=1}^{n} N_j(x, y, z) f_j, \tag{F.2}$$

where N_j are called shape functions, f_j are function values at the vertices of the element.

In the case of using triangular or tetrahedral elements, the volume integrations involving the source terms can be carried out analytically. To simplify the calculation,

a wire source (e.g., grounded wires or magnetic loop wires) carrying the electric current density $\mathbf{J}_s$ is set to be aligned with the edges of the mesh, as shown in Fig F.1. In Galerkin FE methods, the test functions, which are associated with the nodes in the mesh, and the shape functions are constructed from the same function space. Moreover, the test function for a node j, v_j, is the combination of all shape functions N_j at the node over the elements that share the node; thus, the support of the test function is the union of the shared elements of the node j, see Fig F.2. This suggests that the volume integrations involving the source current density are zero for those nodes that are not residing on the source segments:

$$\int_{\Omega_{test}} v(\mu \mathbf{J}_s)\, dV = 0; \quad \int_{\Omega_{test}} v\nabla \cdot (\mu \mathbf{J}_s)\, dV = 0. \tag{F.3}$$

The support of the test function is denoted as Ω_{test} in the above. For those nodes that are residing on the source segments (e.g., node A in Fig F.2), the source term integrations are non-zero. For the integration of current density with a source segment from $\mathbf{r}_1$ to $\mathbf{r}_2$ (assuming the current flows from $\mathbf{r}_1$ to $\mathbf{r}_2$), it becomes

$$\begin{aligned}
\int_{\Omega_{test}} v(\mu \mathbf{J}_s)\, dV &= \mu \int_{\Omega_{test}} v\mathbf{J}_s\, dV \\
&= \mu \int_{\Omega_{test}} vI_0 \left[\mathcal{H}(\mathbf{r}_1) - \mathcal{H}(\mathbf{r}_2)\right] \delta(\mathbf{r}, \mathbf{r}_1, \mathbf{r}_2)\hat{\mathbf{u}}_s\, dV \\
&= \mu \int_{\Omega_{test}} v' I_0 \left[\mathcal{H}(x_1') - \mathcal{H}(x_2')\right] \delta(y' - y_0')\delta(z' - z_0')\hat{\mathbf{u}}_s'\, dV',
\end{aligned} \tag{F.4}$$

where $\delta(\mathbf{r}, \mathbf{r}_1, \mathbf{r}_2)$ denotes the 2-D Dirac delta function in the plane that is perpendicular to the orientation of the source segment $\hat{\mathbf{u}}_s = \mathbf{r}_2 - \mathbf{r}_1$. The last identity in eq (F.4) is derived by rotating the coordinate system (indicated without the prime

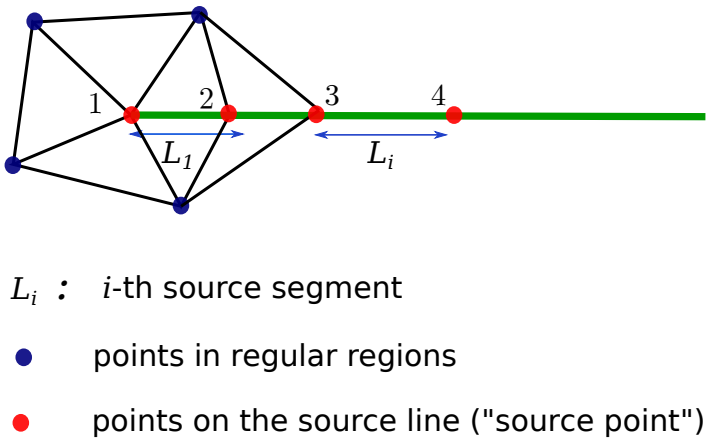

Figure F.1. An illustrative diagram of the CSEM source segments (shown as bold green line) aligned along the edges of unstructured triangular (tetrahedral for 3D) meshes.

symbol) such that in the new coordinate system (x', y', z') the x' axis is aligned with the source segment orientation. $\hat{\mathbf{u}}_s$ and $\hat{\mathbf{u}}_s^{'}$ are the unit vectors along the source segment in the original and the new coordinate systems, respectively. Since v' changes exactly the same way as v does in Ω_{test} and $\mathcal{H}(x_1') - \mathcal{H}(x_2')$ is only nonzero along the segment, eq (F.4) is reduced to a 1-D line integral:

$$\int_{\Omega_{test}} v(\mu \mathbf{J}_s)\, dV = \mu I_0 \int_{x_1'}^{x_2'} v' \left[\mathcal{H}(x_1') - \mathcal{H}(x_2')\right] \hat{\mathbf{u}}_s^{'}\, dx', \tag{F.5}$$

with $v' = v'(x')$ reduced to be the 1-D test function. The integration result of the above can be readily obtained when using polynomial-based test functions. For example, if the linear basis functions are used, then the 1-D test function becomes

$$v'(x') = \frac{x_2' - x'}{x_2' - x_1'}, \tag{F.6}$$

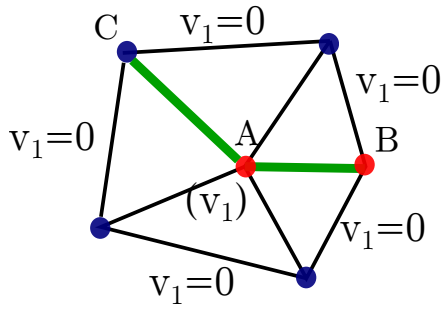

Figure F.2. An illustrative diagram of the support of the test function (v_1) for a node in Galerkin FE methods. v_1 is only nonzero within the five triangles connected to node A, or equivalently, the support of v_1 is the union of the five triangles shown above. $v_1 = 1$ at the node A and is zero at all opposite edges of the elements for the node A. Within each element, v_1 linearly changes (assuming linear basis functions are used) from one at the node A to zero at the opposite edge. Therefore, v_1 also changes the same way from node A to node B (or C) at the source segment (shown as bold green).

which satisfies $v'(x_1') = 1$ and $v'(x_2') = 0$. As a result, eq (F.5) is integrated as

$$\int_{\Omega_{test}} v(\mu \mathbf{J}_s)\, dV = \mu I_0 \frac{x_2' - x_1'}{2} \hat{\mathbf{u}}_s' = \mu I_0 \frac{L_{12}}{2} \hat{\mathbf{u}}_s' = \mu I_0 \frac{L_{12}}{2} \hat{\mathbf{u}}_s, \tag{F.7}$$

where L_{12} is the segment length of the wire source.

The result in eq (F.7) is valid for any arbitrarily oriented source segments for those nodes residing on the source wire, as shown in Fig F.2. For the integration of the divergence of $\mathbf{J}_s$, it is calculated as

$$\int_{\Omega_{test}} v \nabla \cdot (\mu \mathbf{J}_s)\, dV = \mu I_0 \int_{\Omega_{test}} v(\mathbf{r})[\delta(\mathbf{r} - \mathbf{r}_m) - \delta(\mathbf{r} - \mathbf{r}_n)]\, dV = \pm \mu I_0, \tag{F.8}$$

at the two ends ($\mathbf{r}_m$, $\mathbf{r}_n$) of the electric wire source. The positive value is valid if the node is the segment end to which the electric current streams converge ($\mathbf{r}_m$), and the negative value is valid at the end from which the current streams diverge ($\mathbf{r}_n$). The

above divergence integration is zero everywhere else.